Applied Hydrogeophysics For Managed Aquifer Recharge

Dissertation

zur

Erlangung des Doktorgrades (Dr. rer. nat.)

der

Mathematisch-Naturwissenschaftlichen Fakultät

der

Rheinischen Friedrich-Wilhelms-Universität Bonn

vorgelegt von

Klaus Haaken

aus

Kleve

Bonn 2017

Angefertigt mit Genehmigung der Mathematisch-Naturwissenschaftlichen Fakultät
der Rheinischen Friedrich-Wilhelms-Universität Bonn
am Steinmann-Institut für Geologie, Mineralogie und Paläontologie

1. Referent: Prof. Dr. Andreas Kemna, Universität Bonn, Deutschland
2. Referent: Prof. Dr. Alex Furman, Technion Haifa, Israel

Tag der Promotion: 8. Dezember 2017
Erscheinungsjahr: 2018

Diese Dissertation ist auf dem Hochschulschriftenserver der ULB Bonn
http://hss.ulb.uni-bonn.de/diss_online elektronisch publiziert.

Abstract

This thesis investigates the application of hydrogeophysical monitoring and characterization techniques in the context of managed aquifer recharge (MAR). MAR is a sustainable technology in modern water resources management. It denotes the storage, purification, and reclamation of water in aquifers under controlled conditions. MAR receives increasing attention due to generally increasing water demand, especially in (semi-)arid areas. Successful implementation and operation of MAR requires a detailed knowledge of the system in terms of geology and hydrogeology. Therefor, spatially extensive, high-resolution non-invasive geophysical techniques in combination with classical hydro-geological approaches can provide key information. In this thesis, both field monitoring and numerical modeling of different concepts of MAR using hydrogeophysics are presented. A focus lies on the geoelectrical imaging method which can monitor the movement of water in the subsurface with high spatial and temporal resolution due to the direct relation of electrical conductivity to water salinity and/or water saturation. The geoelectrical method is applied to i) simple surface infiltration schemes in order to quantify the volume of infiltrated water, ii) soil aquifer treatment to monitor cyclic ponded infiltration under high fluxes, and iii) aquifer storage and recovery, aiming at understanding complex saline-freshwater systems. The thesis shows that by means of petrophysical models, a quantification of water volume can be achieved using time-lapse electrical imaging. Furthermore, a new approach of temporal-based aquifer zonation is presented by using time-lapse electrical imaging under very high water fluxes. It shows that the heterogeneous subsurface can be imaged for hydraulic characteristics which is not possible with classical approaches or with a single electrical measurement alone. In another study, the complex saline-freshwater interactions of freshwater injection in a hyper-saline aquifer is investigated in a field monitoring and numerical modeling study. The simulation results were used to be compared against the real field results. The exercise demonstrates that the evolution of the freshwater is strongly influenced by the system's hydraulic heterogeneities. This thesis highlights how the joint use of geophysics with hydro-geological approaches as well as numerical modeling give fundamental information for MAR applications. Eventually, the presented approaches of hydrogeophysics can be used to enhance the implementation and operation of MAR applications.

Zusammenfassung

Diese Arbeit handelt von der Anwendung hydrogeophysikalischer Untersuchungsmethoden im Bereich der künstlichen Grundwasseranreicherung (MAR; engl.: Managed Aquifer Recharge). MAR ist die Speicherung, Reinigung und Weiterverwertung von Wasser im Untergrund unter kontrollierten Bedingungen und stellt eine nachhaltige Methode des modernen Wasserressourcenmanagements dar. Das Interesse an MAR nimmt aufgrund der steigenden Nachfrage nach Wasser mehr und mehr zu, besonders im (semi-)ariden Raum. Eine erfolgreiche Implementierung und Anwendung von MAR erfordert detaillierte Kenntnisse der hydro-geologischen Untergrundcharakteristiken. Räumlich extensive, nicht-invasive und hoch-auflösende geophysikalische Methoden ermöglichen diesen Kenntnisgewinn in Kombination mit klassischen hydrogeologischen Untersuchungsmethoden. Diese Arbeit präsentiert die Anwendung hydrogeophysikalischer Methoden anhand von Feld- und Modellierungsstudien von unterschiedlichen Konzepten des MAR. Der Fokus liegt auf der geoelektrischen Bildgebung, die die Bewegung von Wasser im Untergrund mit hoher räumlicher und zeitlicher Auflösung aufgrund der Relation zwischen der elektrischen Leitfähigkeit und der Sättigung bzw. des Salzgehaltes des Wassers wiedergeben kann. Die Geoelektrik ist in dieser Arbeit angewendet in i) einfachen Oberflächeninfiltrationen mit dem Ziel der Quantifizierung der infiltrierten Wassermenge, ii) dem Monitoring des sogenannten Soil Aquifer Treatment unter hohen Infiltrationsflüssen und iii) dem Aquifer Storage and Recovery, um die komplexen Interaktionen zwischen Salz- und Frischwasser zu untersuchen. Anhand von petrophysikalischen Modellen wird gezeigt, dass über die Geoelektrik eine Quantifizierung von Wassermengen möglich ist. Darüber hinaus wird ein neuer Ansatz der Aquifer Zonierung präsentiert, der auf der zeitlichen, geoelektrischen Beobachtung basiert. Dieser Ansatz zeigt, dass eine hydraulische Charakterisierung des heterogenen Untergrundes möglich ist, was mit klassischen (punktförmigen) Ansätzen oder einzelnen geoelektrischen Messungen allein nicht möglich ist. In einer weiteren Studie werden die komplexen Interaktionen bei der Injektion von Frischwasser in einen hyper-salinen Aquifer in einem Feldexperiment und einer darauf aufbauenden numerischen Modellstudie untersucht. Die Simulationsergebnisse werden dabei mit den Feldergebnissen verglichen. Das Experiment zeigt, dass die Ausbreitung des Frischwassers primär von den hydraulischen Heterogenitäten des Untergrundes beeinflusst wird. Diese Arbeit zeigt, wie die integrierte Anwendung von geophysikalischen Verfahren und klassischen hydrogeologischen Ansätzen sowie numerischen Modellen fundamentale Informationen für MAR Anwendungen liefern. Schlussendlich zeigt sich, dass die präsentierten hydrogeophysikalischen Methoden zu einer Verbesserung in der Implementierung und dem Betrieb von künstlichen Grundwasseranreicherungsanlagen führen.

Acknowledgements

At this point I would like to thank quite a number of people. Foremost my Doktorvater Andreas Kemna, who first of all made this work possible. I thank him for all the helpful discussions, motivating words, and all the possibilities that arose through new contacts.

This thesis includes studies from different research projects which were funded from different institutions; namely the German Federal Ministry of Education and Research (BMBF) which funded the projects under license numbers 02WM1081 and 02WA1262/WT1203, and the Regione Autonoma della Sardegna (Italia) for granting the Basic Research Project L.R. 7/2007 (CRP2_686, Gian Piero Deidda).

Many thanks to Alex Furman and Noam Weisbrod for the great teamwork in Israel and the excellent support during field work. And also to the Israeli water company Mekorot, who made the working area available for us. *Toda!*

A very special thanks goes to our Italian colleagues Giorgio Cassiani, Gian Piero Deidda, Claudio Paniconi, Mario Putti, Rita Deiana, and Carlotta Scudeler for the opportunity to our experiment and the great collaboration in Cagliari and Padova. *Mille Grazie!*

I would like to thank Martin Sauter and his working group at the University of Göttingen, here especially Sebastian and Fabian for the help and nice days in the field and on conferences. A special thanks also to Amer Marei for the very great support in the working area in the West Bank, to the habitants of the village Auja and the Palestinian Water Authority PWA. *Schokran!*

I would like thank my former colleague Adrián for the numerous, cool days in the field and the office, I learned a lot during that time. To my former colleagues at the Steinmann-Institute, especially Andreas, Anna, Bernd, Christoph, Jannik, Johannes, Lisa, Maxi, Sebastian, Simon and Shiva. And Stephan for reading parts of this thesis. *Danke!*

I thank my mother, my brother Thomas and my whole family. And last but not least, I thank Isabelle for the support and patience in all needs, that she is always on my side and especially for the understanding concerning my not rare absences.

Klaus Haaken

Contents

Chapter 1

Introduction

1.1 Motivation & Objectives

In times of climate change, population growth and thereby accompanying water demand, the interest on economical and sustainable exploitation of water resources as well as innovative technologies in water reuse receives increasing attention. Particularly in regions with low precipitation, where water demand can easily cause a water crisis, integrated water resources management is absolutely necessary.

In 2010, the United Nations General Assembly declared the access to clean water for drinking and sanitation a Human Right (UN, 2010). Unfortunately, this access is not a matter of course. Areas with water scarcity have to handle their resources carefully to meet this human right. This is not possible anymore with conventional approaches.

One sustainable technology in the use and reuse of almost any water resource is the artificial recharge of groundwater, or better known as Managed Aquifer Recharge (MAR) (e.g., Asano, 1985; Bouwer, 2002; Dillon, 2005; Gale, 2005). It is able to provide natural, easy and cheap water supply; especially in semi-arid and arid regions where water scarcity is a major concern. MAR is applied successfully since some decades in many different areas of the world; actually, simple schemes of MAR have been applied already for centuries. And to date, many examples for MAR can be found in the literature (e.g., Idelovitch et al., 2003; Tuinhof and Heederik, 2003; Flint and Ellet, 2004; Dillon et al., 2006; Wolf et al., 2007; Nadav et al., 2012; Zuurbier et al., 2014).

MAR simply means the storing of water in aquifers. However, the planning, implementation and operation of an MAR system is generally not ”simple”. For efficient and successful MAR, a detailed knowledge of the subsurface system as well as all involved water resources (i.e., water quality, water quantity, geology, hydrogeology, ecology, etc.) is essential. Especially when it comes to the parameterization of the nontransparent subsurface, one has to face many challenges. Although indispensable, classical investigation techniques for the (hydro)geological characterization of the subsurface, such as investigation boreholes, hydraulic head measurements, or water samples, are mostly point measurements. And this point information can only

provide limited insight into the system characteristics since the volume between the points cannot be obtained and is usually interpolated.

Here, geophysical investigation techniques are very promising since they are able to extensively image the subsurface with high spatial resolution and they are non- or at least minimally invasive. Thus, they do not disturb the subsurface. Primarily established for ore and oil exploration, geophysical methods are increasingly being used in the hydrogeology and environmental field of investigation within the last decades (thus, called hydrogeophysics). Overviews and case studies can be found, e.g. in Rubin and Hubbard (2005), Vereecken et al. (2006) and Binley et al. (2015). One of the most common methods in this field is the Electrical Resistivity Tomography (ERT) due to the direct relation of the electrical conductivity to water content, fluid salinity and/or clay content (e.g., Archie, 1942; Binley and Kemna, 2005; Revil et al., 2012). Applied as monitoring tool, the so-called time-lapse ERT can be used to image the movement of water in the vadose zone (e.g., Daily et al., 1992; Zhou et al., 2001; Deiana et al., 2007), the spatio-temporal evolution of salt plumes (e.g., Slater et al., 2000; Kemna et al., 2002; Singha and Gorelick, 2005) or general variations of salt concentration (e.g., Hayley et al., 2009; Moreno et al., 2015). Those results provide information about flow model parameters (e.g., Binley et al., 2002a) and/or solute transport parameters (e.g., Kemna et al., 2002; Vanderborght et al., 2005; Koestel et al., 2008; Müller et al., 2010).

Also very common in the field of hydrogeology is the method of Ground-Penetrating Radar (GPR) (e.g., Finsterle and Kowalsky, 2008). GPR is able to provide high resolution images of dielectric properties of the soil which can be related to soil moisture content and the lithological distribution (e.g., Binley et al., 2002a; Annan, 2005, and references therein).

Furthermore, a combination of different geophysical methods couples the advantages of two methods and can reveal new information. Often used is the combination of ERT with GPR (e.g., Binley et al., 2002a,b; Slater and Reeve, 2002; Linde et al., 2006; Doetsch et al., 2010a, 2012a). And also the combination of ERT and seismic methods was applied successfully (e.g., Faust, 1953; Mazác et al., 1988; Meju et al., 2003).

To date, only few studies exist using geophysical tools for MAR applications. Davis et al. (2008) used time-lapse gravity monitoring in their study at an abandoned underground coal mine that was developed for artificial aquifer storage and recovery as a subsurface reservoir. The time-lapse micro-gravity surveys were able to detect the spatial distribution of the injected water and to produce density-contrast models. With the changes in density and some knowledge in porosity, the gravity data can be related to hydraulic parameters.

In the study of Maliva et al. (2009), advanced borehole geophysical logging tools were applied to improve aquifer characterization and modeling for MAR investigations. They used neutron-gamma ray spectroscopy, micro-resistivity imaging, and nuclear magnetic resonance to estimate porosity, hydraulic conductivity, salinity, and the mineralogy. They also stated that the geophysical logging tools are not a stand-alone technique, but can give supplementary, fine-scaled data. However, borehole logging tools are limited to the vicinity around the borehole and strongly rely on the borehole conditions. Irregular boreholes may bias the logging data and lead to

uncertain interpretations. Still, borehole geophysical logging tools are much more cost and time efficient than core sampling.

Minsley et al. (2011) gave recommendations on the use of hydrogeophysical tools for aquifer storage and recovery systems. They conducted a numerical study with flow and transport simulations and simulations of the geophysical response with the aim to quantify site-specific parameters for an aquifer storage and recovery site in Kuwait. The applied geophysical methods were electrical resistivity, time-domain electromagnetics, and seismics. They investigated the sensitivity of these different methods to changes in the subsurface properties. Since the different methods are sensitive to different properties, their study aims at giving recommendations which method is best to be applied, which, however, also depends on the questions of investigation. They saw that, at least in their particular study, the seismic and electromagnetic methods were limited due to low sensitivities.

Mawer et al. (2013) conducted a synthetic study for the use of vertical electrical conductivity profiles beneath an MAR pond to estimate saturated hydraulic conductivity and van Genuchten parameters as well as infiltration rates. Using a homogeneous unsaturated zone, they studied the sensitivity of vertical electrical resistivity profiles in direct-push resistivity probes to its temporal and spatial resolution. They also derived a relation to estimate infiltration rates and pond bottom clogging from the electrical conductivity data. The same group studied water infiltration beneath an MAR pond using long 1D electrical resistivity probes (Nenna et al., 2014). The resistivity measurements were able to capture the water table response and to identify variations in water saturation.

The study of Parsekian et al. (2014) applied geoelectrical imaging of the subsurface below an aquifer recharge and recovery site alongside with hydrochemical measurements to identify preferential flow paths. With the aim to investigate water quality and aquifer heterogeneity, their study showed that the coupled interpretation of hydrochemical and geophysical data can reduce the uncertainty concerning water quality changes. The data can be used to delineate areas for new wells and helps to understand infiltration patterns.

In the recent study of Mawer et al. (2016), the heterogeneous infiltration rate in an MAR pond was investigated using temperature sensing. Additional ERT measurements were used to improve the design and operation of MAR systems by providing critical information about parameters controlling the infiltration rates.

All these studies already show that hydrogeophysics is a useful tool for the investigation of questions concerning MAR systems. However, more studies are required for these complex applications, both in terms of hydrogeophysics as well as MAR systems.

This study deals with different aspects of MAR, such as the assessment of selected sites for suitability of MAR, the water infiltration in the context of soil aquifer treatment and the complex interactions between saltwater and freshwater as they appear in aquifer storage and recovery systems. These applications are investigated using hydrogeophysical monitoring in combination with conventional hydrogeological approaches as well as numerical modeling.

The aim of this thesis is on one hand to further show that hydrogeophysics in

general, and geoelectrical imaging in particular, is a powerful tool to be applied for the requirements of the planning, implementation and performance of MAR sites. It will not, of course, be shown that hydrogeophysics is a stand-alone tool in the field of investigation, but in addition to classical (hydro)geological techniques it is able to provide enhanced information, especially about the (often heterogeneous) subsurface lithological and hydraulic characteristics; since those cannot be obtained by the point-information-type data of most classical techniques alone. The thesis shows that time-lapse ERT is able (a) to image the vadose zone under very high water fluxes and (b) to characterize flow and transport dynamics in saltwater-freshwater systems with both, high spatial and high temporal resolution. Using the results of these studies, they can be used, e.g., for enhancements of existing MAR sites.

On the other hand, for instance a new developed approach will be presented in this thesis which uses the results of temporal dense time-lapse ERT data for a temporal-based zonation of the subsurface. The results show aquifer heterogeneities related to hydraulic characteristics which cannot be imaged with a single ERT measurement or with conventional hydrogeological techniques alone. This approach is also useful and applicable in other fields of hydrology, not only in MAR. Also in this thesis, recommendations will be given on the use of the geoelectrical imaging methods for questions/problems concerning different application types of managed aquifer recharge.

1.2 Structure of this Thesis

This thesis uses geophysical investigation techniques (with a focus on geoelectrical imaging) to characterize and monitor various applications of MAR in four different case studies.

The first study (Chapter 3) is a numerical feasibility study of ponded water infiltration, monitored using time-lapse ERT in order to image the infiltrating water front and to quantify the infiltrated water volume.

The second study (Chapter 4) assesses an alluvial basin in the Lower Jordan River Valley (West Bank) for the suitability of storing run off water in the subsurface. Here, refraction seismics and geoelectrical imaging are used to capture the geological geometry of the basin and water infiltration experiments, monitored with the geoelectrical method, are used to define hydraulic parameters of the sediments. Investigation boreholes, infiltration tests and soil samples emphasize the results of the geophysics.

In the third study (Chapter 5), the physical process of water infiltration under high water fluxes (ponded infiltration) in the context of soil aquifer treatment at the Shafdan site in Israel is investigated using time-lapse geoelectrical imaging. The dynamic imaging data are used to give a new approach of temporal-based subsurface zonation, related to hydraulic characteristics.

The fourth study (Chapter 6) deals with the process of mixing related to freshwater injection in a hyper-saline aquifer in Sardegna, Italy. The experiment was monitored using time-lapse geoelectrical imaging in boreholes. An extensive numerical study

of the experiment with simulation of density-dependent flow and transport as well as electrical measurements was undertaken to investigate the observed phenomena.

Beforehand of the presentation of the studies, a general theoretical background of MAR and the applied geophysical investigation techniques will be given. Finally, a summary of conclusions and some perspectives close the thesis.

Chapter 2

Theoretical Background

2.1 Management of Aquifer Recharge

The Management of Aquifer Recharge (MAR) describes the storage and treatment of water resources in aquifers (e.g., Asano, 1985; Pyne, 1995; Bouwer, 2002; Dillon, 2005; Gale, 2005). Here, a water source (e.g., storm water, surface/runoff water, groundwater, or treated wastewater) is infiltrated or injected under controlled conditions into an aquifer (confined or unconfined; porous or fractured/karstic) for storage and/or purification of water (Figures 2.1 and 2.2). The reclaimed water can be used for domestic or agricultural purposes. MAR can also occur as unintentional recharge, for example through irrigation. However, here MAR is referred to intentional recharge.

Figure 2.1: Picture of an infiltration pond from the Shafdan site in Israel (see Chapter 5) as an example for the MAR technique soil aquifer treatment (SAT) (Section 2.1.1). Note that the water table here above the surface does not exceed 0.5 m.

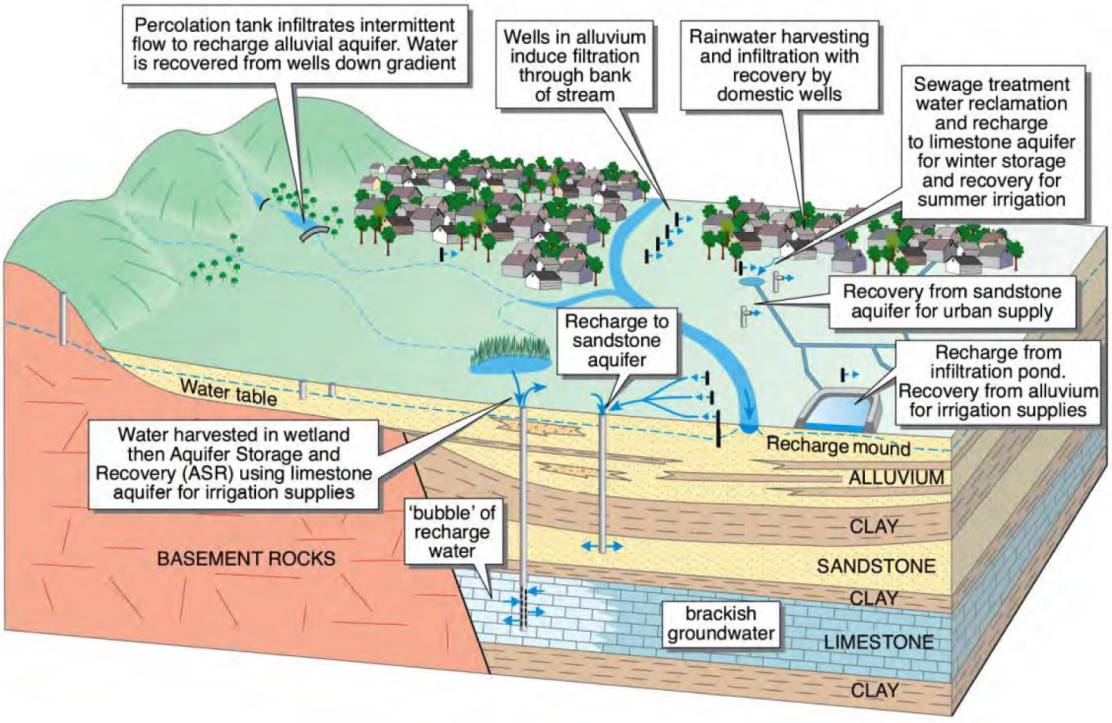

Figure 2.2: Schematic overview of MAR after Dillon et al. (2009), adapted from Gale (2005).

MAR has great advantages, for instance compared to conventional surface storage (like ponds or surface dams) since it can prevent water from losses through evaporation or from contamination, e.g. through algae growth. Benefits from MAR can be, beside others, economic and health risk reduction, increased agricultural yields and reduced vulnerability to droughts (Gale, 2005). Furthermore, it provides a cheap and easy form of water supply and has the potential to be a major contributor to the UN Millennium Goal for Water Supply (Dillon, 2005).

Especially for semi-arid and arid regions, where high evaporation rates and high spatial and temporal variability in rainfall occur, MAR can be a very effective tool. High water demand is usually given in these regions and growing population, agriculture, and tourism lead to further growing water demand. Additionally, most (semi-)arid regions perceive rising average temperatures and lowering annual rainfall due to climate change which leads to decreasing water resources available for water supply.

Applications of MAR can be found in, e.g., Gale (2005) with examples from Australia, Balochistan, Hungary, India, Iran, Kenya, Mexico, Namibia, South Africa, and Spain. Another example demonstrating the options of MAR for Australia comprises Dillon et al. (2009). Also, Tuinhof and Heederik (2003) comprise a collection of MAR case studies around the world. EWRI/ASCE (2001) is a technical guideline for the planning, construction, maintenance, and operation of MAR projects of many different types, also assessing economical, environmental, and legal considerations.

2.1.1 Recharge Techniques

MAR is only a general term and can be divided into several types of recharge techniques. These techniques can range in complexity from simple rainwater harvesting to deep-well injection of reclaimed water into a saline aquifer (Gale, 2005). Overall, there are three main groups of techniques that differ by their primary water application scheme (Maliva and Missimer, 2012):

- Subsurface injection through wells,
- Surface or near-surface application or spreading of water,
- Enhancements of natural recharge processes.

These application schemes can be further differentiated into various recharge techniques. The most common techniques are described as follows (Figure 2.3) (after Dillon, 2005; Gale, 2005):

- **Aquifer storage and recovery (ASR):** Involves the injection of water into an aquifer through wells for storage and later recovery (Pyne, 1995). It can also mean for instance injection of freshwater into a brackish aquifer to increase the availability of mid-quality water, e.g., for agricultural irrigation. ASR is part of the fourth study of this thesis (Chapter 6).
- **Aquifer storage transfer and recovery (ASTR):** Extension of ASR, but the recovery occurs through another well to increase the travel time.
- **Bank filtration:** Infiltration from a surface water body (lake or river) is induced by pumping groundwater from a well or a series of wells beneath it. To guarantee a successful scheme, the surface water quality needs to be acceptable and the permeabilities of the river or lake bed deposits and the aquifer need to be high enough. The travel time of the surface water to the wells should be at least 30 days. Suspended fine material in the surface water body may clog the river or lake bed. Bank filtration is a common technique for drinking water supply in temperate zones.
- **Dune filtration:** Ponded water infiltration within the valleys of dunes and extraction through wells or ponds at lower elevation to balance supply and demand. The method is successfully being used along the coast of the Netherlands. It plays an important role for water abstraction and prevention of seawater intrusion.
- **Infiltration ponds:** Spreading basins for off-stream infiltration through the unsaturated zone to unconfined aquifer. A basin for infiltration is excavated in the ground or placed in a natural system with surrounding banks. The pond is used for controlled infiltration of water into the subsurface system, filling up the aquifer for safe storage. With that, the water is secured from loss like evaporation and from contamination, for instance through algae growth. Infiltration ponds in association with storm water usually have big concerns

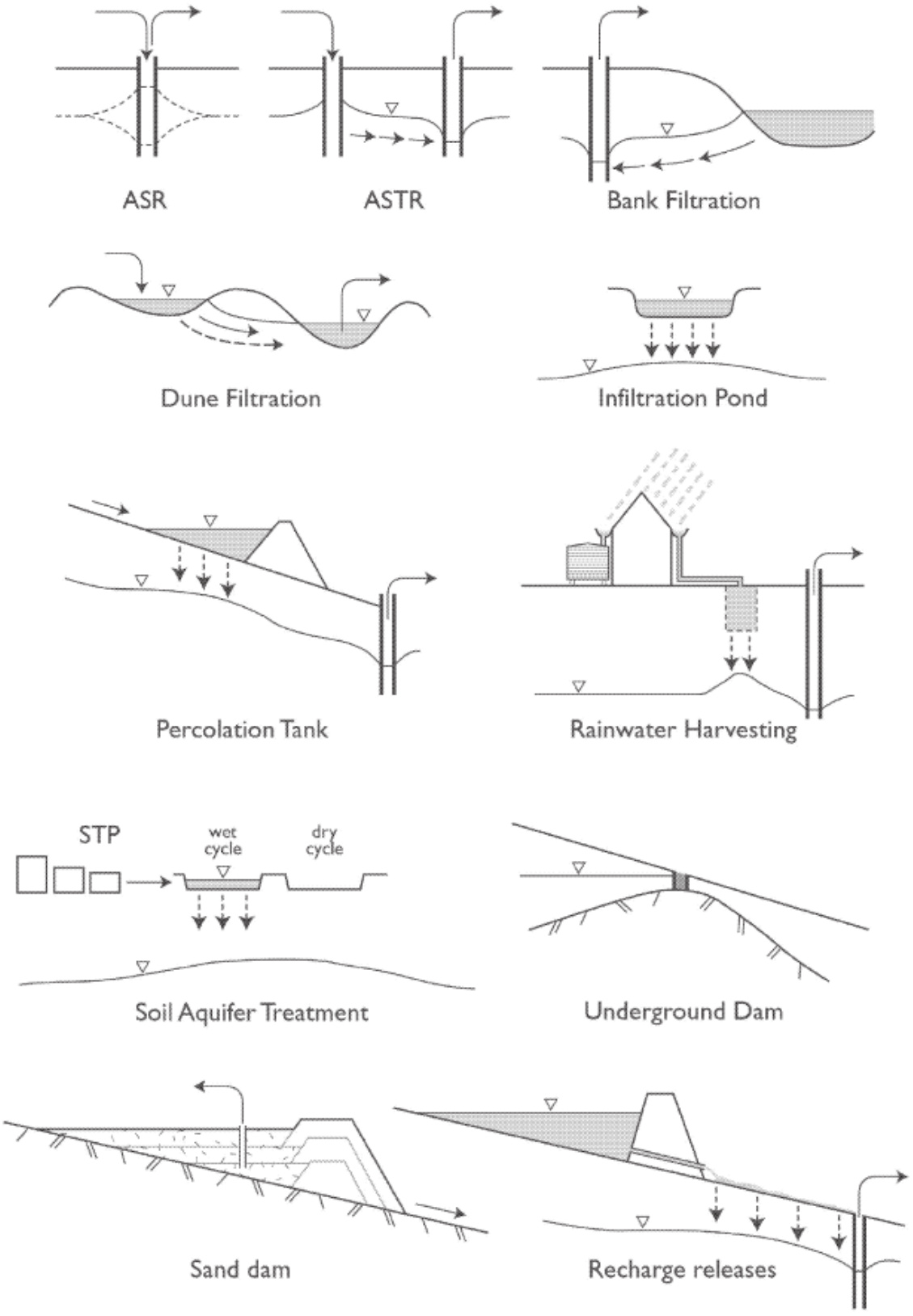

Figure 2.3: Types of MAR after Dillon (2005).

regarding clogging of fine material suspended in the surface water. The ponds have to be cleaned from the fine material from time to time since it decreases the infiltration rate rapidly.

- **Percolation ponds:** Water storage in ephemeral wadis to enhance storage in unconfined aquifers. Dams can be build from in-situ river bed material. The structures can additionally reduce soil erosion, the destructive energy of flash floods, and sediment transport.
- **Rainwater harvesting:** Collection of roof runoff and infiltration through a well or a sand/gravel filled caisson.
- **Soil aquifer treatment (SAT):** Infiltration of pre-treated sewage through ponds for further purification in the vadose zone and recovery through wells. SAT is an extension of infiltration ponds. Treated wastewater is recharged through a preferably thick vadose zone for purification during percolation through the vadose zone. The Shafdan site in Israel (Figure 2.1), which will be intensively discussed in the third case study of this thesis, is one of the largest SAT facilities in the world and successfully operated since more than three decades (Icekson-Tal et al., 2012). For further details, it is referred to Chapter 5. For SAT systems, the infiltration process is very important, from a physical point of view, but also from the biological and chemical perspective since during percolation through the vadose zone, biological and chemical components in the fluid are degraded.
- **Underground dams:** Subsurface dams are built in ephemeral streams where groundwater flow is constricted by basement highs. The groundwater is reclaimed from wells or series of wells.
- **Sand dams:** Storage of runoff water in sand dams built in wadis in arid areas. They are a reasonable solution in areas of flash floods. The flood will be slowed down and coarse, suspended material settles out. The material accumulates with time and the dam wall can also be raised with time. This creates an artificial aquifer with time and water can be abstracted via wells.
- **Recharge releases:** Dams in ephemeral streams with releases of stored water downstream and infiltration into the underlying aquifer. This is an extension of percolation ponds, with a release through pipes and the recharge occurring further downstream in the riverbed. Suspended solids settle down before recharge, which reduces clogging.

Some of these methods are very easy to implement and only need little engineering knowledge (e.g., water harvesting techniques), other methods already require some design and more knowledge (e.g., storage dams, spillways) and e.g., construction of wells or injection boreholes need further engineering expertise. But also the operation of MAR systems requires a good knowledge of the involved hydrological and physical processes.

There can also be a combination of different types of MAR. The most important types appearing in this thesis are aquifer storage and recovery, infiltration ponds and soil aquifer treatment.

2.1.2 Geology and Hydrogeology

The local geological and hydrogeological settings decide if an MAR implementation can be feasible or not. Some important factors have to be considered, which are (Gale, 2005):

- the geometry and boundaries of the aquifer and surrounding formations,
- the hydraulic properties of the aquifer and the vadose zone,
- the groundwater level and vadose zone thickness,
- the quality of the groundwater, and
- the mineralogy of the aquifer.

In cases where water infiltration from the surface is planned, the surface and the vadose zone need large attention since those limit the infiltration process first of all. Parameters influencing the feasibility for MAR are the vertical hydraulic conductivity of the vadose zone, the permeability, transmissivity, and storativity of the aquifer, and the thicknesses of vadose zone and aquifer. If an aquifer has only low storage capacity it can receive only very limited amounts of additional water (Gale, 2005).

The categories of aquifers that are suitable for MAR, are (a) alluvial deposits, (b) fractured hard rock, (c) consolidated sandstone aquifers, and (d) carbonate aquifers (Gale, 2005). However, a porous aquifer is more favorable compared to a fractured or karstic aquifer. Recharge from the surface to unconfined aquifers is more cost-effective than to confined aquifers (Steinel, 2012). Thus, an unconfined porous aquifer with a thick unsaturated zone has in general the highest storage capacity and is therefore most suitable for MAR.

2.1.3 Water Sources

There exist several sources of recharge water, i.e., surface water, runoff water, treated wastewater or potable supply water. The source water can vary in availability, quantity, and quality. Some source water need to be pre-treated due to their quality. The understanding of the groundwater and its interactions with the recharge water is very important (Gale, 2005). A short summary of the main sources will be given (after Gale, 2005):

- **Surface water:** Water from rivers or lakes is recharged directly via bank filtration, but can also be diverted into recharge facilities. Rivers can carry considerable quantities of suspended load which can result in clogging. Therefore, settling ponds can be used before the water is led into infiltration ponds. Water quality has to be considered when rivers or lakes may be polluted from waste discharges.

- **Runoff Water:** Runoff water or storm water can vary strongly in quantity, mainly depending on rainfall. But also the quality can change, especially in urban areas, where storm water can be contaminated with various sources from surface materials. This water should be recharged through the vadose zone for further purification before reuse. Water from rooftops has high quality and is recharged directly into the aquifer through wells.

- **Treated wastewater:** Wastewater is usually treated in waste water treatment plants (WWTP) and then used for recharge. The quantity and quality of the treated sewage is reasonably constant over time. Since the water after treatment is in most cases still not in potable water quality, it is directed to spreading basins for further treatment, the so called soil aquifer treatment (SAT) (see Chapters 2.1.1 and 5). The reclaimed water can then be used for agricultural purposes.

- **Potable supply water:** High quality water can also be used for recharge and is very common to be used. The subsurface storage of high quality water is a very sustainable method. In the majority this is done in ASR and ASTR systems (see Chapters 2.1.1 and 6), where the source water is injected through a well into a confined aquifer where the potable water creates a bubble within the native groundwater.

2.1.4 Planning and Implementation of MAR

MAR implementations need special planning and engineering design (EWRI/ASCE, 2001). The planning of the MAR project is one of the most important processes for a successful implementation (Maliva and Missimer, 2010). Many aspects have to be assessed for an MAR site. First of all, the water supply needs to be determined. Preliminary activities involve data collection, resources evaluation, conceptual plan determination, and environmental assessments. Here, a useful method is the MAR suitability mapping in order to find suitable catchment areas and aquifers. Rahman et al. (2012) developed a tool based on spatial multi-criteria decision analysis for the site selection. Considerations regarding the aquifer are about its storage capacity, how quick the recharge water can infiltrate and if the recovery of the water satisfies quantity and quality (Steinel, 2012).

Also very important is the public involvement, since the most people are not familiar with MAR; and in the first place, infiltration of water into the ground on purpose may appear strange to many people. The next step would be feasibility studies, field investigations and testing programs before the final design of the site is created and given in engineering and environmental reports. Again here, the public involvement is important. The following phase contains the construction of the site and start up. During operation of the MAR project, maintenance, project reviews and project modifications are needed.

2.1.5 Challenges with MAR

One main problem with MAR is clogging (either mechanical, chemical or biological) of the pond surface material, shallow subsurface material or sediments close to the well. It can decrease, for instance, the infiltration rate of a pond dramatically (up to two to three orders of magnitude (Steinel, 2012)). Especially with low soil hydraulic conductivity in the first place; but also thin layers of low hydraulic conductivity can reduce the infiltration rate. For instance, flash floods in arid areas carry huge amounts of suspended solids that will settle down as soon as the streaming velocity is very low. This is usually the case in the infiltration pond and therefore the pond surface can be clogged very quickly.

Increased salt accumulation can be the result of return flow of irrigation water after evaporation. Also generally, contamination can occur through the infiltration water, the soil or the groundwater.

Other problems can be misconception of the local hydrogeology and/or geology (leading to, e.g., too low storage capacity or contamination) or poor design of the infiltration structure or well. Biological and/or chemical processes that occur within the vadose zone or the aquifer can have a negative impact on the water quality.

Under high water fluxes in the vadose zone with ponding conditions, as it is the case at the Shafdan SAT site (see Chapter 5), entrapped air can decrease the infiltration rate. The pore filling air within the vadose zone is pushed down by the water front infiltrating from the surface to the groundwater table, thus called entrapped air. At some point, this air naturally moves upwards through the infiltrating water and by this decreases the infiltration velocity. As part of the same research project as in the study in Chapter 5, the effect of entrapped air was investigated in column experiments by Mizrahi et al. (2016).

As mentioned above, a detailed knowledge of the subsurface system is required for successful implementation and operation of MAR.

2.2 Geophysical Characterization and Monitoring Techniques

The most common geophysical methods for the characterization and monitoring in hydrogeological studies are the methods of Electrical Resistivity Tomography (ERT) and Ground-Penetrating Radar (GPR). In this thesis, ERT is the key method and applied in all three studies. Additionally, the methods of GPR as well as refraction seismics are applied in order to support the results of the geoelectrical investigations.

This section provides a short summary of the concepts underlying the geophysical methods that were applied in this thesis, with a focus on the (time-lapse) electrical resistivity method and two short sections about ground-penetrating radar and refraction seismics, respectively. Some more details about the theory of the methods will also be given in the case studies.

2.2.1 Geoelectrical Imaging

Today, the method of geoelectrical imaging is increasingly being used in the field of hydrological and environmental investigations due to the relation between electrical conductivity and groundwater conduction and/or water saturation as well as water salinity (e.g., Binley and Kemna, 2005; Revil et al., 2012; Binley et al., 2015, and references therein). The broad distribution is also due to some further great advantages of the method, such as that it is non-invasive, thus the study area is not disturbed which reduced costs for drilling or excavations. Furthermore, it is fast and cheap in application.

The electrical DC-method, first established by the Schlumberger brothers, is based on a four-electrode array. It involves the injection of an electrical current through two electrodes into the subsurface and the measurement of the resultant electrical potential difference between another pair of electrodes. By applying Ohm's law, the electrical transfer resistance can be calculated. The true value of the electrical resistivity (ρ) of the subsurface or its inverse, the electrical conductivity (σ), is depending on the geometry of the electrodes and its (in nature always) heterogeneous distribution in the subsurface. Applying this four-electrode method along a line on the surface and/or in boreholes with multiple electrodes and a combination of many (hundreds or thousands of) measurements, this creates the tomographic approach of the resistivity method (e.g., Daily et al., 2004, and references therein). Through special inversion algorithms (e.g., Loke and Barker, 1996; Kemna, 2000), the measured apparent electrical conductivities are converted into images of effective electrical conductivities; thus called, according to the terminology in medical imaging, electrical resistivity (or resistance) tomography (ERT).

Applied in a time-lapse manner (i.e., repeating measurements over time for the same array), ERT provides a tool for monitoring, for instance detecting a moving water body in the vadose zone, seawater intrusion in coastal areas, or a salt tracer in the saturated zone (e.g., Vereecken et al., 2006). From these results, it is possible to define flow and transport parameters (e.g., Kemna et al., 2002).

The direct dependency of the electrical conductivity to the water saturation and/or the water salinity can be described by means of petrophysical models. One of the first descriptions was developed by Archie (1942)

$$\sigma_b = \frac{1}{F}\sigma_w, \tag{2.1}$$

where σ_b is the bulk electrical conductivity of the soil, σ_w is the electrical conductivity of the pore fluid, and F is the formation factor, accounting for the pore space geometry, defined as

$$F = \frac{\mathrm{a}}{\phi^m}. \tag{2.2}$$

Here, a is the tortuosity factor, ϕ is the porosity, and m is an empirical factor, namely the cementation index. Archie found that also the water saturation S is correlated with the electrical conductivity and expanded Equation 2.1 to

$$\sigma_b = \frac{\phi^m}{\mathrm{a}}\sigma_w S^n, \tag{2.3}$$

with n referred to as the saturation index, another empirical factor. In the case of saturated conditions, $S = 1$ and the electrical conductivity can be directly related to variations in fluid salinity (i.e., Equation 2.1).

However, the classical approach of Archie is only limited to sand sediments. With increasing content of silt or clay, the surface conductivity (σ_s) of the mineral grains play a significant role and will contribute to the bulk electrical conductivity, which is accounted for in the approach of, for instance, Linde et al. (2006):

$$\sigma_b = \frac{1}{F}[S^n\sigma_w + (F-1)\sigma_s]. \tag{2.4}$$

Also the approaches of Waxman and Smits (1968) and Revil (2013) include the surface electrical conductivities. Further petrophysical models can be found in Lesmes and Friedman (2005).

As already mentioned in the introduction of the thesis (Chapter 1), only few studies exist using geophysical, especially geoelectrical methods, in applications of MAR. In this thesis, the method of (time-lapse) ERT is used in all studies. In the first study (Chapter 3), a synthetic time-lapse ERT experiment, monitoring water infiltration, was simulated. In the second study (Chapter 4) ERT is used in combination with seismic surveys to characterize the geometry of an alluvial basin and time-lapse ERT of an infiltration experiment is used to characterize the subsurface. In Chapter 5, time-lapse ERT monitors the water infiltration in the vadose zone under ponding conditions with high water fluxes and in the fourth study (Chapter 6), cross-hole time-lapse ERT is applied to a freshwater injection experiment in a hyper-saline aquifer.

2.2.2 Ground-Penetrating Radar

GPR is an electromagnetic method in the frequency range of a few MHz to a couple of GHz. It uses a transmitting antenna to send an electromagnetic wave into the ground and a receiving antenna to capture the wave. The wave is either directly send from the transmitter to the receiver or reflected on lithological and/or anthropogenic patterns in the subsurface. The waves can be visualized in a radargram showing the radar pulses over time and space, and the travel time and amplitude of the waves are measured. GPR is sensitive to the dielectric permittivity and the electrical conductivity of the subsurface (Vereecken et al., 2005).

Depending on the aim of investigation, measurements with GPR can be performed in various ways, meaning the geometric orientation of the antenna pair, i.e., both antennas on the surface, both in boreholes, or a combination of surface and boreholes. For borehole applications the antennas can be used within one borehole or between two boreholes (the so-called cross-hole method). The antennas can have a fixed separation and moved along a profile, or the distance between them is increased around a virtual point, thus resulting in a 1D sounding.

GPR can address hydrogeological questions like the geological structure and material properties (Annan, 2005). The subsurface material (including pore-filling fluid) influences the velocity and the amplitude of the electromagnetic wave. Thus, the detected signal can be used for analyzing water content, salinity, porosity, grain size, and clay content (e.g., Topp et al., 1980; Davis and Annan, 1989).

The volumetric water content θ, for instance, can empirically be related to the relative dielectric permittivity ε_r (e.g., Topp et al., 1980)

$$\theta = -5.3 \cdot 10^{-2} + 2.9 \cdot 10^{-2}\varepsilon_r - 5.5 \cdot 10^{-4}\varepsilon_r^2 + 4.3 \cdot 10^{-6}\varepsilon_r^3. \tag{2.5}$$

ε_r is defined as $\varepsilon_r = \varepsilon/\varepsilon_0$, where ε is the dielectric permittivity and ε_0 is the dielectric permittivity in free space (Vereecken et al., 2005). By measuring the velocity of the electromagnetic wave v, the real part of the relative dielectric permittivity ε_r' relates by

$$v = \frac{c_0}{\sqrt{\varepsilon_r'}} \tag{2.6}$$

where c_0 is the vacuum propagation velocity of electromagnetic waves. Thus, the velocity of the electromagnetic wave decreases with increasing water content. Qualitatively, this can be seen by late arrival times of the waves in the radargram. However, the signal strength of the wave is attenuated with increasing water content, limiting the depth of investigation of the GPR method.

Cross-hole GPR measurements are used to describe the unsaturated zone of the infiltration basin for SAT in the study in Chapter 5 in order to compare the results with the ERT data.

2.2.3 Refraction Seismics

In seismic methods, a mechanical wave is by means of an artificial seismic source (hammer, falling weight, or explosives) send into the subsurface and its propagation at the surface as well as its seismic echoes in the subsurface are detected via a series of geophones (for an overview, see e.g., Telford et al., 1990). Once a seismic wave is generated, different types of surface and ground waves are created and spread with different characteristics. In Refraction Seismics (RS), the compressional wave (p-wave) is of interest.

For the case of a lithological layer with high p-wave velocity underlying a layer with lower p-wave velocity, the critical refracted wave is generated at the layer boundary and can be detected by the geophones; the velocities can be estimated from the seismogram. This principle is based on Snell's law from the ray theory (Telford et al., 1990). By using this law, the thickness of the upper layer can be calculated. However, this method is limited to cases where the seismic velocities increase with depth, which is required for the generation of the critically refracted wave; this phenomenon is encountered in most shallow applications (Vereecken et al., 2005).

For shallow MAR applications, RS is the method of choice for the characterization and delineation of the geology of the site; like the thickness of the vadose zone or aquifers and their geometry. Table 2.1 gives an overview of seismic velocities in different unconsolidated and consolidated sediment rocks. With seismic methods it is also possible to quantify material properties of the subsurface, for instance porosity, hydraulic conductivity, elastic moduli, and water saturation (Vereecken et al., 2005).

RS are used in the study in Chapter 4 to delineate an alluvial basin (intended for subsurface water storage) to its underlying rock basement and by that calculating the thickness of the alluvial sediments.

Table 2.1: Sesimic p-wave velocities of selected unconsolidated sediments, rocks, and fluids (excerpted from Knödel et al., 2007).

Material	**Velocity v_p (m s^{-1})**
Clay	500 - 2,800
Sand	100 - 2,000
- dry	100 - 600
- wet	200 - 2,000
- saturated	1,300 - 1,800
Gravel	180 - 1,250
Weathering layer	100 - 500
Sandstone	800 - 4,500
Chalk	1,800 - 3,500
Limestone	2,000 - 6,250
Air	310 - 360
Water	1,430 - 1,590
Saltwater	1,400 - 1,600

Chapter 3

Geoelectrical Monitoring of Water Infiltration: A Numerical Feasibility Study

Parts of this study were published in the proceedings of the conference on Integrated Water Resources Management:

Klaus Haaken, Christoph Oberdörster, Martin Sauter, and Andreas Kemna 2011. Time-lapse electrical imaging as a tool for monitoring and quantification in managed aquifer recharge applications: a numerical feasibility study. *Proceedings of the International Conference on Integrated Water Resources Management (IWRM)*, Dresden, Germany, October 12-13.

3.1 Introduction

Water infiltration into and through the unsaturated zone can be a complex process, as described in Section 2.1; and especially in case of a heterogeneous subsurface in terms of sedimentation and hydraulic characteristics. Thus, with this increasing complexity, also the management of water infiltration in the context of MAR becomes challenging. Knowing the relevant quantities (like the infiltrated water volume) is of great importance, for instance to know if the infiltrated water can be completely recovered or if parts of the water is lost due to whatever reason. On the surface it is possible to measure the quantity of water flowing through a defined stream, however its movement below the surface is difficult to be seen and to be measured.

This is possible with using the geophysical method of ERT. As shown in Section 2.2.1, by using a petrophysical relationship the measured electrical conductivity can be related to water saturation. In order to test this phenomenon in the case of MAR, a synthetic numerical experiment was carried out to simulate ponded water infiltration as well as time-lapse ERT measurements for the monitoring of water infiltration. The aim of the study is to show the potential of time-lapse ERT in order to characterize the subsurface under hydrological aspects and to quantify the infiltrated water volume. It is designed as a feasibility study for vadose zone MAR applications, like surface infiltration (see Section 2.1.1) as it could be the case in the study in Chapter 4.

A comparable approach of quantifying recharge in mantled sinkholes using time-lapse ERT was conducted by Schwartz and Schreiber (2009). They converted the measured electrical 2D profiles via Archie's law (see also Section 2.2.1 and therein Equation 2.3) into volumetric water content and by this monitored temporal changes in water content. Their results showed that recharge in mantled sinkholes can appear as both, rapid and slow recharge.

In this synthetic study, an approach of quantifying water volume using time-lapse ERT data is presented. It uses the changes in electrical conductivity, caused by the changes in water saturation and integrates these changes over space and time. By relating the true, modeled data with the inverted results, a recovery rate can be calculated indicating the recovery of the infiltrated water volume from the inverted time-lapse ERT data. In addition, three different ERT setups in terms of electrode position are compared: two cross-borehole setups with 10 m and 20 m separation between boreholes as well as one surface electrode setup.

This approach can be useful in MAR applications where the measurement of the real infiltrated water volume is difficult to be realized or water losses from the surface have to be accounted for, such as through evaporation.

3.2 Material & Methods

Coupled hydrogeological and geophysical numerical modeling was carried out to simulate electrical resistance measurements in a 2D synthetic, heterogeneous vadose zone during an infiltration experiment using the modeling package iTOUGH2 (for more details, see Pruess et al., 1999; Pruess, 2004; Finsterle et al., 2008). Different levels of noise were added to the simulated ERT data. The ERT measurements were then inverted and the derived resistivity values converted into water saturation. Finally, the inverted results of the changes in water saturation are compared with the "true" saturation values of the hydrological forward simulation, and set in relation. By integrating the results over space and time, this proposes the approach of quantification of the infiltrated water.

3.2.1 Unsaturated Water Flow

For the hydrogeological forward model, vadose zone water flow is described by Richards' equation (Richards, 1931) as implemented in the simulator TOUGH2 (Pruess et al., 1999):

$$\frac{\partial}{\partial t}\theta = \boldsymbol{\nabla} \cdot [K \boldsymbol{\nabla} h], \tag{3.1}$$

where t is time, θ is specific volumetric water content, K is the hydraulic conductivity, expressed as

$$K = k \frac{k_{rel} \varrho g}{\mu}, \tag{3.2}$$

with k the absolute permeability, k_{rel} the relative permeability, ϱ fluid density, g gravitational acceleration and μ the viscosity of the fluid. The hydraulic head h is defined as:

$$h = P + \varrho g z, \tag{3.3}$$

with P the liquid-phase pressure head and z the vertical coordinate (positive upward). $P = P_{ref} + P_c$, where P_{ref} is a reference gas pressure and P_c the capillary pressure. For (nearly) isothermal conditions, variations in fluid density and viscosity can be neglected.

Since relative permeability and capillary pressure are dependent on water saturation, they are described by the van Genuchten-Mualem model (van Genuchten, 1980):

$$k_{rel} = \sqrt{S_e}[1 - (1 - S_e^{m^{-1}})^m]^2 \tag{3.4}$$

$$P_c = -\frac{1}{\alpha}(S_e^{-1/m} - 1)^{1-m} \tag{3.5}$$

Here, S_e is the effective water saturation, m is an exponent regarding the grain size distribution, and α is the air entry pressure. The effective water saturation is expressed as:

$$S_e = \frac{S - S_r}{1 - S_r}, \tag{3.6}$$

with S the actual water saturation and S_r the residual water saturation.

The simulated aquifer here is a heterogeneous sandy soil with areas of lower permeability. The heterogeneous permeability was generated with a sequential Gaussian simulation using Geostatistical Software Libraries (GSLib). The heterogeneous permeability field is shown in Figure 3.1.

The spatial extend of the model domain is 20 m in the horizontal x- and 20 m in the vertical z-direction, with a cell size of 0.25 m by 0.25 m. The infiltration of water was simulated by giving the surface cells (first row) between 8 m and 12 m in x-direction a water saturation of $S = 1$ (thus, resulting in a pond length of 4 m). After 5 days, the infiltration was stopped by giving the same cells a value of

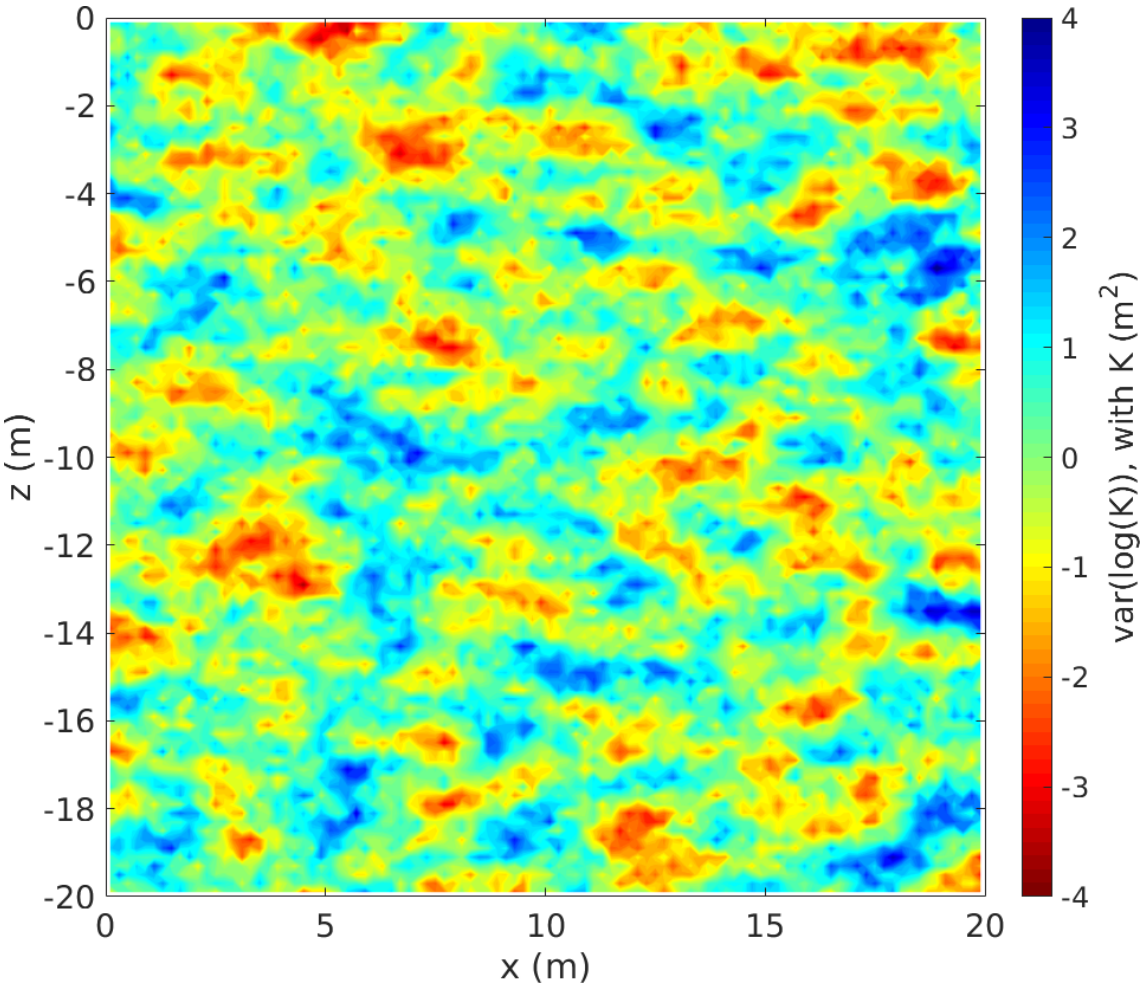

Figure 3.1: Heterogeneous permeability field, plotted as logarithmic variance in permeability, generated using GSLib.

$S = 0$. The groundwater table lies at 17 m below ground surface. The parameters of unsaturated flow related to Richards' equation (Equations 3.1 and 3.2) and the van Genuchten-Mualem model (Equations 3.4 to 3.6) are listed in Table 3.1.

Table 3.1: Model parameters defined for the simulation of unsaturated flow.

Parameter	Symbol	Value	Unit
Permeability (mean value)	K	10^{-11}	m^2
Porosity	ϕ	0.35	-
Residual water saturation	S_r	0.105	-
Grain size distribution index	m	1.66	-
Air entry pressure	α	10^3	-

3.2.2 Geoelectrical Imaging

The geoelectrical forward model was simulated using the code CRMod (for more details, see Kemna, 2000), implemented within the iTOUGH2 code (Finsterle, 2007; Finsterle and Kowalsky, 2008). Here, the electric potential field, Φ, for a current injection between electrodes at $\boldsymbol{r}_{S+}$ (current source) and $\boldsymbol{r}_{S-}$ (current sink) is calculated by solving the Poisson equation

$$-\boldsymbol{\nabla} \cdot [\sigma_b \boldsymbol{\nabla} \Phi] = I[\delta(\boldsymbol{r} - \boldsymbol{r}_{S+}) - \delta(\boldsymbol{r} - \boldsymbol{r}_{S-})], \tag{3.7}$$

together with appropriate boundary conditions, where σ_b is the given electrical conductivity distribution, I is the injected current strength, and δ is the Dirac delta function.

The relation between the hydrological and electrical model is described by means of a petrophysical model after Archie (1942) (see Equation 2.3). Figure 3.2 shows the relation between electrical resistivity and water saturation for the Archie model. The parameters were chosen for typical values of sand from the literature and are listed in Table 3.2. The surface conductivity was neglected in this study.

Table 3.2: Archie parameters defined for the synthetic study.

Parameter	Symbol	Value	Unit
Porosity	ϕ	0.35	-
Elec. fluid conductivity	σ_w	10^{-3}	S m^{-1}
Cementation index	m	1.8	-
Saturation index	n	2.0	-

For the forward ERT model, we performed three different simulations for different electrode setups: two cross-borehole arrays with a separation of 10 m and 20 m between the boreholes, respectively and one array on the surface.

Both cross-borehole arrays consist of 51 electrodes, where 21 electrodes are positioned in each borehole, separated by 1 m (resulting in 20 m borehole depth with the first electrode at the surface) and 9 electrodes are situated on the surface between

the boreholes with a separation of 1 m for the 10 m boreholes and 2 m for the 20 m boreholes. The grid of the model is 20 m by 20 m (as for the hydrogeological model). The 2D electrical grid is set as a vertical plain in the middle of the model domain in x- and y-direction, respectively.

The surface array consists of 48 electrodes with 1 m separation and a gap of 4 m in the center at the position of the infiltration pond. The total grid is 50 m in x-direction and 10 m in y-direction (as for the hydrogeological model; note that for the surface ERT setup also a different heterogeneous permeability field was generated with GSLib, but not shown here).

The simulated ERT measurements were inverted using the smoothness-constraint imaging code CRTomo (also here, for more details, see Kemna, 2000, and Section 5.2.3.2). Based on a finite-element discretization, the code computes the smoothest possible distribution of electrical conductivity, or its reciprocal, the electrical resistivity, in a 2D image plane explaining the given data set. Here, an objective function $\Psi(\boldsymbol{m})$ is iteratively minimized, which is composed of the measure of data misfit and first-order model roughness, with both terms being balanced by a regularization parameter λ:

$$\Psi(\boldsymbol{m}) = \|\boldsymbol{W}_d[\boldsymbol{d} - \boldsymbol{f}(\boldsymbol{m})]\|^2 + \lambda\|\boldsymbol{W}_m\boldsymbol{m}\|^2, \tag{3.8}$$

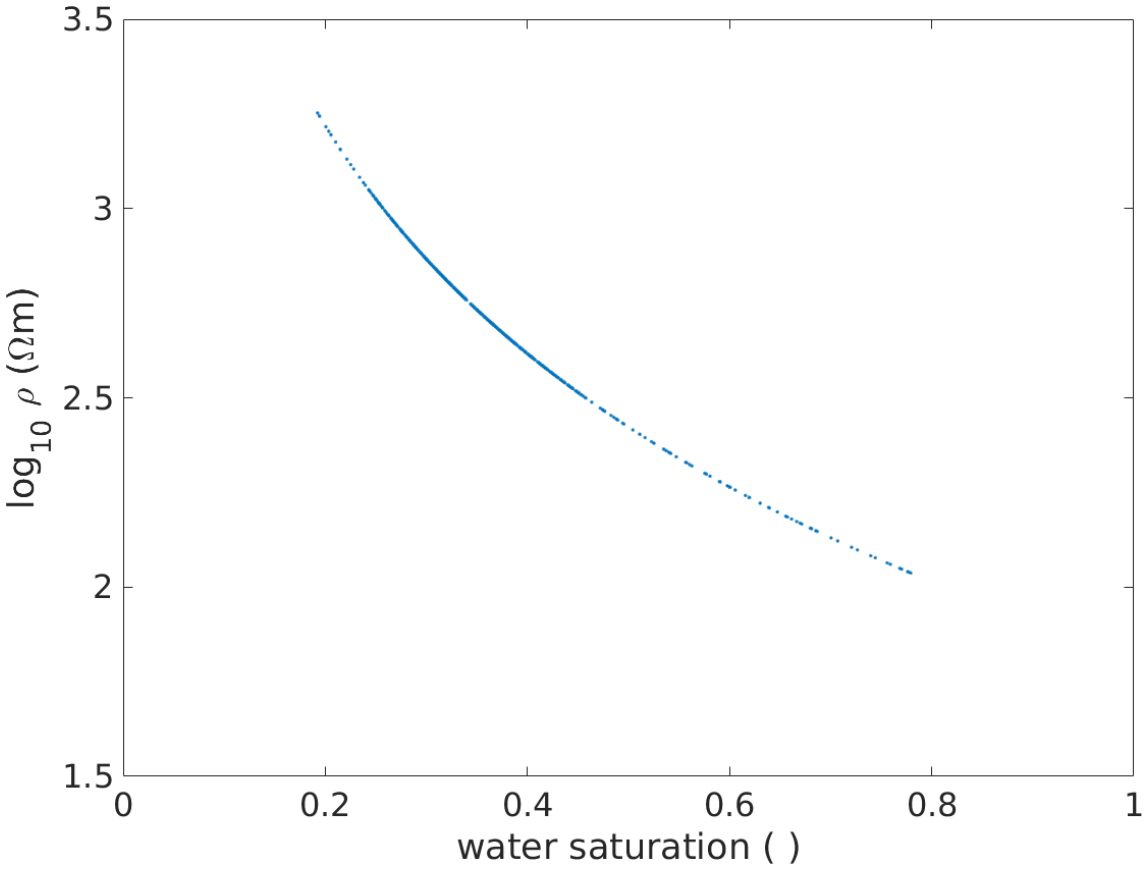

Figure 3.2: The petrophysical model after Archie, the graph shows the relation between electrical resistivity and water saturation.

where $\boldsymbol{d}$ is the data vector (log resistances), $\boldsymbol{m}$ the model vector (log resistivities of parameter cells), $\boldsymbol{f}(\boldsymbol{m})$ the operator of the forward model, $\boldsymbol{W}_d$ a data weighting matrix, and $\boldsymbol{W}_m$ a matrix evaluating the first-order roughness of $\boldsymbol{m}$. Assuming the data errors are uncorrelated and normally distributed, $\boldsymbol{W}_d$ is a diagonal matrix given by

$$\boldsymbol{W}_d = diag\{\frac{1}{\epsilon_1}, \cdots, \frac{1}{\epsilon_N}\}, \tag{3.9}$$

where ϵ_i is the error estimate (standard deviation) of the i-th datum, $\epsilon_i = {}^{\Delta R_i}/_{R_i}$, and N the number of measurements. At each iteration step of the inversion, a univariate search is performed to find the maximum value of the regularization parameter λ which locally minimizes the data misfit.

Resistivity images exhibit a variable spatial resolution (e.g., Ramirez et al., 1995; Alumbaugh and Newman, 2000; Nguyen et al., 2009). A useful indicator for this variation is the cumulative sensitivity $\boldsymbol{s}$ (e.g., Kemna et al., 2002; Nguyen et al., 2009) which as L1 norm measure is given as:

$$\boldsymbol{s} = \sum_i \frac{|a_{i,j}|}{|\epsilon_i|}, \tag{3.10}$$

where $a_{i,j}$ is the sensitivity of the i-th datum with respect to the j-th parameter. The sensitivity indicates how a change in electrical resistivity of a certain model cell (j) affects a transfer resistance measurement (i). Analogously, the cumulative sensitivity quantifies the change of a complete dataset to a changing model cell. In a qualitative manner one can assume that a cumulated sensitivity clearly below 10^{-3} leads to a weak imaging.

3.2.3 Recovery Rate

The obtained electrical resistivities after ERT inversion were back-transformed to water saturation based on the adopted petrophysical model (Equation 2.3). For evaluation, the differences of water saturation S at each time step t to water saturation at time step t_0 (i.e., the model start before infiltration) were calculated for the model domain around the area of interest in the 2D domain:

$$\Upsilon(t) = \iint_{XZ} (S(t) - S(t_0))dxdz. \tag{3.11}$$

For comparison of the inverted time-lapse ERT data with the true model data, this calculation was done for both, the forward model and the inverted images and set in relation. This calculates the recovery rate

$$RR(t) = \frac{\Upsilon(t)_{inverted}}{\Upsilon(t)_{simulated}}. \tag{3.12}$$

Additionally, different noise levels (5%, 10%, and 20%) were added to the simulated ERT data before inversion to evaluate the data misfit in the images and thus, in the quantification of infiltrated water volume.

3.3 Results

The synthetic modeling data were treated as described above and the inverted electrical imaging results are shown in Figure 3.3 for the two cross-borehole ERT setups and in Figure 3.4 for the surface ERT setup. The ERT results reveal the infiltration pattern in the subsurface. Importantly, low and high permeable zones are correctly delineated with the narrow borehole setup. Areas with low permeability show higher water saturation, resulting from higher electrical conductivity; here, the retention time of the water saturation is higher. The opposite phenomenon is observed for the areas with high permeability. The resolution of the images varies for the different ERT setups. A higher resolution can be observed for the narrow borehole setup (10 m separation) than for the wider setup (20 m separation). However, the surface ERT setup shows much smoother images of water saturation; it is not able to delineate low and/or high permeable zones. Note that for the surface setup, the maximum depth of the model domain is only 10 m, compared to 20 m for the two borehole setups.

In particular, the potential of recovering the infiltrated water volume is investigated. Due to spatial regularization, the inverted images are smoother compared to the distribution of the forward model, whereas breakthrough curves (Figure 3.5) and the recovery rate RR shows that the quantities are revealed appropriately, with little underestimation (Figures 3.6a, and 3.6b for the cross-borehole ERT setup). Also for the surface ERT setup (Figure 3.6c), little underestimation can be noticed. The underestimation of ERT inversion results has also been observed for tracer studies (e.g., Singha and Gorelick, 2005; Oberdörster et al., 2010). However, our results exhibit less underestimation.

The underestimation increases with increasing borehole distances, caused by decreasing sensitivities between boreholes and smooth regularization from inversion (Figures 3.7a and 3.7b). These figures clearly show that the coverage distribution in the center between the borehole increases with decreasing borehole distance. Whereas the cumulated sensitivity never falls below 10^{-3} (as set as criteria in Section 3.2.2), it is much larger within the area of interest for the narrow borehole setup than for the wider setup.

Analogously to the borehole setup, the coverage distribution for the surface ERT setup (Figure 3.7c) obviously shows decreasing sensitivity with increasing distance from the electrodes, i.e., here equivalent with increasing depth. In the area of interest, i.e., between around 20 m and 30 m in x-direction, which is around the center of the profile, the cumulated sensitivity never falls below 10^{-3}.

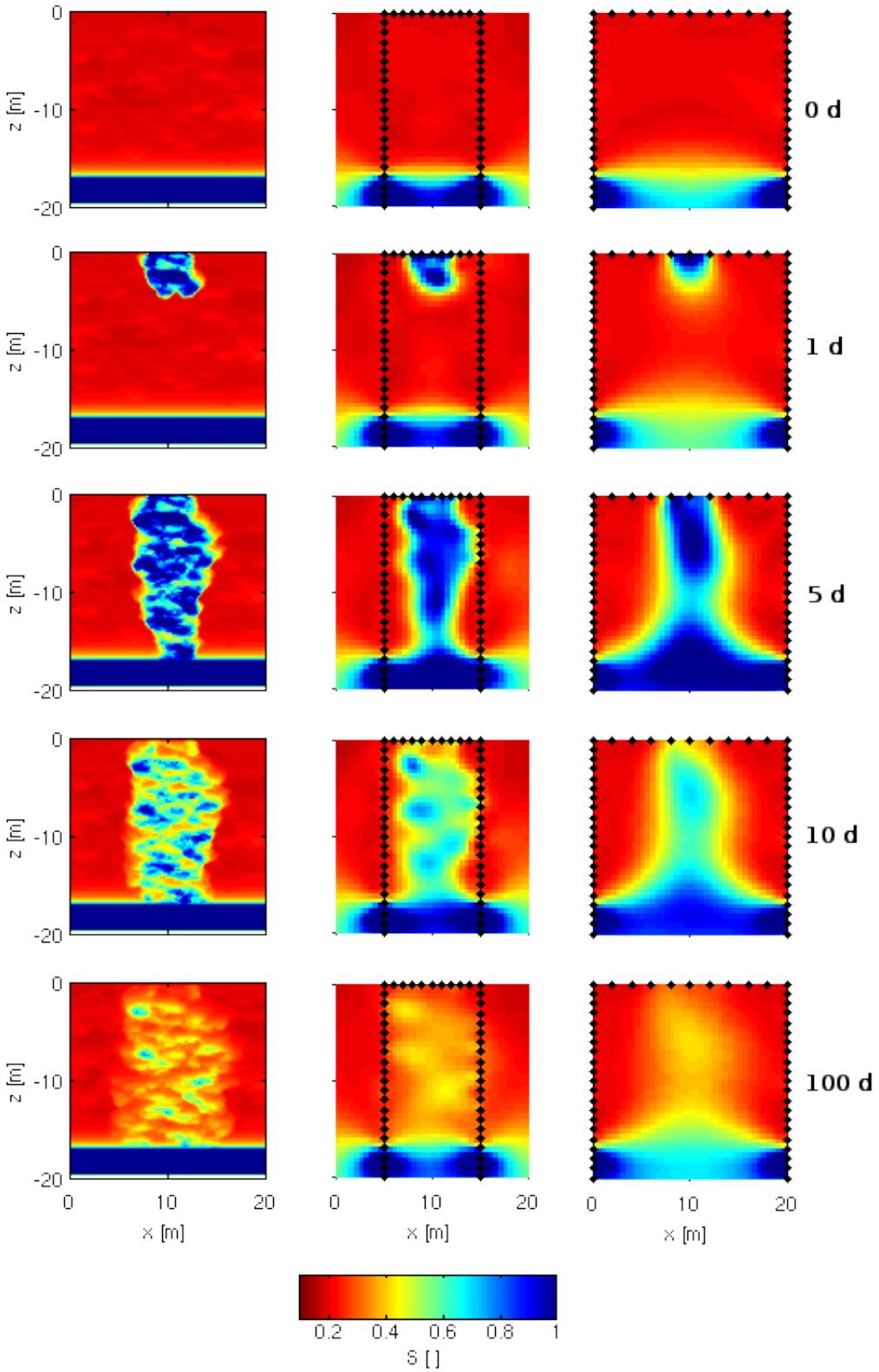

Figure 3.3: Forward and inverse model results for the two cross-borehole ERT setups: First column shows water saturation of the hydrological forward model, second and third column show back-transformed water saturation after inversion of the simulated ERT data with borehole separation of 10 m and 20 m, respectively. The rows denote the different time steps, where the first row demonstrates the prior model at time t_0. Black diamonds denote the position of the electrodes, separated 1 m.

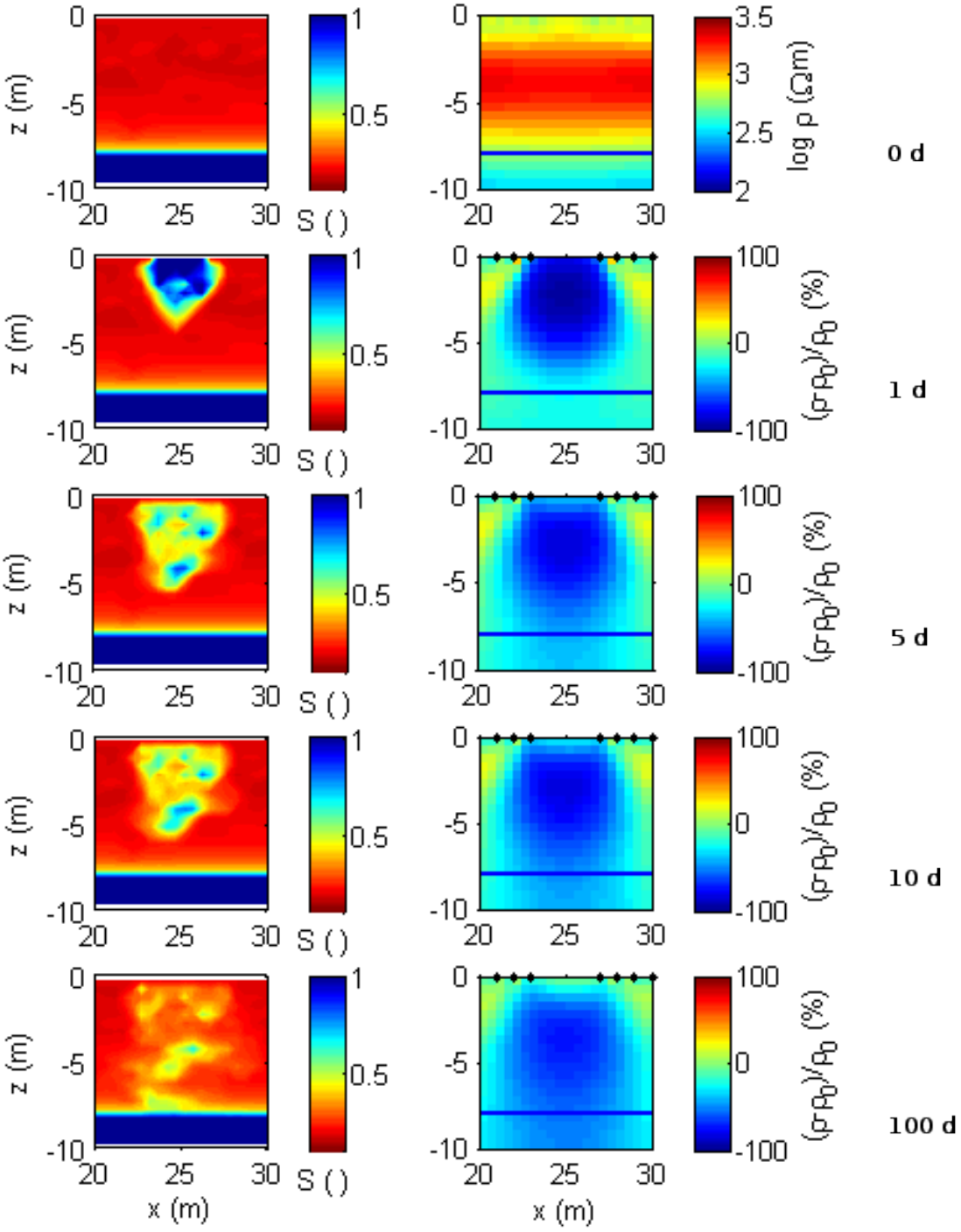

Figure 3.4: Forward and inverse model results for the surface ERT setup: First column shows water saturation of the hydrological forward model and second column shows back-transformed water saturation after inversion of the simulated ERT data. The rows denote the different time steps, where the first row demonstrates the prior model at time t_0. Black diamonds denote the position of the electrodes. Note that the images only show a detail of the entire model domain around the area of interest.

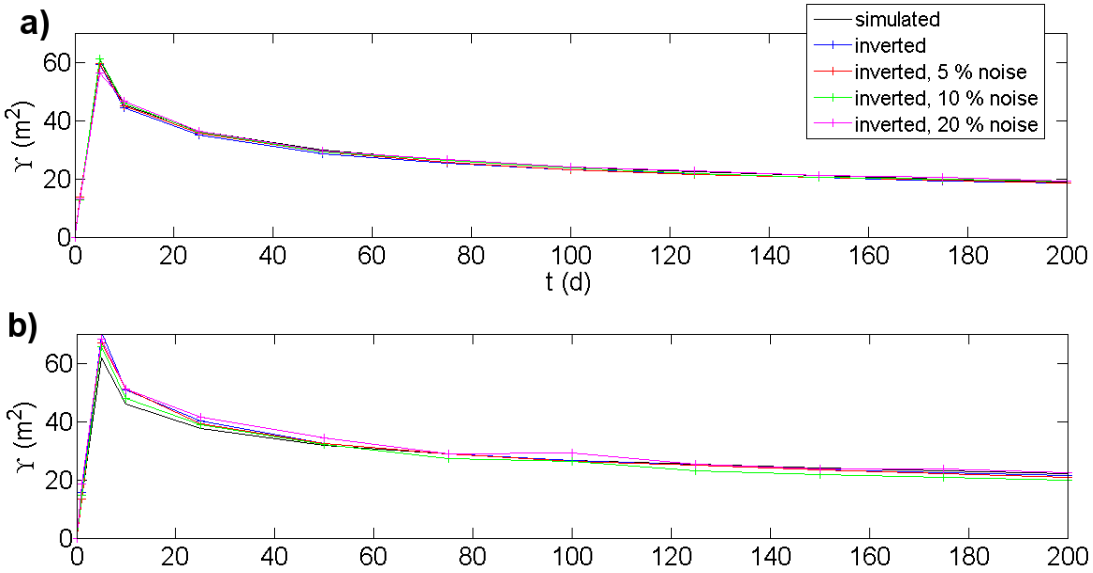

Figure 3.5: Breakthrough curves for Υ for the cross-borehole ERT setups with borehole separation of (a) 10 m and (b) 20 m.

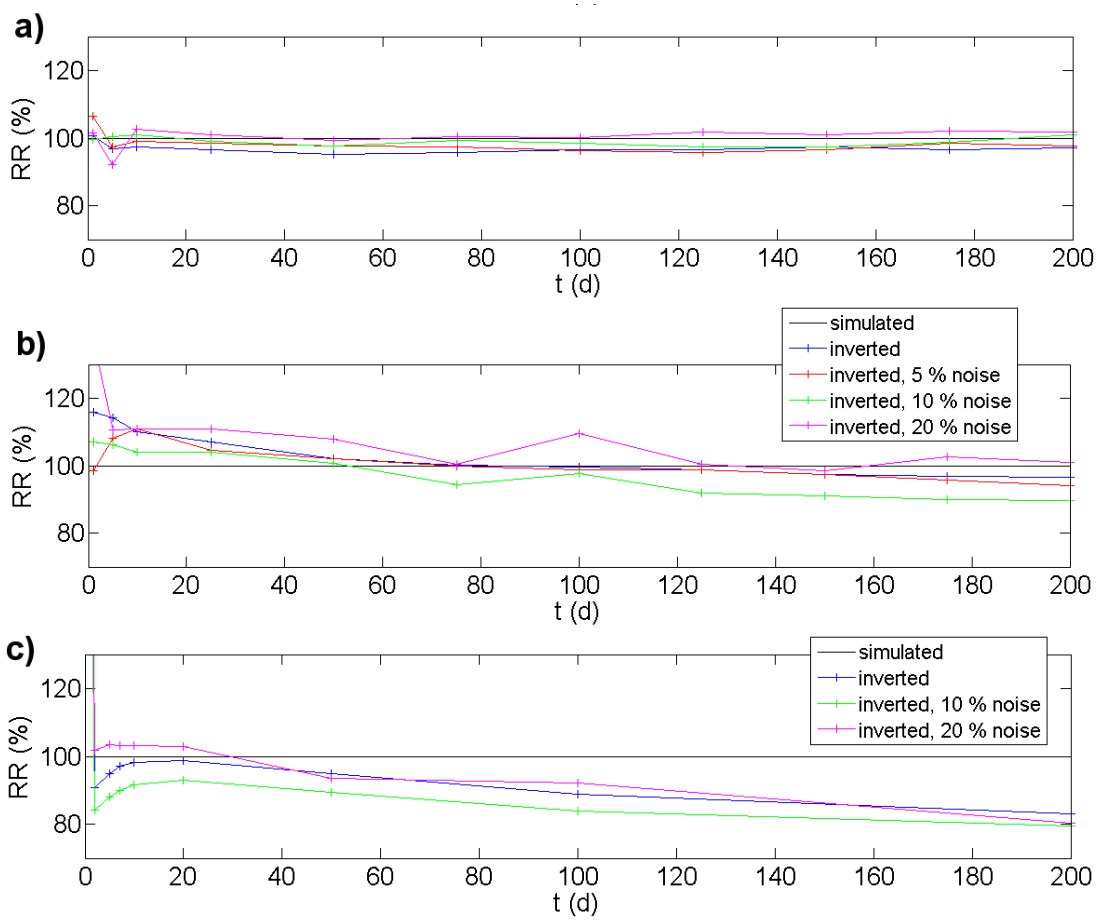

Figure 3.6: Recovery rate RR for the cross-borehole ERT setups with borehole separation of (a) 10 m and (b) 20 m as well as (c) for the surface ERT setup.

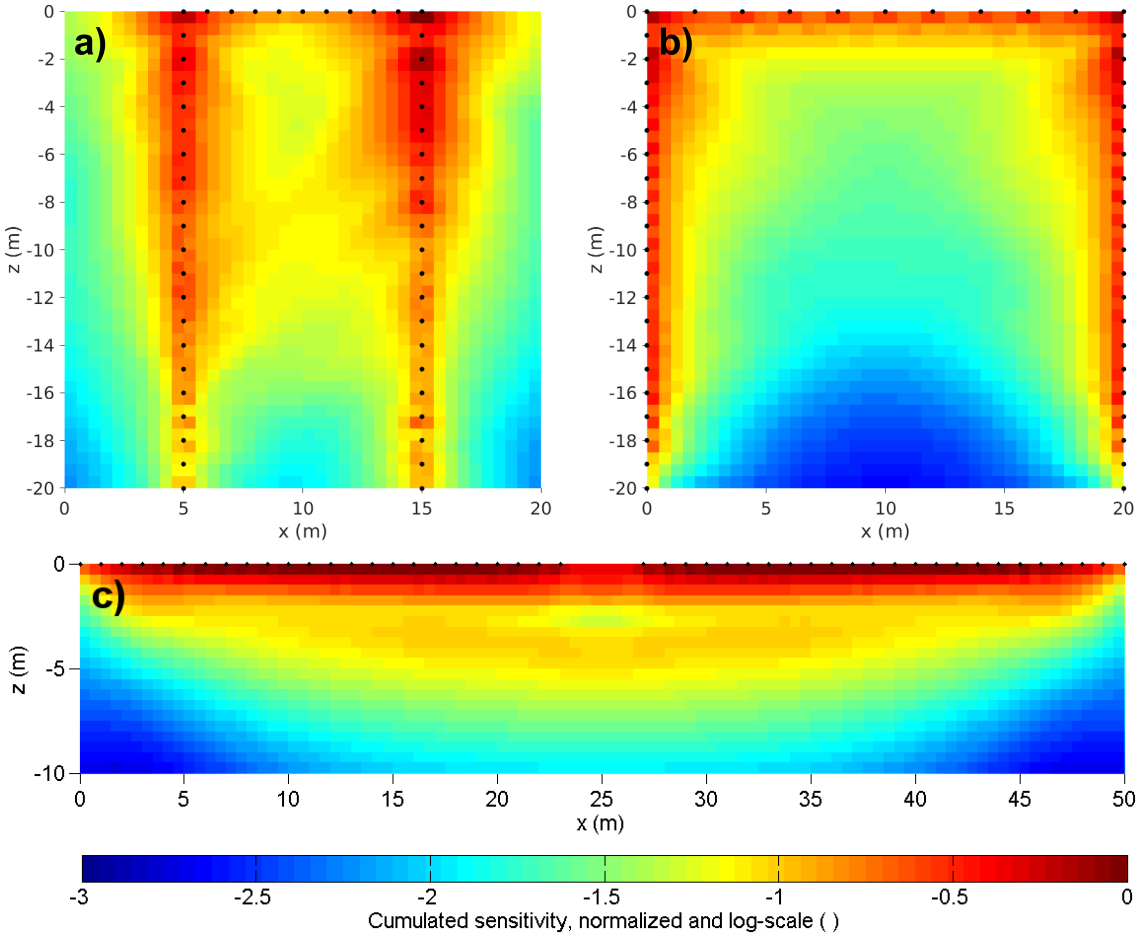

Figure 3.7: Cumulated sensitivity distribution (coverage) for the inversion results of (a) the cross-borehole ERT setup with 10 m borehole separation, (b) the cross-borehole ERT setup with 20 m borehole separation, and (c) the surface ERT setup. Black circles denote the position of the electrodes.

3.4 Conclusions

In this synthetic study, the potential of time-lapse electrical imaging to monitor and quantify water infiltration for MAR was investigated. This was done by a differential inversion approach (time-lapse ERT), where temporal and spatial changes in electrical resistivity caused by changes in water saturation were converted into water saturation using a petrophysical relation. The results show that time-lapse ERT has the potential to quantify relevant quantities of infiltrated water for MAR and therefore can be a powerful tool for the monitoring of MAR applications. However, some knowledge about petrophysical subsurface parameters is required (Archie parameters) that can only be obtained by additional measurements in the laboratory.

Additionally, different ERT electrode setups in boreholes and/or on the surface were compared for the approach. The comparison shows that recovering the relevant quantities depends on the coverage of the ERT method within the area of interest. A narrow cross-borehole setup reveals better results than a wider setup, which is

obvious. A surface ERT setup can only be used for shallow subsurface applications.

On the other hand, without the aim of direct quantification, only the changes in electrical conductivity can be related to changes in water saturation (assuming a constant water salinity and temperature) and by that give an idea of the characterization of hydraulic subsurface heterogeneity (see also Chapter 5).

The delineation over space and time of the infiltrated water within a hydraulic heterogeneous aquifer can be achieved using time-lapse ERT in boreholes and/or on the surface, in order to identify areas where water infiltrates faster or slower. Depending on the correlation length within the heterogeneous aquifer as well as the electrode geometry (distance between boreholes and distance between electrodes), this can be done with high spatial resolution. Extending the ERT data to 3D measurements (and inversion) would lead to even higher resolution and decreasing negative effects on the electrical data.

Chapter 4

Hydrogeophysical Site Characterization for Suitability of MAR

4.1 Introduction

The Lower Jordan River Valley (LJRV), a long and narrow basin, shared by three nations (Israel, Jordan and the Palestinian Authority) has great potential for agriculture. However, due to its arid climate (50 to 150 mm a^{-1} precipitation and potential evaporation of up to 2,600 mm a^{-1}) and further decreasing amounts of rainfall over the last decades, the area is characterized by water scarcity (Hötzl et al., 2009). Rainfall occurs very seasonally in winter times, and heavy rainfalls in the mountains surrounding the valley occur as flash-floods through wadis into the valley. It is tried to keep this runoff water and stored in surface ponds to use it for agricultural irrigation throughout the entire year, and especially in the dry and hot summer season. But lots of water is lost already before storing due to uncontrolled infiltration into the subsurface and runoff through the Jordan river into the Dead Sea. Moreover, large amounts of the captured water evaporate in the hot season or get contaminated by algae growth in the ponds.

Therefore, the controlled storage of water resources in the subsurface is a promising technique for this area to prevent the water from losses like evaporation. The method of managed aquifer recharge (MAR) is the storage of water in aquifers (e.g., Bouwer, 2002; Dillon, 2005; Gale, 2005). It is a sustainable and innovative method in the context of integrated water resources management. And additionally, it is easy and cheap to apply. MAR is already applied successfully in the LJRV, mostly on the eastern side of the river in Jordan. One example is the Wala reservoir east of the Dead Sea in Jordan (e.g., Xanke et al., 2015); a summary of the multilateral project SMART (Sustainable Management of Available Water Resources with Innovative Technologies; *www.iwrm-smart2.org*) with other examples of MAR in the LJRV can be found in Klinger et al. (2015).

However, before implementation of MAR, the knowledge of all involved water resources, aquifers and their (hydro-)geology is crucial (see also Chapter 1). The delineation of basin geometries, characterization of sediments concerning hydraulic parameters and the knowledge of all in- and outflows have to be intensively investigated before planning an MAR site.

Due to strong heterogeneities in the subsurface, conventional hydro-geological techniques like exploration boreholes, pumping tests or soil and water samples, are mostly insufficient to describe spatial structures and the complex flow and transport processes of fluids both in the saturated and unsaturated zones (Kemna et al., 2006). Furthermore, they are expensive, selective and can interfere with the flowing system. Spatial extensive, non- or at least minimally-invasive methods like geophysical investigation techniques provide characterization of the subsurface with high spatial resolution and monitoring of processes during infiltration events. In addition they are more competitive and do not disturb the flowing system. Geoelectrical techniques are among the most used geophysical methods in the field of hydrogeophysical problems (Binley and Kemna, 2005).

Electrical resistivity tomography (ERT) provides spatial and temporal imaging about the distribution of electrical conductivity in the subsurface. Since the electrical conductivity can be correlated with water saturation in the subsurface (Archie, 1942), the movement of the water body in the vadose zone can be detected, as shown in

Figure 4.1: Location map of the working area.

Chapter 3. One should consider the change in electrical conductivity, which can be caused by variation of saline concentrations in the sediment and the fluid. Those effects are anticipated especially in coastal or (semi-)arid areas.

After hydrogeophysical inversion of the measured geophysical characteristics including adequate error models and parameterization, the hydrogeological model will be provided to the intended working area. Here, a characterization will be given due to the reasonability of the applied method of MAR.

In this study, we present a general approach that can be taken as a recipe for future investigations in finding and investigating suitable spots for MAR, especially in arid and semi-arid regions using hydrogeophysical investigation techniques. The approach is presented as a case study where we use geophysical methods to investigate the geological geometry of an alluvial basin in the LJRV (West Bank) and hydrological characteristics of the basin material in combination with classical hydrogeological approaches. Here, we use the methods of refraction seismics (RS) and ERT. RS is used to detect the basement rock of the alluvial basin and by that delineate the thickness of the potential aquifer for subsurface storage. ERT is applied both, as static measurements giving the state of electrical conductivity of the subsurface and by that also detect the basement rock and as time-lapse data, monitoring changes in electrical conductivity due to water movement in the unsaturated zone during an infiltration experiment.

4.2 Site Description

The alluvial basin under investigation is located west of the village Auja (also: Uja) in the Jordan Valley (West Bank), about 10 km north to the city of Jericho (Figure 4.1). It is part of the Jordan Rift Valley, a north-south striking pull-apart basin with a width of 5 km to 9 km in the north to 23 km in the south (Farber et al., 2004). It started to create in the Miocene through the northward and eastward moving Arabian plate, departing from the African and European plates. After its creation, sedimentation and erosion phases alternated within the valley during the Oligocene. The sediments were deposited mainly from the surrounding mountains in the east and the west as clastic sediments from rivers and alluvial fans as well as lake deposits from the Lisan lake, the former Dead Sea (Begin et al., 1974).

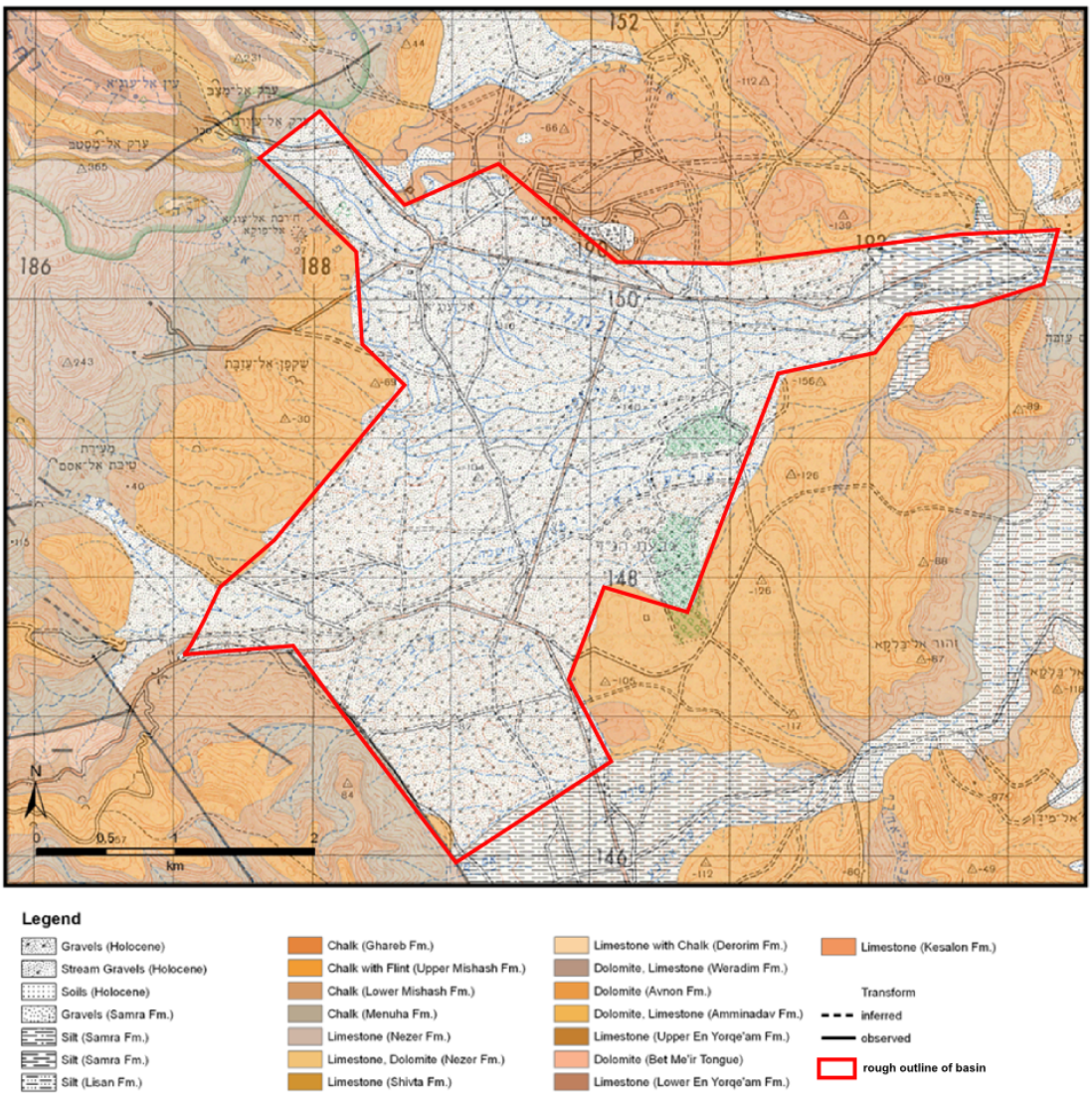

Figure 4.2: Geological map of the alluvial basin west of the village Auja (West Bank). Modified after Begin (1974).

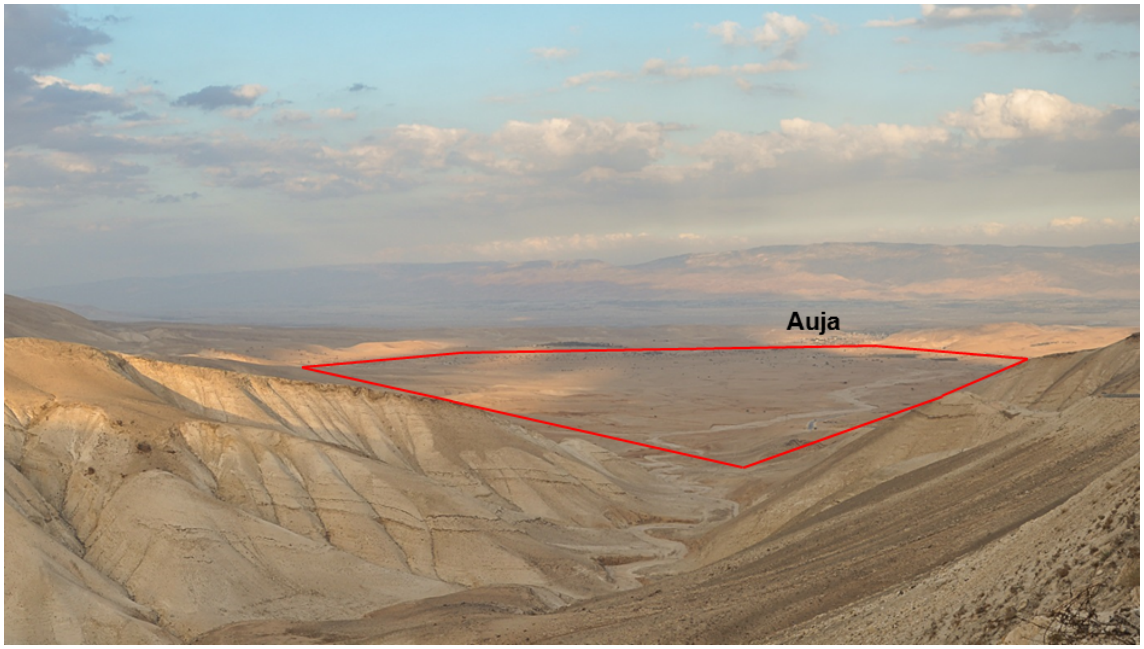

Figure 4.3: Photograph of the alluvial basin, view from southwest to northeast. The basin is marked with the red outline. The village Auja is visible at the northeastern outlet of the basin, in the background the mountains of the eastern margin of the LJRV are visible, already belonging to Jordan.

The Auja basin is an about 3 km by 3 km wide morphological depression with the West Bank Mountains as western and southern margin and a lower hilly section in the east and in the north (Figure 4.3). The basin has its inlet in the north-west through Wadi Auja with Auja spring and a smaller inlet with no significant flow in the south-west. The outlet of the basin into the actual Jordan Valley lies in its north-east, where also the village Auja is situated.

The Auja basin contains clastic sediments from an alluvial fan, deposited during the last glacial period. The sediments are mostly composed of gravels, sands and silts transported from the West Bank Mountains (Figures 4.2 and 4.4c). But also fine material (silt and clay) from lake depositions can be found (Lisan Formation). In the north-eastern outlet of the basin, finer material (mostly silt) can be found, which was deposited as marginal sediments in the Late Pleistocene (Samra Formation) (Begin, 1974). The unconsolidated sediments are underlain by Cretaceous chalk rocks (Mishash/Abu-Dis Formation, Senonian), which are known as a local aquiclude (Figure 4.4b). The chalk rocks build a syncline below the basin, striking from northeast to southwest. This synclinal form is also effective on the topography of the site, as described above.

The Jordan Rift Valley drains groundwater flowing from adjacent basins (Farber et al., 2004). The source of water flowing through Wadi Auja and the alluvial basin is both, runoff water from the West Bank Mountains flowing through Wadi Auja to the Jordan River (mainly in the rain season in winter and spring) as well as spring water from the seasonally flowing Auja Spring (Schmidt et al., 2014) (Figure 4.4a). The spring contains groundwater from a huge karst aquifer in the West Bank

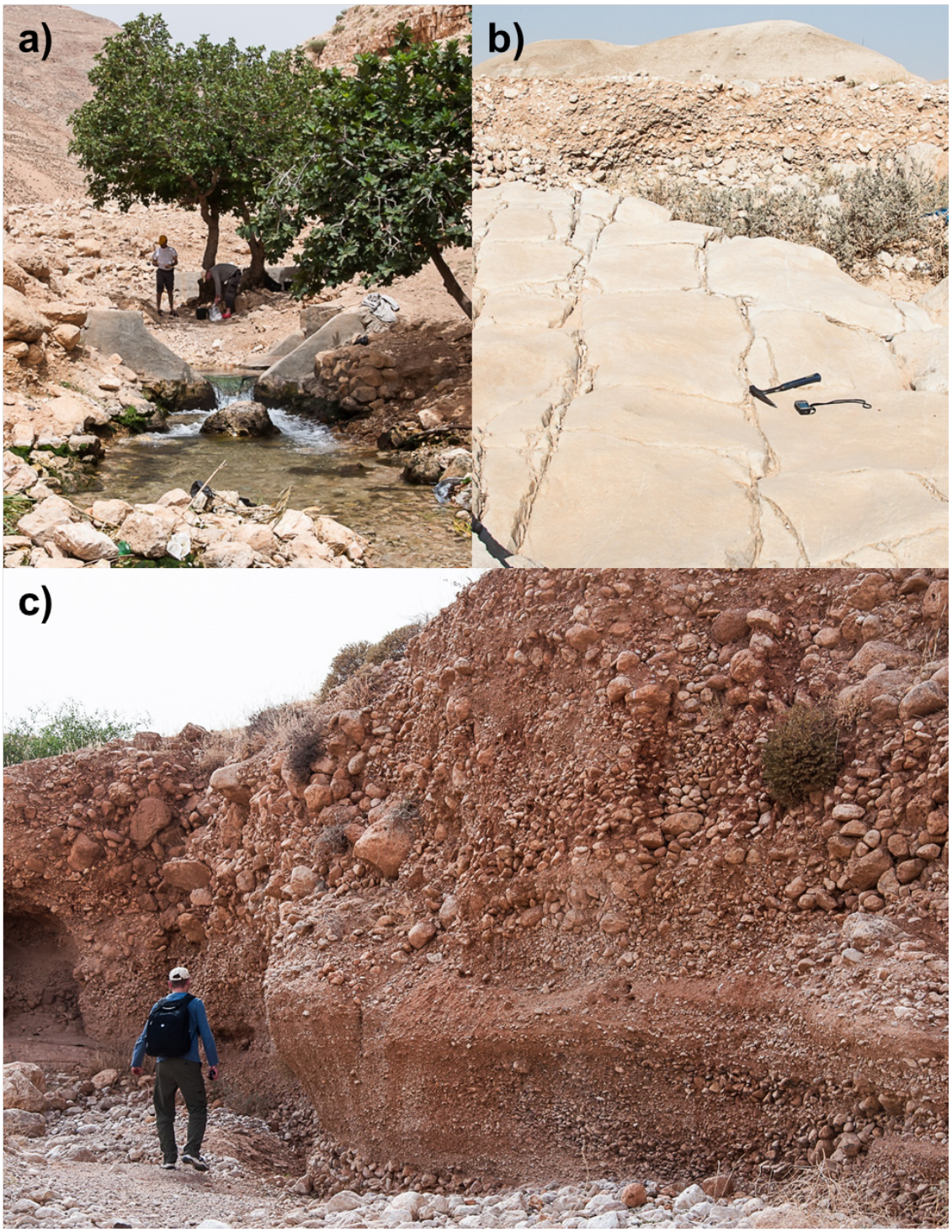

Figure 4.4: Photographs from the study area: (a) Auja spring, with spring tapping structure and gauging station, overhauled during the first phase of the project SMART (see also Schmidt et al., 2014), (b) outcrop of the chalk rock (Mishash/Abu-Dis Formation) near the wadi in the north-eastern outlet of the basin, and (c) outcrop of the alluvial sediments in the basin center close to the location of the geophysical investigation arrays. The picture shows the very heterogeneous sedimentation of the alluvial strata.

Mountains, flowing during winter and spring time with a mean discharge of about $0.3\,m^3\,s^{-1}$ (Schmidt et al., 2014). The runoff water can also occur as flash floods after heavy rainfalls in the mountains.

A weir and a canal, built in the 1960s at the transition between Wadi Auja and the basin, capture parts of the water (runoff and spring water) and lead it to the village Auja, where it is stored in surface ponds for agricultural irrigation. Due to the canals age, lots of water is lost on the 5 km to 6 km distance to the village and as mentioned in Section 4.1 the ponded water suffers from evaporation and contamination through algae growth.

The geometrical situation makes the basin a well reasonable spot for groundwater storage since most parts of the water cannot be captured with the canal.

In November 2011, three exploration boreholes were drilled in the area close to the village (Figure 4.6b) by GMT (Geotechnical & Material Testing Center, Ramallah) in order to characterize the alluvial sediments. Borehole BH1 reached a depth of 5 m and the other two boreholes reached 20 m depth. Figure 4.5 contains the lithological logs of the boreholes. They show that the sediments are mostly composed of an alternation of silty and gravelly sands and sandy silts. Hydraulic conductivity and porosity were calculated by GMT in the laboratory using sediment samples from the boreholes. In addition, other experiments were conducted to measure the hydraulic conductivity of the sediments, such as double-ring infiltrometer experiments, calculations from sieve analyses from soil and sediments samples, and calculations from falling head injection experiments in the boreholes.The values for hydraulic conductivity vary from $1 \cdot 10^{-7}\,m\,s^{-1}$ (in the very shallow subsurface) to about $8 \cdot 10^{-4}\,m\,s^{-1}$. This reflects the heterogeneous characteristics of the alluvial sediments in the basin. The hydraulic conductivity of the shallow subsurface (i.e., < 2 m depth) is very low since it contains fine soil material. From undisturbed soil specimen, a mean porosity of 35% was measured for the alluvial sediments.

4.3 Methodology

In order to use the alluvial basin for subsurface storage, both the hydraulic parameters of the involved sediments as well as the thickness and geometry of the alluvial basin fill material are important parameters that have to be known. To investigate the thickness and the geometry of the alluvial sediments, we used geophysical methods in this study. Refraction seismics is in this case a well suitable method to delineate the basement rock, i.e. the chalk rock. The contrast in seismic velocities between the rock and the unconsolidated sediments is expected to be large and therefore, well to be found. The other method of investigation is electrical resistivity tomography. Also the electrical conductivity is expected to be different for either sediment. However, heterogeneities within the unconsolidated sediments can be detected using ERT.

In addition, the information from the investigation boreholes and sediments samples presented above are used to support the geophysical results.

In order to determine the hydraulic parameters of the alluvial sediments, time-lapse ERT measurements of controlled infiltration experiments were conducted. Also here,

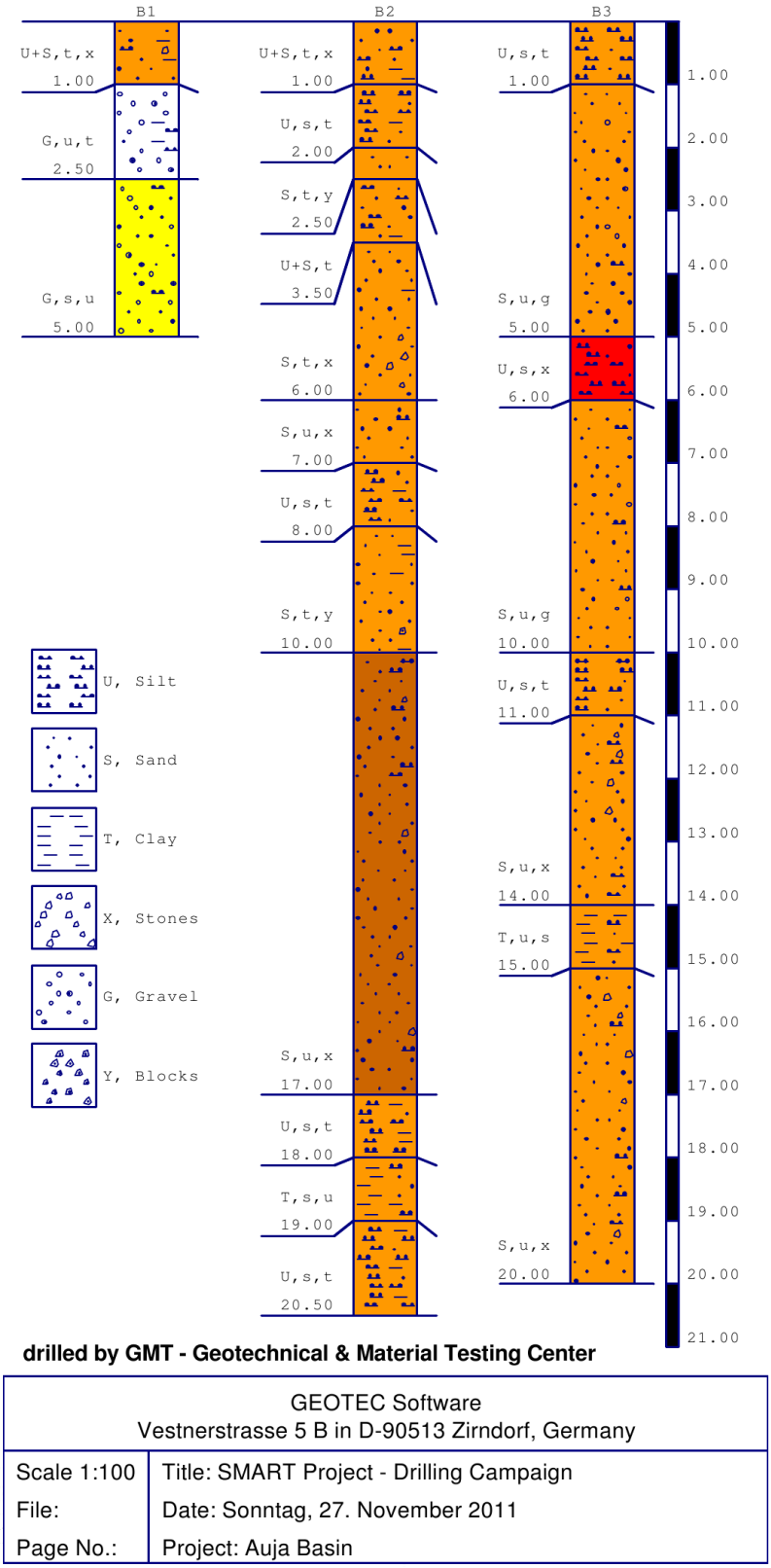

Figure 4.5: Lithological log of the three investigation boreholes drilled at the outlet of the basin. Their location can be found in Figure 4.6b.

the geophysical results are supported by classical hydrogeological measurements, such as double-ring infiltrations and core sample analyses.

4.3.1 Refraction Seismics

The refraction seismic field survey was conducted by the Geophysical Institute of Israel (GII), Lod, in October and November 2010. Six arrays were measured in the northern central part of the Auja basin (Figure 4.6a). The measurements were performed using 48 geophones with a distance of 10 m between them for four arrays (AR1, AR2, AR4, and AR5), 5 m distance for array AR3 and 40 geophones with 10 m separation for array AR6; the entire length of all arrays sums up to about 2.5 km. The seismic source was a 50 kg heavy weight, which fell off a defined height of 1 m above the surface. For each array, the source was placed on eight to nine positions along the line of geophones, starting and ending with an offset of 50 m from the first and the last geophone, respectively. The seismic signal, detected by the 10 Hz geophones, was recorded using SUMMIT remote units with a sampling rate of 0.5 ms and a recording interval of 500 ms.

Afterwards, the seismic measurements were processed and inverted using the software package ReflexW 5.6 (Sandmeier Scientific Software, Germany; *www.sandmeier-geo.de*). At first, a bandpass-frequency-filter was applied to the data. Then the first arrivals were picked and combined in a travel time diagram in order to assign them to the different layers. Finally, a wavefront inversion converts the travel times into depth information. The analyses and evaluation of the seismic data was conducted by Piel (2011) in the framework of his Bachelor Thesis.

4.3.2 Electrical Resistivity Tomography

4.3.2.1 ERT Measurements of Subsurface Structure

Electrical resistivity tomography (ERT) measurements were carried out along two arrays within the basin in November 2010 and two arrays in the outlet at the north-eastern border of the basin in March 2012 (Figure 4.6). The measurements were conducted using an IRIS Syscal Switch Pro 96 resistivity meter. The first array in the basin center was the same like array AR1 of the seismic survey, but extended to the eastern direction. Altogether for the first long array, 160 electrodes were used, with a distance of 5 m between them. The profile was measured as two arrays with 96 electrodes each, with an overlap of two-thirds (known as ”roll-along”) in order to combine the profiles in the later inversion. Measurements were done with Wenner and skip-3 (number of skipped electrodes within one dipole) dipole-dipole configurations. The second array was the same like array AR4 of the seismic survey. 96 electrodes with 5 m separation were used as well as Wenner and skip-5 dipole-dipole configurations. For the two arrays in the outlet area (Figure 4.6b), 96 electrodes were used for each array with 2 m separation for profile AM1 and 2.5 m separation for profile AM2. Measurements were collected as skip-4 dipole-dipole for profile AM1 and skip-3 dipole-dipole for profile AM2.

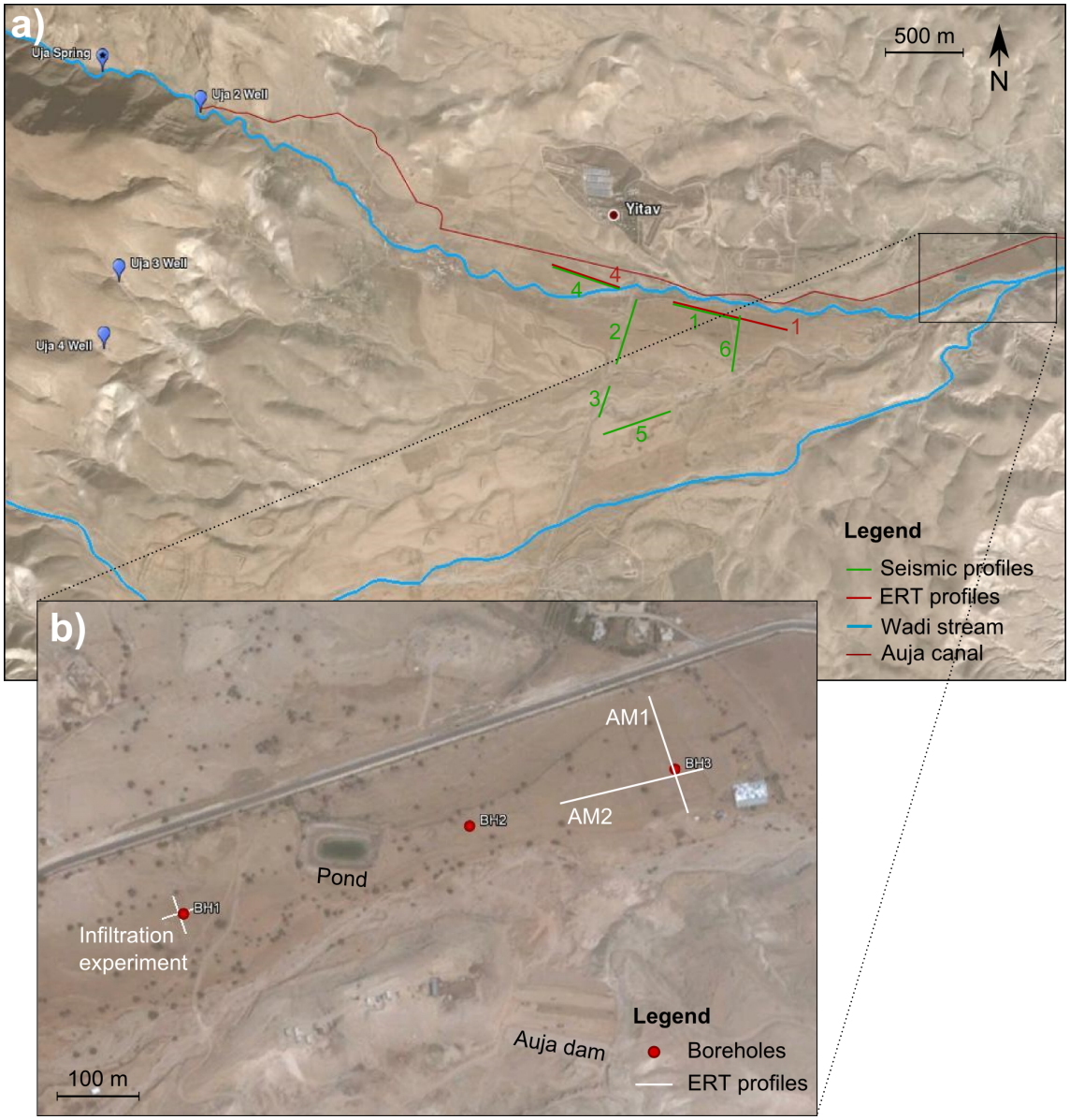

Figure 4.6: (a) Location map of the six refraction seismic arrays (AR1 to AR6) and the two ERT arrays (AR1 and AR4). (b) Location map of the three exploration boreholes, the ERT arrays AM1 and AM2, and the ERT monitored infiltration experiment (picture source: Google Earth).

For the dipole-dipole configurations, the measurements were conducted as normal and reciprocal, i.e., interchanging current and potential electrode pairs in order to provide measurement errors for the dataset. Resistance data were collected in the time domain, using a square-wave current injection with 50% duty cycle and a pulse length of 2 s. 800 mV was set as criterion for the potential readings. The stacking (repetition of readings) was set to a minimum of three and a maximum of six, with the requirement of reaching a quality factor of less than 5%.

4.3.2.2 ERT Monitoring of Water Infiltration

For the infiltration experiment in March 2011, a small, quadratic pond with 3 m length in lateral directions and a depth of 0.5 m was prepared in the north-eastern outlet of the basin (Figure 4.12), close to the village, where the Wadi Auja enters the Jordan Valley (Figure 4.6b). Twice a volume of 7 m^3 of water was infiltrated through the basin into the subsurface (Table 4.1).

Time-lapse electrical imaging was conducted over a one week time period to monitor the changes in electrical resistivity, caused by changes in water saturation due to the infiltration of water. Therefore, ERT measurements were performed in two perpendicular arrays, having the infiltration basin in the center of the arrays. For each array, 48 electrodes with 1 m separation were used in a skip-3 dipole-dipole configuration. One dataset in each array was collected as background before the start of infiltration in order to compare the background data with the following changes over time. For quantification of error parameters, also the reciprocal configuration was measured for the background data set. The other specifications of the Syscal instrument were set as described in Section 4.3.2.1. However, here a pulse length of 0.5 s was used in order to save time for the measurements.

Table 4.1: Time steps of infiltration and ERT monitoring in hours after start of infiltration. t_0 represents the background measurement before start of infiltration.

Time step	Time after start of infiltration
t_0	0 h
Infiltration 1 (7 m^3)	0 h
t_1	1.75 h
t_2	4.5 h
t_3	25 h
t_4	49 h
Infiltration 2 (7 m^3)	76 h
t_5	96.5 h
t_6	147 h

In order to calibrate the measured electrical resistivities for water saturation via Archie's law, four undisturbed soil specimen were extracted from the alluvial basin. The samples were measured in the laboratory with the aim to estimate the Archie parameters (geometrical factors and saturation index). Since the samples were metallic cylinders in the first place, the samples had to be relocated to plastic cylinders. The parameters could be used in addition to the results of the infiltration experiment to quantify the volume of infiltrated water within the infiltration basin.

The samples, relocated into a cylindric sample holder, were saturated with water and the electrical resistivity was measured during evaporation of the water. Using the time-varying electrical resistivity and the change in water saturation, Archie parameters were interpreted using Equation 2.3. The laboratory experiments and the evaluation of the measured data was conducted by Reitemeyer (2015) during his Bachelor Thesis.

From the four samples, a mean value of the parameters was calculated and used for the evaluation of the infiltration experiment. The mean values can be found in Table 4.2.

Table 4.2: Mean values of Archie parameters evaluated from the soil samples.

Parameter	Symbol	Value	Unit
Porosity	ϕ	0.27	-
Formation factor	F	5.4	-
Elec. fluid conductivity	σ_w	0.5	S m^{-1}
Surface conductivity	σ_s	0.016	S m^{-1}
Cementation index	m	1.3	-
Saturation index	n	1.8	-

The value of the electrical fluid conductivity (σ_w) was measured at the site for the infiltrated water. However, in the evaluation of the infiltration experiment, surface electrical conductivity was neglected and thus, the simpler approach after Archie was applied.

4.3.2.3 ERT Data Processing and Inversion

Geoelectrical data are affected by noise. Therefore, filtering of the raw data is required prior to inversion. Systematical errors such as bad electrode connections or problems related to power supply led to removal of data. Outliers resulting from too high current strengths (> 1 A) or large geometrical factors ($> 10^4$ m) were also removed from the data set prior to inversion.

A good estimation of the data error ϵ is crucial, in particular to avoid over-fitting the data and thus the creation of artifacts in the ERT images. The resistance error (ΔR) model used here is defined as (e.g., Slater et al., 2000)

$$\Delta R = a + bR, \tag{4.1}$$

with the parameters a and b accounting for absolute and relative resistance error contributions and R being the measured resistance. From the normal and reciprocal discrepancies, the error parameters were defined to a to 0.015 Ω and b to 2%. For the infiltration experiment, the error parameters were set to a to 0.1 Ω and b to 10%.

After processing of the electrical data, they were inverted using the smoothness-constraint inverse modeling tool CRTomo. A full description of the code is given by Kemna (2000) and a brief overview can be found in Section 3.2.2. In the inversion, the data errors ϵ are represented according to the linear model expressed in Equation 4.1.

Resistivity images exhibit a variable spatial resolution (e.g., Ramirez et al., 1995; Alumbaugh and Newman, 2000; Nguyen et al., 2009). A useful indicator for this variation is the cumulative sensitivity $\boldsymbol{s}$ (e.g., Kemna et al., 2002; Nguyen et al., 2009) (see also Section 3.2.2 and therein, Equation 3.10). The sensitivity indicates how

a change in electrical resistivity of a certain model cell affects a transfer resistance measurement. Analogously, the cumulative sensitivity quantifies the change of a complete dataset to a changing model cell.

For the monitoring data of the infiltration experiment, a difference inversion approach was used to focus only on the temporal changes in electrical resistivities, which are correlated with the change of water saturation (e.g., Daily et al., 1992; LaBrecque and Yang, 2000; Kemna et al., 2002). Here, the inversion results are changes with respect to the background data at time t_0. The advantage of this approach is that modeling errors and data errors correlated over time are canceled out to a significant degree and associated imaging artifacts that would occur in a standard inversion are suppressed.

4.4 Basin Geometry Characterization

4.4.1 Refraction Seismics

The results of the seismic survey are presented in Figures 4.7 and 4.8. They clearly show a two-layered system, which reflect the expected contrast of seismic velocities between the two layers; however, the contrast is lower than expected, which is most likely related to the weathered upper part of the chalk. The p-wave velocities of the unconsolidated sediments are in the range of $700\,\mathrm{m\,s^{-1}}$ to $1{,}000\,\mathrm{m\,s^{-1}}$ whereas the p-waves within the chalk rock reach velocities between $1{,}500\,\mathrm{m\,s^{-1}}$ and $1{,}800\,\mathrm{m\,s^{-1}}$.

The thickness of the first layer, which is interpreted as the unconsolidated alluvial deposits, varies along the different arrays between 10 m and 30 m. Small scale structures at the bottom boundary are related to the paleo-relief (i.e., channel structures) of the chalk. Velocity variations within the upper layers are caused by lateral changes in lithology, for instance areas containing finer material (silt or clay lenses) compared to the coarse, clastic sediments (sand and gravel). Additionally, the variations in velocities can also be caused by varying water saturation or a combination of both.

Figure 4.9 shows a three-dimensional illustration of the six seismic arrays on the geological map of the alluvial basin. The image shows that the thickness of the alluvial sediments seems to decrease towards the south of the basin center; in west-east direction, the alluvial sediments exhibit a relatively constant thickness. It is visible from the illustration that the results of the six different arrays are consistent. The intersection of profiles show the same thickness in all profiles.

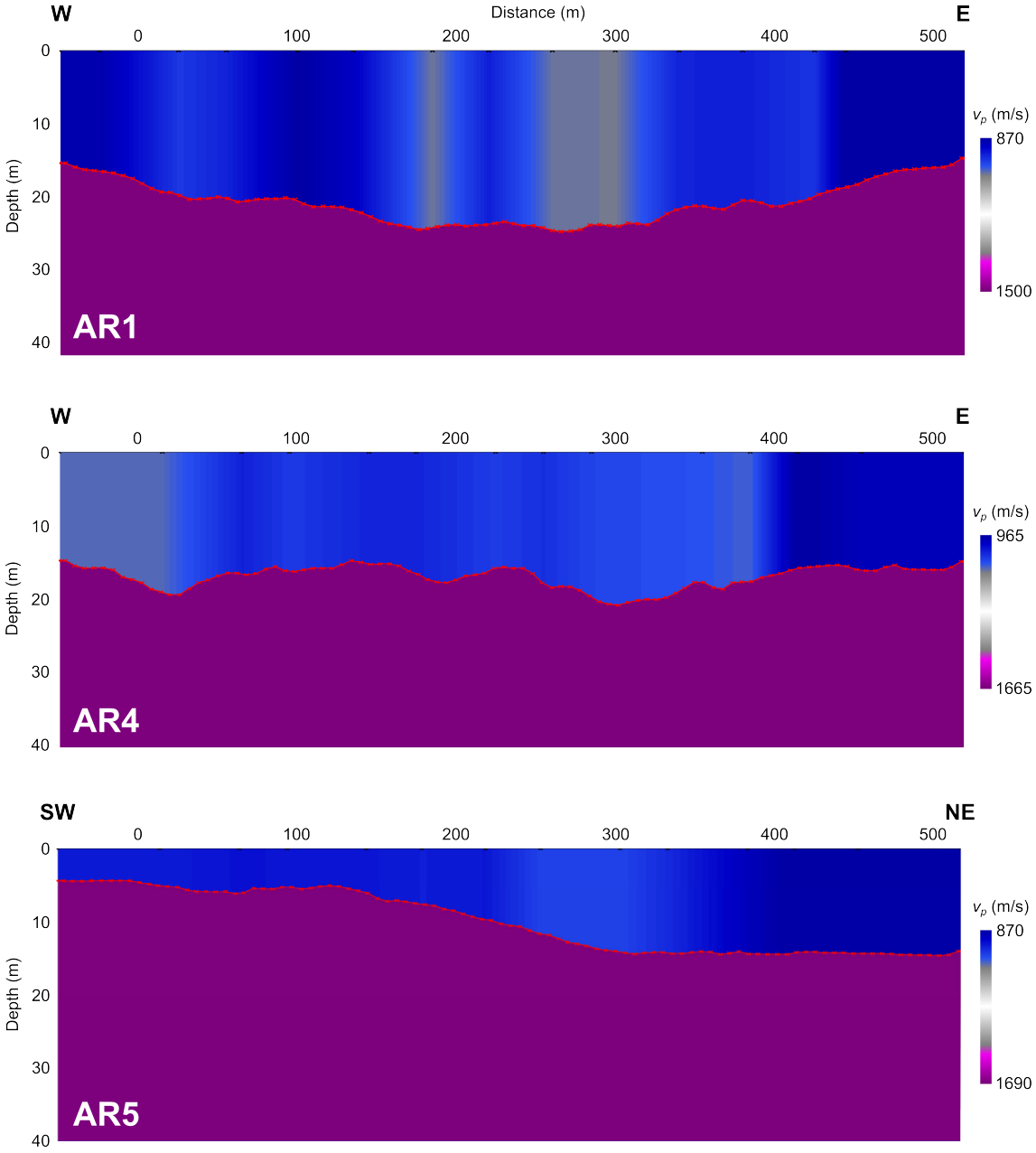

Figure 4.7: Results of the west-east striking refraction seismic arrays AR1, AR4, and AR5. The results reveal that the upper blue (and gray) layer is correlated with the unconsolidated, alluvial sediments and the lower, purple layer with the bedrock. v_p denotes the seismic velocity of the p-wave.

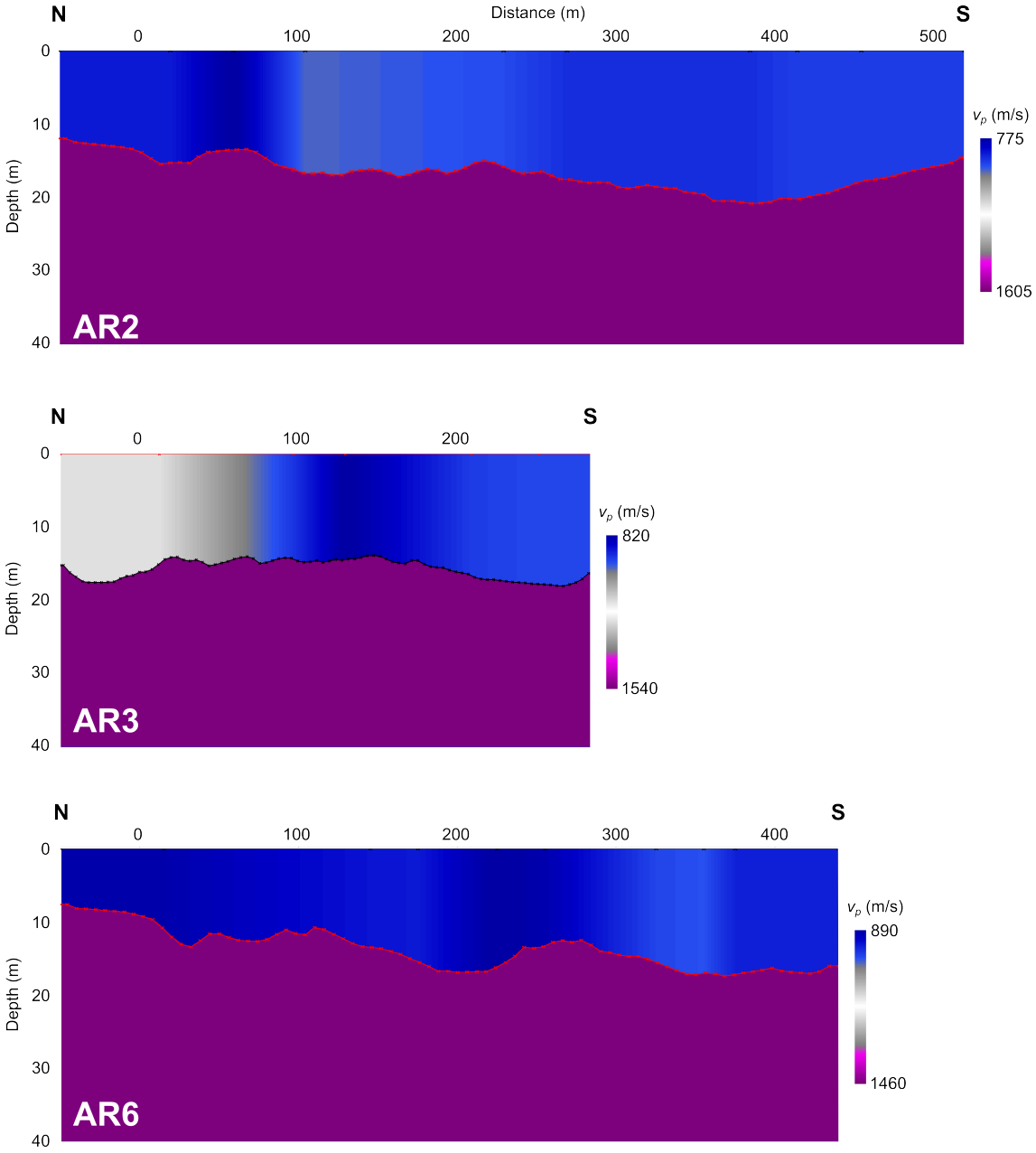

Figure 4.8: Results of the north-south striking refraction seismic arrays AR2, AR3, and AR6. The results reveal that the upper blue (and gray) layer is correlated with the unconsolidated, alluvial sediments and the lower, purple layer with the bedrock. v_p denotes the seismic velocity of the p-wave.

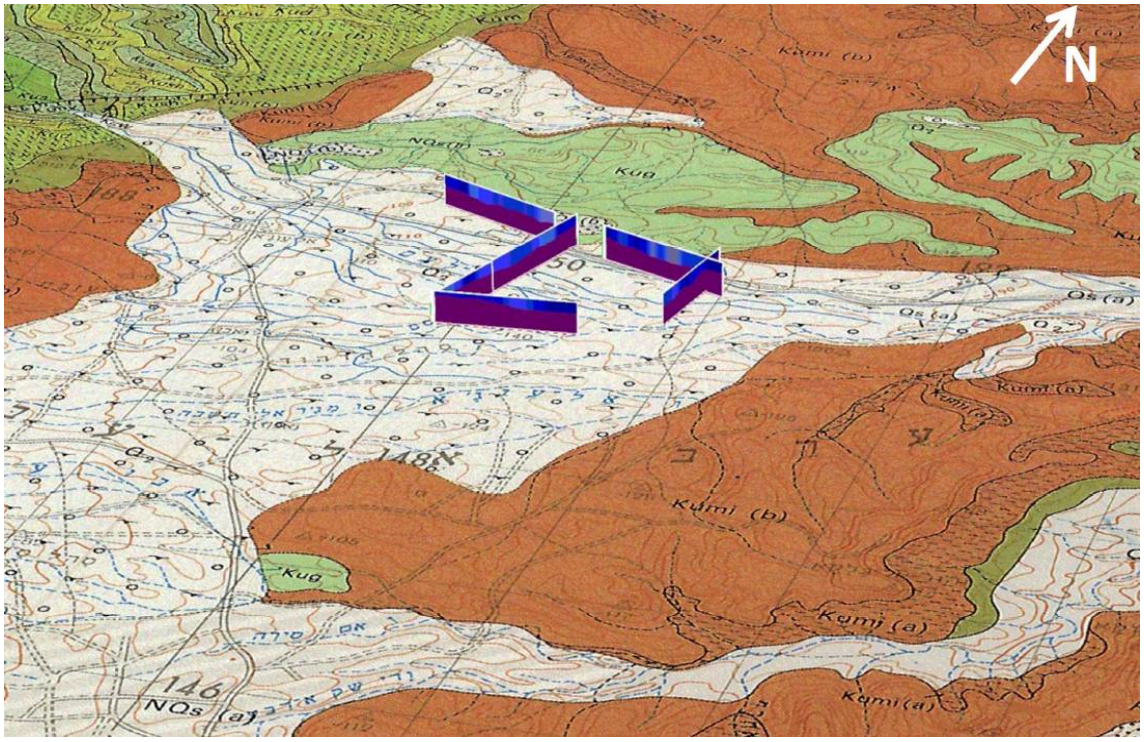

Figure 4.9: Three-dimensional illustration of the six seismic arrays on the geological map.

4.4.2 Electrical Resistivity Tomography

The electrical data of all arrays were processed and inverted as described in Section 4.3.2.3. The results of profile AR1 in the basin center are presented in Figure 4.10. As visible from the electrical resistivity distribution in Figure 4.10a, in a depth from 40 m to 60 m the electrical resistivity changes significantly from values of about 25 Ωm to 70 Ωm to values of up to 700 Ωm. This change can be related to the lithological change of the alluvial sediments to the expected chalk bedrock. However, as seen in the seismic results (Section 4.4.1), the thickness of the clastic sediments seems far less. This is likely caused by decreasing sensitivities of surface ERT with depth (Figure 4.10b). And due to the situation of a high conductive layer overlying a high resistive layer, this can lead to an overestimation of the depth of the resistive layer and therefore, also of the intersection.

During the measurement of profile AR4 battery problems occurred which led to poor data quality. Thus, the data could not be inverted thoroughly and is therefore not shown here.

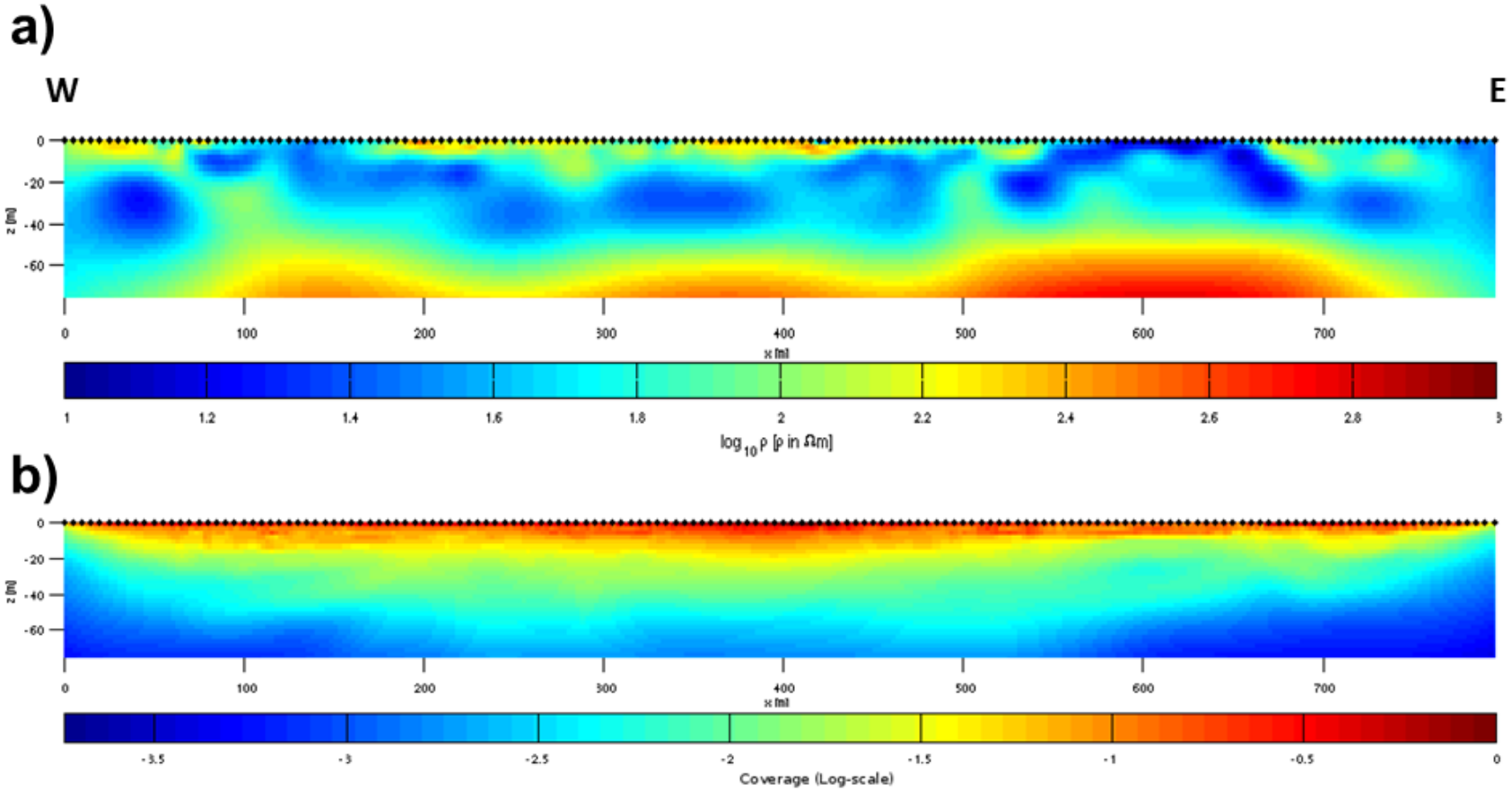

Figure 4.10: (a) Electrical resistivity image of array AR1. (b) Cumulated sensitivity distribution (coverage) of the subsurface for the inversion results of array AR1. Black dots denote the position of the electrodes.

The results of the profiles AM1 and AM2 are shown in Figure 4.11. Both images of electrical resistivity show a high resistive layer in the shallow subsurface (up to about 8 m depth) which is related to the very dry first soil layer. The depth of the bottom resistive layer is indicated between 20 m and 30 m, which is again related to the chalk bedrock. As observed in a nearby drilled well (very close to the location of borehole BH2), the bedrock was reached at 21 m depth. Thus, the ERT images again show a little overestimation of the resistive layer below a conductive layer. However, the overestimation is far less than in profile AR1, probably due to the lower electrode separation (i.e., 5 m for profile AR1 and 2 m and 2.5 m for profiles AM1 and AM2, respectively). Figure 4.11a (resistivity magnitude image) indicates a channel structure which can be related to the paleo-wadi. The high resistive part on the left side of AM1 is most likely related to the chalk rock, which outcrops a few meters south of the profile.

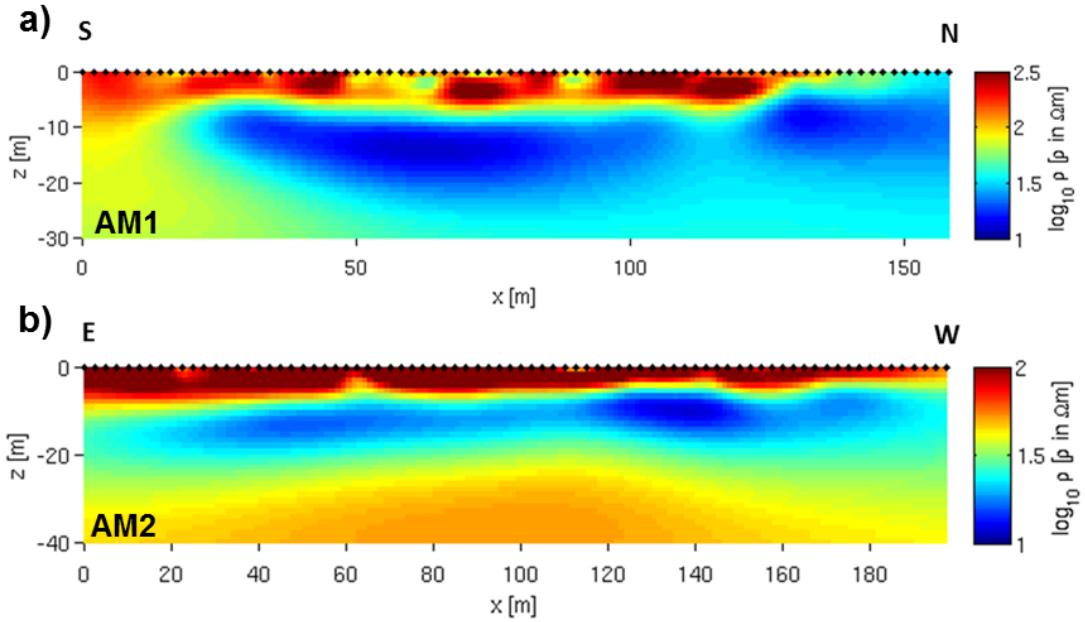

Figure 4.11: Electrical resistivity images of the electrical surveys AM1 (a) and AM2 (b) in the outlet of the basin near the village Auja. Black dots denote the position of the electrodes.

4.4.3 Integrated Interpretation of Geophysical Results

As shown above, the geophysical methods are able to detect the expected two-layered system within the alluvial basin (alluvial sediments overlying the chalk rock).

However, the comparison of the two methods show discrepancies in the estimated thickness of the alluvium, i.e., the electrical images lead to an overestimation of the bedrock depth of up to 100% compared to the seismic images. Due to the lack of ground-truth information at the site (expect the drilling at the outlet of the basin), this interpretation is difficult to validate since also the seismic profiles

cannot be seen as ground-truth data. It is possible that, taking into account the ERT results, the resulting seismic measurements underestimated the thickness of the alluvial sediments.

A planned drilling campaign for observation boreholes within the alluvial basin in the area of the seismic surveys to calibrate the geophysical measurements was unapproved by the Israeli government.

4.5 Hydrogeological Characterization

This section shows and discusses the results of the infiltration experiment. Figure 4.12 shows a photograph of the excavated infiltration pond with the installation of the ERT monitoring system. As described above (see Section 4.3.2.3), the processed ERT data were inverted with the code CRTomo. The inverted electrical resistivities were converted into water saturation using Archie's law (see Equation 2.3 in Section 2.2.1) by using the measured parameters in Table 4.2. The approach assumes that the salinity of the infiltrating water is constant and also temperature effects can be neglected.

Figure 4.12: Excavated pond for the infiltration experiment, filled with water. The depth of the pond was around 0.5 m. The photograph also shows the orange cables of the IRIS Instruments Syscal measurement device for geoelectrical monitoring.

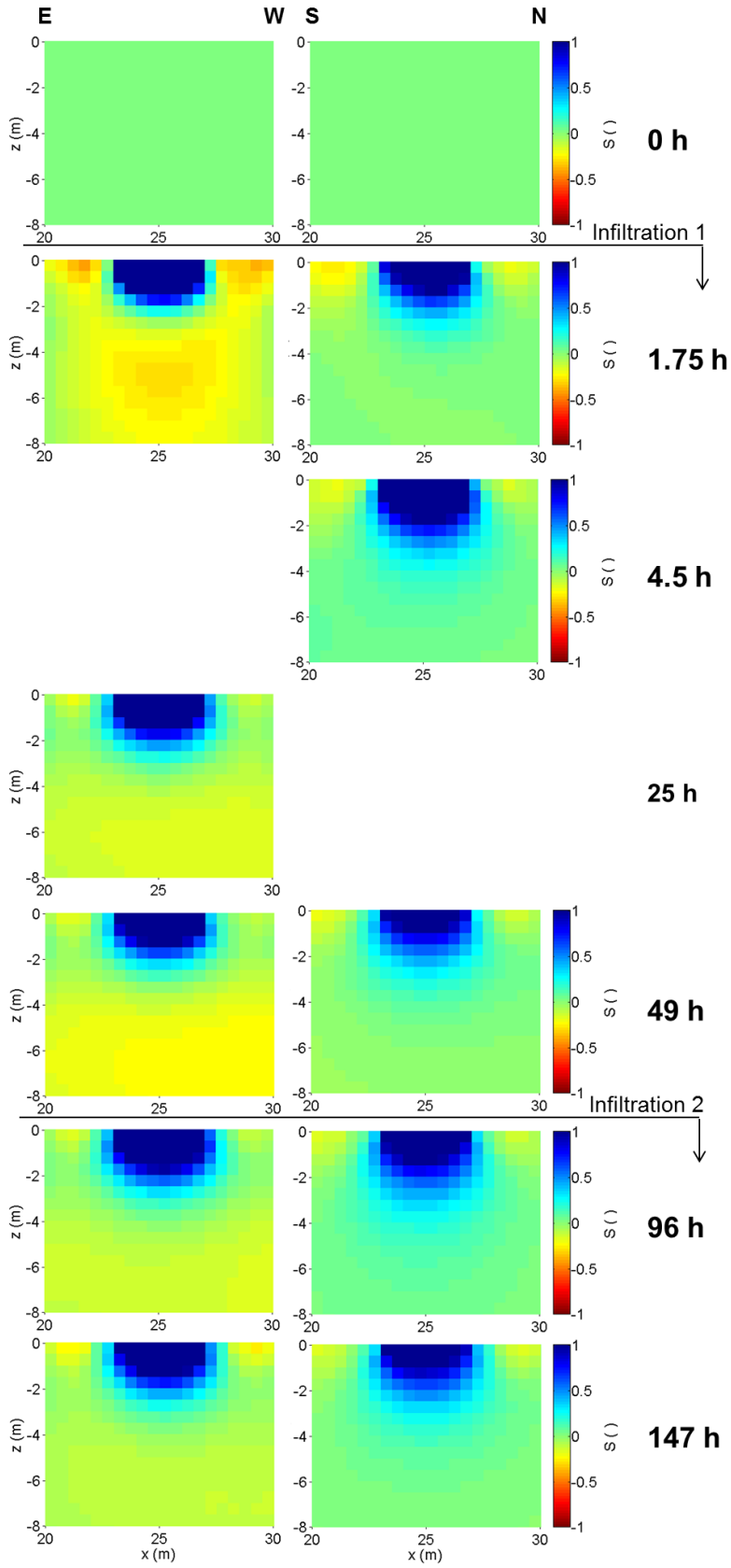

Figure 4.13: Time-lapse ERT monitoring results of the infiltration experiment. The infiltration occurred in the center of the arrays, i.e., between $x = 23.5\,\mathrm{m}$ and $x = 26.5\,\mathrm{m}$. Plotted are the changes in water saturation as stated in Equation 4.2.

Figure 4.13 shows the results of the inverted time-lapse ERT images of the infiltration experiment, where the images show the ratio of the difference of time step t_x and time step t_0 (i.e., the background measurement before start of infiltration) to time step t_0, according to

$$\Delta S(t) = \frac{S(t) - S(t_0)}{S(t_0)}. \tag{4.2}$$

The first image presents the background image at time t_0. Note that the tomograms are only displayed in the area of interest, i.e., between 20 m and 30 m in lateral direction of the ERT profiles; the infiltration pond was located between 23.5 m and 26.5 m in lateral direction. The images clearly show the change in water saturation due to the infiltration of the water through the pond. The main changes are visible up to a depth of about 4 m. The changes below that depth are much smaller. This is due to (a) decreasing coverage of the tomograms and (b) due to the fact that the water electrical conductivity (σ_w) was very high and led to an increased salt concentration for the residual water. This, however, limits the predictions of this experiment to a certain degree. The results are comparable with the results of the surface ERT setup in the synthetic study in Chapter 3. Therein, the plume of the infiltrated water after ERT inversion was smooth compared to the "real" forward model.

Structures close to the surface are related to artifacts in the inversion procedure, mainly seen around the infiltration water plume in the east-west array. This is mainly rooted in changing electrode positions during the acquisition of measurements, since the electrodes could not be left in the study area for the entire experiment duration. The north-south array shows better images due to better data quality, since the cables used for the east-west array for the background measurements caused some trouble during data acquisition and therefore led to higher errors in the data. Due to the same reason, time step t_2 was not usable for the east-west array and time step t_3 for the north-south array. Figure 4.14 shows the background images, plotted

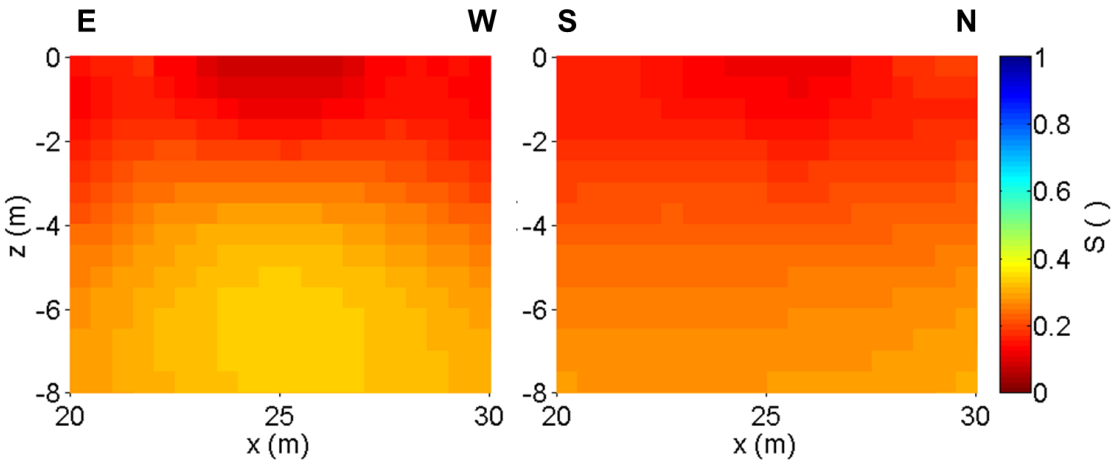

Figure 4.14: Inversion results for the background data at time step t_0 before water infiltration for both ERT arrays. Results are plotted as water saturation.

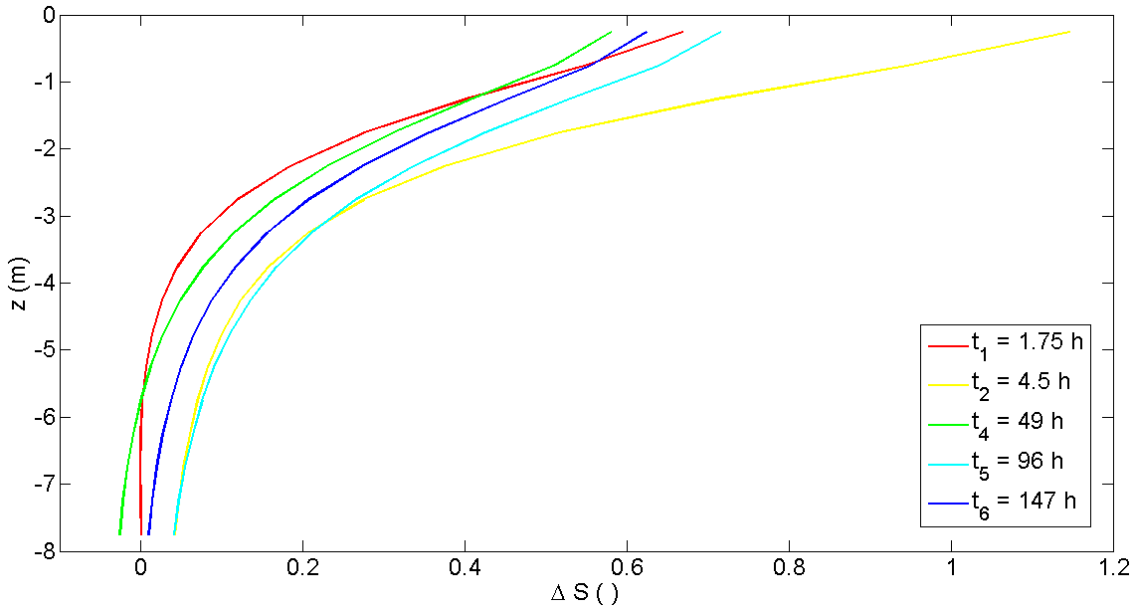

Figure 4.15: Changes of water saturation (see Equation 4.2) with depth for the different time steps for the north-south array.

as water saturation. In the first layer, between 23 m and 27 m in x-direction, the infiltration pond can be seen as an area with very low water saturation. Actually, the 0.5 m deep pond is in this case filled with air. Since the topography of the pond was neglected in the inversion grid, this results in an area with high electrical resistivity and thus, low water saturation.

Figure 4.15 shows the changes in water saturation with depth over time. t_1 was measured during the first filling of the infiltration pond and t_2 was measured after finishing. This explains the significant increase from t_1 to t_2. t_4 was two days after infiltration, and between t_4 and t_5 the second filling of the pond took place, which is also indicated by an increase in water saturation. t_6 is again two days after infiltration. Table 4.1 gives an overview of the time steps. Thus, the water saturation increases with time and depth. However, at lower depth (below about 5 m depth) the water saturation is very low, probably below a value of the residual water saturation at the site. The residual water content was measured during the drilling of boreholes BH2 and BH3 and resulted in a mean value of 7.4%.

Figure 4.16 shows the electrical resistivity image of the area along the west-east array of the infiltration experiment at time t_6. In the image, the position of the infiltration pond (in the center of the image) is clearly visible. The reason for this is due to the high electrical conductivity (and thus high salt concentration) of the infiltrated water. The salt accumulates as residual in the pores of the vadose zone and therefore contributes to low electrical resistivity.

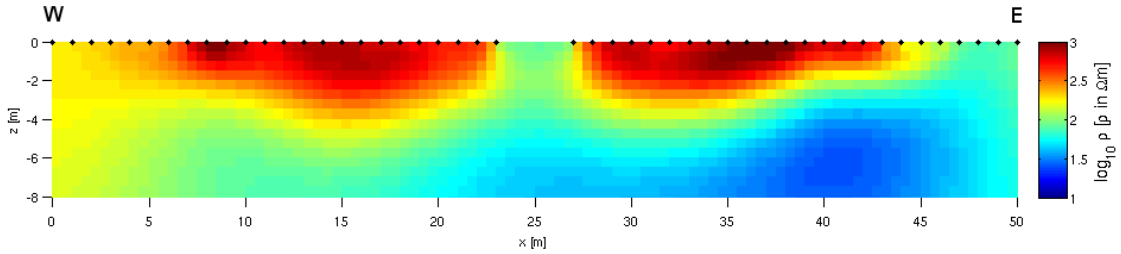

Figure 4.16: Resistivity image of the west-east array along the infiltration experiment. Results show measurements about six days after infiltration (t_6; compare Table 4.1). Black diamonds denote the position of the electrodes.

4.6 Conclusions

In this case study, different geophysical methods were applied to investigate an alluvial basin west of the village Auja in the Lower Jordan River Valley (West Bank) with the aim of the study to assess the suitability of subsurface storage of water within the alluvial basin. Therefore, refraction seismics as well as geoelectrical imaging were carried out along several arrays in the northern and north-eastern parts of the basin.

The results of the basin geometry delineation using the geophysical investigation techniques (RS and ERT) show that the methods are capable in determining vertical and lateral heterogeneities of the geological subsurface structures. This is very useful since it cannot be obtained by typical point information data alone. However, ground truth data (e.g., exploration boreholes) are still needed to calibrate the geophysical results since it was observed that the different geophysical methods (seismics vs. geoelectrics) deliver discrepancies in their results. The ERT images likely overestimated the thickness of the alluvial sediments.

The results of the seismic surveys in the northern, central part of the basin reveal a thickness of the alluvial sediments of up to 30 m with some variations due to paleo-relief structures of the bedrock boundary. Towards the north-eastern direction of the basin, where its outlet is located, the thickness decreases to about 20 m and the paleo-relief shows a channel structure parallel to the recent Wadi Auja.

In addition to the static geophysical measurements to delineate the geological geometry of the basin, an infiltration experiment was carried out in the alluvial sediments to investigate the infiltration behavior and to characterize hydraulic characteristics of the sediments. The experiment was monitored using time-lapse electrical imaging, and supplementary hydrogeological investigations were applied to calibrate the geophysical results.

The results of the study suggest a geometrical situation and hydraulic characteristics of the alluvial basin that make it suitable for subsurface water storage; especially the northern part of the basin, along the recent stream of Wadi Auja, exhibits a constant thickness of the clastic sediments in the range of 20 m to 30 m. However, the heterogeneous hydraulic characteristics of the alluvial sediments are not ideal, but feasible. Further investigations are still needed, such as investigation boreholes

in the basin center to calibrate the RS and ERT results as well as numerical modeling of artificial recharge scenarios.

4.7 Perspectives

This study had the aim of assessing the suitability of subsurface water storage in the working area using hydrogeophysical investigation techniques. The conceptualization and implementation of MAR at the basin was not part of this project. Although this research is a case study, the work can be used in all fields of investigation for MAR and can be taken as a recipe for future studies with the aim of using hydrogeophysical techniques for MAR.

Thus, the study shows that the geophysical methods in addition with selected geological (i.e., boreholes) and hydrogeological (i.e., water and soil samples) point information, thus called hydrogeophysical methods, can be a useful tool for investigations when planning and implementing sites for managed aquifer recharge.

Geophysical methods still reveal more potential in the context of MAR:

- (Spectral) induced polarization ((S)IP): The effect of induced polarization, occurring at the grain-fluid interface after switching on/off the electrical current, contains valuable information about capacitive and resistive characteristics of the subsurface material and can be related to hydraulic properties of the soil (detailed reviews can be found, e.g., in Sumner, 1976; Slater and Lesmes, 2002; Kemna et al., 2004; Binley and Kemna, 2005; Slater, 2007; Revil et al., 2012). Thus, the method can be useful in identifying and monitoring for instance clogging effects.
- Ground-penetrating radar (GPR): GPR can be used for shallow subsurface characterization; applied for instance in boreholes (cross-hole) it can be directly related to water content, e.g., see Chapter 5.
- ERT: Time-lapse data can even be used to identify heterogeneities that cannot be obtained by static measurements alone (temporal-based zonation approach, see Chapter 5).
- Cross-borehole ERT: As shown in the previous synthetic study (Chapter 3), the application of time-lapse ERT between boreholes can increase the resolution and delineation of imaging heterogeneous structures in the subsurface considerably. On the other hand, this application needs installation of boreholes which also increases the study costs and produces an intervention with the flowing system.

As for the Auja basin itself, parallel to the second project phase of SMART (2010 to 2013), the Palestinian Ministry of Agriculture built a small scale dam in the northeastern area of the basin (indicated in Figure 4.6) to capture the runoff water from Wadi Auja for agricultural irrigation with a capacity of 0.5 million cubic meters (MCM) per year (Palestinian Water Authority, 2012). The reservoir also leads to artificial recharge into the subsurface below and downstream of the reservoir.

Acknowledgements

This work was financed by the German Federal Ministry of Education and Research (BMBF) under project number 02WM1081. The author would like to thank Martin Sauter for the fruitful collaboration in this project as well as Sebastian Schmidt, Fabian Ries and René Piel for their help with coordination and in the field. Special thanks to Amer Marei for his great help with coordination and communication with the people from the village Auja and all the help in the field; and to his students Kayan, Subhi and Mahmoud for their help in the field. Further thanks go to Jannik Fassmer and Lukas Reitemeyer for their laboratory work.

Chapter 5

Time-lapse Electrical Imaging of Soil Aquifer Treatment

Based on the publication in Vadose Zone Journal:

Klaus Haaken, Alex Furman, Noam Weisbrod, and Andreas Kemna 2016. Time-lapse electrical imaging of water infiltration in the context of soil aquifer treatment. *Vadose Zone Journal* 15(11), doi:10.2136/vzj2016.04.0028.

5.1 Introduction

Managed aquifer recharge (MAR) is a sustainable technology in modern water resources management (Dillon, 2005). In soil aquifer treatment (SAT), a subarea of MAR, reclaimed wastewater is infiltrated through recharge basins into the subsurface for further purification and to recharge the aquifer. The unsaturated zone functions here as supplementary treatment to filter out organic and inorganic compounds from the effluents. This natural system can also improve the removal of human pathogens, which are a main concern for public health. Moreover, the natural environment increases the cycle time of biodegradation and thereby allows more time for biodegradation of contaminants and sorption of metals (Dillon et al., 2006). The method of SAT becomes increasingly important for regions of water scarcity. The recovered water can be used for instance for agricultural and recreational irrigation. Studies on SAT are spread over the literature. Overviews on SAT (and MAR in general) are given, e.g., by Bouwer (2002), Dillon (2005), Dillon et al. (2006), and Browne et al. (2008).

SAT operation usually involves few days of flooding large basins followed by a few days of drying period. These basins are usually located on natural sandy profiles, which allow the natural processes of purification and fast infiltration rates (Browne et al., 2008). From a physical point of view, SAT is a unique situation of cyclic infiltration under ponding conditions and the unsaturated flow is characterized by very high water fluxes. However, due to increasing amounts of wastewater the available surface areas of infiltration ponds being used for treatment are approaching their limits. This requires consideration of methods to increase infiltration capacity at the existing ponds. Simply continuous flooding of the pond with a constant head of water would lead to increased bioaccumulation and clogging of the surface and shallow subsurface and is therefore not suitable. For increase and control of infiltration, a real-time evaluation of the vadose zone state is required.

The method of electrical resistivity tomography (ERT) nowadays is widely used in hydrogeological investigations (e.g., Binley and Kemna, 2005; Revil et al., 2012; Binley et al., 2015). With the advantages of this spatially extensive, non- to minimally-invasive method, it is possible to characterize the subsurface with high spatial resolution. Moreover, repeated measurements during the course of infiltration events provide a tool for monitoring the vadose zone (e.g., Vereecken et al., 2006). Time-lapse ERT can detect the movement of water in the vadose zone (e.g., Daily et al., 1992; Zhou et al., 2001; Deiana et al., 2007; Looms et al., 2008b). These images can be used as a proxy to identify water infiltration from which flow model parameters can be inferred (e.g., Binley et al., 2002b; Deiana et al., 2008; Looms et al., 2008a; Moreno et al., 2015). Time-lapse ERT has also been used to monitor the spatiotemporal evolution of salt plumes (e.g., Slater et al., 2000; Kemna et al., 2002; Singha and Gorelick, 2005), or variations in salinity in general (e.g., Hayley et al., 2009; Moreno et al., 2015), from which information on flow and solute transport parameters can be inferred (e.g., Vanderborght et al., 2005; Koestel et al., 2009a,b; Müller et al., 2010; Moreno et al., 2015). To date, most studies on ERT monitoring of infiltration experiments are mostly limited to small-scale experiments (e.g., Deiana et al., 2007; Looms et al., 2008b).

Only few studies have investigated the infiltration process of SAT using geophysical methods. Parsekian et al. (2014) applied geoelectrical imaging of the subsurface below an aquifer recharge and recovery site alongside hydrochemical measurements to identify preferential flow paths based on ERT-derived hydrofacies without time-lapse data. Mawer et al. (2013) conducted a synthetic study whereby vertical electrical conductivity profiles and secondary hydrologic data beneath an MAR pond were used to estimate saturated hydraulic conductivity and retention parameters of a homogeneous soil. With their methodology, the logarithm of the hydraulic conductivity could be estimated within 5% accuracy. Additionally, they developed a method to estimate recharge rates and surface clogging. While promising, their synthetic method is limited to homogeneous soils.

MAR sites in general and SAT in particular are limited by land availability and their operation needs to be optimized to allow for more efficient recharge of water. To do that, a better understanding of the flow processes, both in the shallow and deep vadose zone, is needed, which can be obtained from geophysical imaging results. Particularly, geophysical methods allow real-time monitoring of the vadose zone. The ability to determine the real-time state of the vadose zone is essential for hydraulic optimization of SAT infiltration processes.

Our study uses time-lapse ERT to measure the electrical response of the vadose zone exposed to high water fluxes during cyclic water infiltration. It aims at experimentally investigating the ability of (cost-effective) surface ERT measurements to acquire high-resolution (up to 10 m deep and a lateral coverage of several tens of meters, with hourly resolution) images of the vadose zone under very high fluxes.

Using temporally dense ERT measurements, it is possible to track water fluxes in the vadose zone and thereby infer hydraulic information. This leads us to propose a new approach of aquifer zonation using the spatial information on the dynamic behavior of the electrical conductivity during infiltration. The proposed methodology differs from classical zonation approaches which rely on structural (static) information, for instance from the joint inversion of cross-hole seismic, georadar and ERT data (Doetsch et al., 2010b) or from probabilistic approaches based on conditional probabilities of facies given a resistivity value (Hermans et al., 2015), as it is based on the (dynamic) process response.

5.2 Experimental Methods

5.2.1 Site Description

The Shafdan SAT facility in Israel, one of the largest in the world, is being successfully operated for several decades; the annual amount of effluents recharged into the aquifer beneath the recharge ponds is about 120 million cubic meters (MCM), and about 130 MCM per year are pumped by the surrounding production wells (Icekson-Tal et al., 2012). The Shafdan SAT site is part of the Tel Aviv metropolitan wastewater treatment plant (WWTP), operated by Mekorot, the Israeli national water supply company. Effluents of the WWTP are first treated in the mechanical-biological treatment plant and then recharged into a section of the sandy Israeli

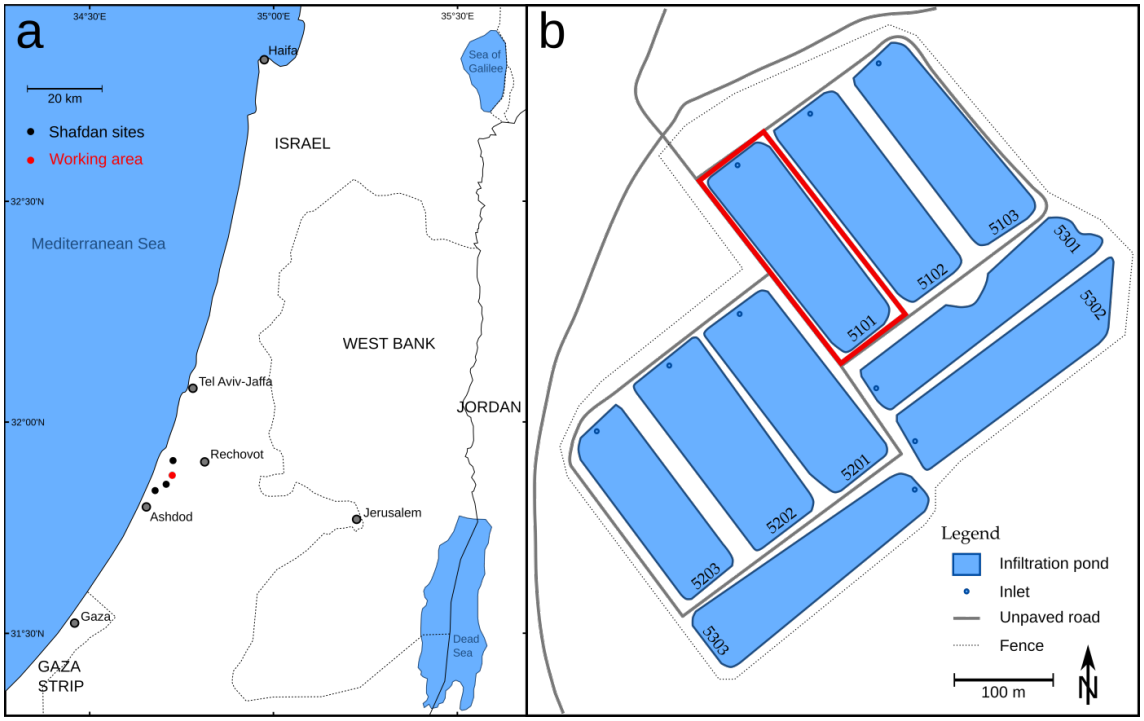

Figure 5.1: (a) Location of the Shafdan site and the working area in Israel. (b) The infiltration ponds at Yavneh 2 with the selected pond 5101 under investigation.

coastal plain aquifer beneath the Yavneh and Soreq spreading basins (Figure 5.1). According to Mekorot report (Icekson-Tal et al., 2012), between 1987 and 2012 about 2,021 MCM of effluents were treated and recharged into the Yavneh basins area (see below) and about 2,188 MCM were reclaimed from the aquifer using production wells surrounding the area (the difference between the numbers is due to natural recharge). The reclaimed water is supplied for unrestricted agricultural irrigation in the southern part of Israel.

The pond under investigation belongs to the Shafdan pond cluster of Yavneh 2, located on the coastal plain area about 20 km south of Tel Aviv, close to the town Yavneh (Figure 5.1a). The cluster consists of nine infiltration ponds, each with a surface area of around 15,000 square meters and a depth of 1 m. Pond Yavneh 2-5101 (Figure 5.1b) was selected for research. The pond is 220 m long and 70 m wide, resulting in an area of about 15,400 square meters. The groundwater table lies at 39 m below ground surface (b.g.s.) and the sediments are mainly composed of sands and silty sands from the Holocene and porous sandstone from the Kurkar formation (Plio-Pleistocene) (Sneh and Rosensaft, 2004). In terms of water infiltration depth, the pond infiltrates over 100 m of reclaimed water per year.

5.2.2 Field Experiment

5.2.2.1 Experimental Setup

The pond was equipped with various types of hydrological and geophysical sensors (Figures 5.2a and 5.2b). Three hydrological stations were installed at different locations of the pond, each with six sensors up to a depth of 3 m. The sensors (time domain transmittance, TDT, by Acclima, Inc., USA connected to a CR1000 data logger, Campbell Scientific, USA) log moisture content, temperature and electrical conductivity.

In total, four direct-push boreholes with an inner diameter of 50 mm were drilled as two pairs with a separation of 3 m for each pair and to a depth of about 20 m (Figure 5.2a). Core samples were analyzed for grain size distribution and porosity using the hydrometer method and dry sieving. The boreholes were equipped with unscreened PVC pipes for zero-offset cross-hole GPR measurements which were undertaken at a mainly dry stage of the pond. Background ERT measurements were conducted prior to the infiltration experiment (see Appendix 5.A).

For the time-lapse ERT monitoring, a total of 288 stainless-steel electrodes were buried at a depth of 0.75 m b.g.s. of the pond (to prevent the electrodes and cables from destruction through the ploughing machine which cultivates the pond surface every few weeks). The electrodes were positioned in three straight lines (see Figure 5.2a for their orientation). Each profile comprises 96 electrodes, separated by 2 m in profile line A1 and 0.5 m in profile lines A2 and B1, respectively.

5.2.2.2 Time-lapse ERT Monitoring

The infiltration experiment, undertaken in May 2014, consisted of four flooding and drying cycles (see also Table 5.1): After the pond was initially dried for about a month, infiltration cycle 1 with one day of flooding and two days of drying was applied (this operation is similar to the common site operation). This was followed by cycle 2 with the same flooding and drying durations as in cycle 1. Following this was cycle 3 with half day of flooding and one day of drying implemented. Cycle 4 consisted of half day of flooding, followed by a long drying period (at least 6 to 7 days). The four cycles add up to a total of 15 days.

Table 5.1: Timing and amount of effluent for the flooding events during the ERT data acquisition in profile A2. Date and time are local time.

Cycle	Start time (dd.mm.yy hh:mm)	End time (dd.mm.yy hh:mm)	Duration (hh:mm)	Effluent amount (m^3)
1	18.05.2014 08:13	18.05.2014 18:52	10:39	7,677
2	21.05.2014 08:29	22.05.2014 08:07	23:38	21,482
3	24.05.2014 09:59	24.05.2014 20:16	10:17	12,906
4	25.05.2014 19:45	26.05.2014 07:59	12:14	10,678

For the ERT monitoring of the infiltration experiment, the permanently installed ERT lines and the IRIS Instruments Syscal Pro 96 Switch resistivity meter were used.

Every hour, a skip-3 dipole-dipole acquisition with 2,580 single resistance readings was applied for the two weeks infiltration procedure, thus comprising of 363 surveys with a total of 936,540 dipole-dipole measurements for profile A2. Acquisition of each frame took about 35 minutes. The infiltration experiment was first applied for profile A2 (see also Table 1) and then repeated for lines B1 and A1, respectively (Figure 2a). We chose to focus here on line A2 as 1) profile A1 (the longer electrode line) delivered lower data quality; and 2) the results for profile B1 (which is perpendicular to profile A2) qualitatively and quantitatively show similar behavior (profiles not shown for brevity) but is somewhat less interesting as it is perpendicular to the

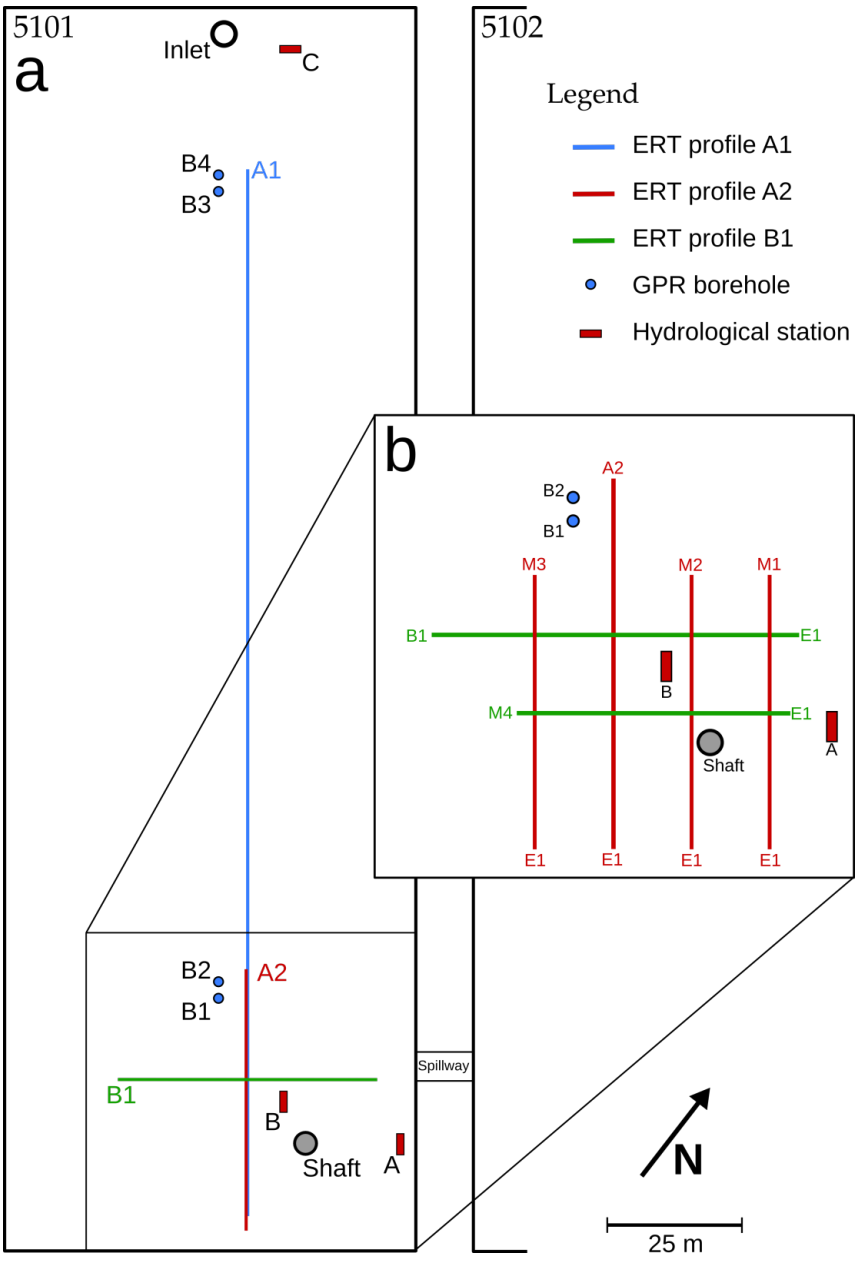

Figure 5.2: (a) Pond Yavneh 2-5101 with geophysical and hydrogeological instruments. (b) Focus on the lower pond edge with positions of the ERT profiles for background measurements (see Appendix 5.A).

general on-surface flow direction.

The following specifications were set to the IRIS system: The stacking (repetition of measurements) was set to a minimum of three and a maximum of six stacks, with the requirement of reaching a quality factor (standard deviation) of less than 5%. Resistance data were collected in the time domain, using a square-wave current injection with 50% duty cycle and a pulse length of 500 ms.

5.2.3 Time-lapse ERT Inversion

5.2.3.1 Data Processing

Geoelectrical data are affected by noise. Therefore, filtering of the raw data is required prior to inversion. Systematical errors such as bad electrode connections or problems related to power supply led to removal of data. Outliers resulting from too high current strengths (> 1 A) or large geometrical factors ($> 10^4$ m) were also removed from the data set prior to inversion.

A good estimation of the data error ϵ is crucial, in particular to avoid over-fitting the data and thus the creation of artifacts in the ERT images. The resistance error (ΔR) model used here is defined as (e.g., Slater et al., 2000)

$$\Delta R = a + bR, \tag{5.1}$$

with the parameters a and b accounting for absolute and relative resistance error contributions and R being the measured resistance. We set a to $0.001\,\Omega$ and b to 5%, which represents a rather conservative approach for the given data.

5.2.3.2 Inverse Modeling

The ERT field data from the infiltration experiments were inverted using the smoothness-constraint inversion code CRTomo by Kemna (2000). Based on a finite-element discretization, the code computes the smoothest possible distribution of electrical conductivity, or its reciprocal, the electrical resistivity, in a 2D image plane explaining the given data set. Here, an objective function $\Psi(\boldsymbol{m})$ is iteratively minimized, which is composed of the measure of data misfit and first-order model roughness, with both terms being balanced by a regularization parameter λ:

$$\Psi(\boldsymbol{m}) = \|\boldsymbol{W}_d[\boldsymbol{d} - \boldsymbol{f}(\boldsymbol{m})]\|^2 + \lambda\|\boldsymbol{W}_m\boldsymbol{m}\|^2, \tag{5.2}$$

where $\boldsymbol{d}$ is the data vector (log resistances), $\boldsymbol{m}$ the model vector (log resistivities of parameter cells), $\boldsymbol{f}(\boldsymbol{m})$ the operator of the forward model, $\boldsymbol{W}_d$ a data weighting matrix, and $\boldsymbol{W}_m$ a matrix evaluating the first-order roughness of $\boldsymbol{m}$. Assuming the data errors are uncorrelated and normally distributed, $\boldsymbol{W}_d$ is a diagonal matrix given by

$$\boldsymbol{W}_d = diag\{\frac{1}{\epsilon_1}, \cdots, \frac{1}{\epsilon_N}\}, \tag{5.3}$$

where ϵ_i is the error estimate (standard deviation) of the i-th datum, $\epsilon_i = {}^{\Delta R_i}/_{R_i}$, and N the number of measurements. At each iteration step of the inversion, a univariate search is performed to find the maximum value of the regularization parameter λ which locally minimizes the data misfit. The iteration is stopped when the RMS error-weighted data misfit,

$$\mathrm{RMS} = \sqrt{\frac{1}{N}\sum_{i=1}^{N}\frac{|d_i - f_i(\boldsymbol{m})|^2}{|\epsilon_i|^2}}, \tag{5.4}$$

reaches a value of one.

In a time-lapse monitoring framework, one is primarily interested in the temporal changes of data and parameters. Therefore, in the "difference inversion" approach of time-lapse ERT (e.g., LaBrecque and Yang, 2000; Kemna et al., 2002), $\boldsymbol{d}$, $\boldsymbol{f}(\boldsymbol{m})$ and $\boldsymbol{m}$ in the objective function (Equation 5.2) are replaced by, respectively, the differences $\boldsymbol{d} - \boldsymbol{d}_0$, $\boldsymbol{f}(\boldsymbol{m}) - \boldsymbol{f}(\boldsymbol{m}_0)$ and $\boldsymbol{m} - \boldsymbol{m}_0$, where $\boldsymbol{m}_0$ is the background model obtained by carrying out a standard inversion of the background data $\boldsymbol{d}_0$ at time t_0. The advantage of this approach is that modeling errors and data errors correlated over different time steps are canceled out to a significant degree and associated imaging artifacts that would occur in a standard inversion are suppressed.

5.3 Results & Discussion

5.3.1 Apparent Conductivity

Figures 5.3a and 5.3b show the ERT monitoring raw data prior to inversion and the volumetric water content (VWC) measured at station B, respectively. Figure 5.3a contains the average values of the apparent electrical conductivity (reciprocal of the apparent electrical resistivity) from each of the 363 data sets as well as the infiltrated volume of effluents as columns (data obtained from Mekorot based on flow metering of the inlet). The apparent electrical conductivities are categorized according to the distance between the two electrode pairs (dipoles) involved in the measurement, representing different "pseudo depths" (while each measurement can be seen as an integral response of the subsurface, measurements with larger dipole separations are more sensitive to greater depths than those with smaller dipole separations). The VWC data (Figure 5.3b) is measured until a depth of 2.9 m. Thus, only the "shallow" ERT data (red lines in Figure 5.3a) correspond to the data from the TDT sensors. The curves of apparent electrical conductivity clearly show four peaks synchronized with the flooding of the pond. From this it follows that the four peaks reflect the breakthrough of the four infiltration events. As the flooding of the pond starts, the overall electrical conductivity increases immediately and after infiltration ceases it decreases quickly, then slowly back to the background value.

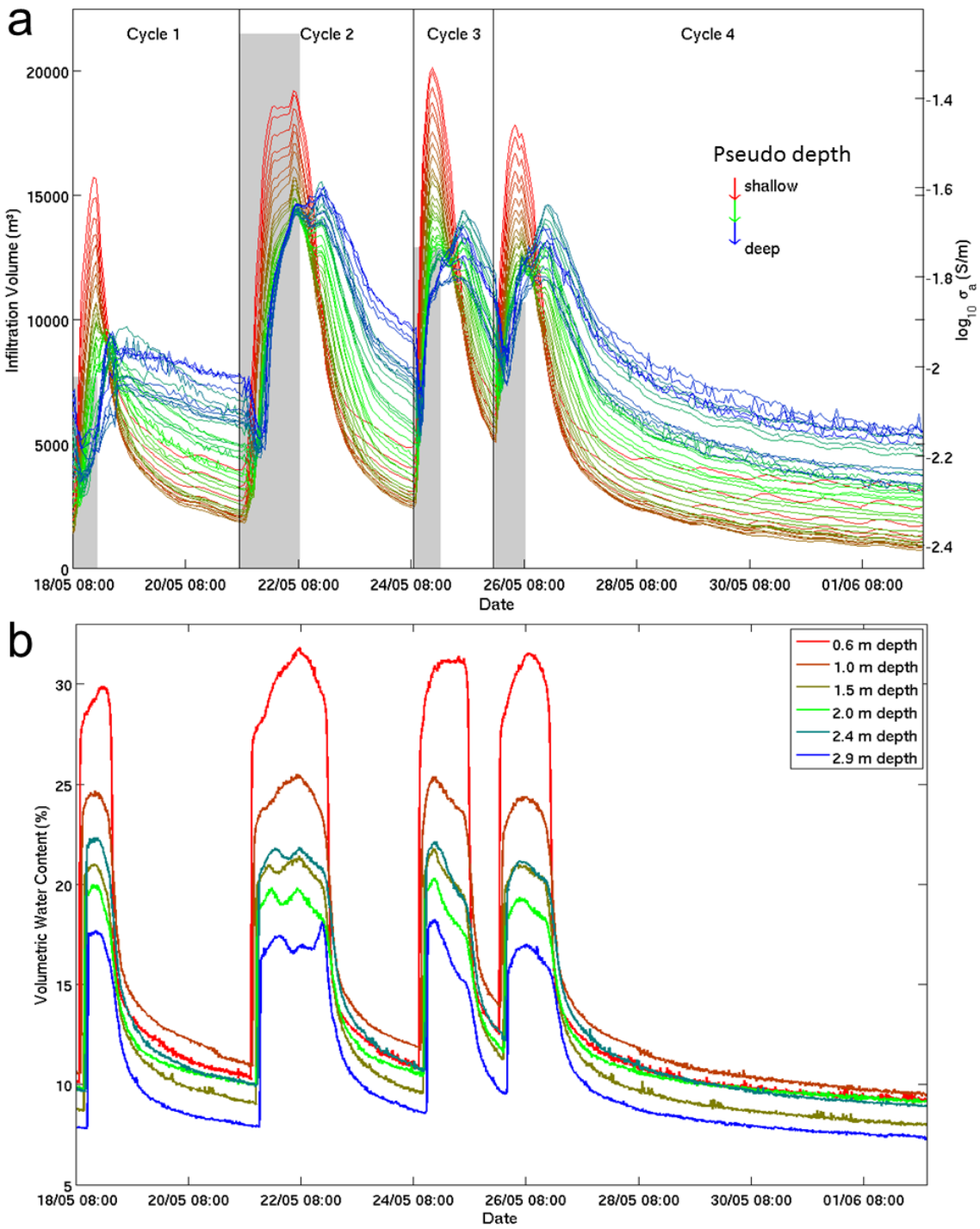

Figure 5.3: (a) Median of apparent electrical conductivity measurements (raw data) for increasing pseudo depth and volume of infiltrated water (grey columns) for the period between May, 18th and June, 2nd 2014 for profile A2. Start time was 8:13 a.m. on May, 18th. (b) Volumetric soil water content data for different depth, measured from the TDT sensors in hydrological station B for the same time period (see also Figure 5.2).

It is clearly visible that the ERT raw data contain valuable information about the system behavior at different depths and cycles. Each of the breakthrough curves (Figure 5.3a) seems to contain two groups of peaks, the first for the "shallow" measurements (red lines) and a second, temporally delayed, for the "deeper" measurements (blue and green lines).

Differences between shallow and deep measurements do not only occur regarding the timing of peaks, but also regarding the way the electrical conductivity increases (or decreases). Shallower measurements show faster increase in electrical conductivity, which is expected. They also increase to higher values. Given the large infiltration (well over 100 m annually) and the stability of the water salinity (Icekson-Tal et al., 2012), and the not so different lithology at depth, this clearly means that the water content at shallower depth reaches higher values, compared to the deeper sandy layers. This is confirmed by the volumetric water content measurements, displayed in Figure 5.3b.

ERT data for the drying period also show differences for the different layers: the electrical conductivity decreases rapidly for the shallow layers, indicating fast drainage. At the same time, the deeper layers show a much milder drop in electrical conductivity – much slower and to a higher final state. Above all, this indicates very low retention in the shallow layers. In the deeper layers, the decreased rate is partially due to the draining from shallower layers, but the elevated final electrical conductivity also indicates higher retention. This is best seen at the right end of Figure 5.3a, and qualitatively supported by the particle size distribution (see Figure 5.9b).

As the flooding of the pond starts and correspondingly the apparent electrical conductivity in the shallow measurements increases (mainly red lines in Figure 5.3a), it first decreases for the deeper measurements (mainly blue lines). We attribute this seemingly counter-intuitive observation to the well-known negative sensitivity of the deeper measurements in shallow regions (e.g., Spitzer, 1998). Only after some delay, i.e., with water further infiltrating downwards into the region of positive sensitivity of the deeper measurements, also these responses become positive.

The curves in Figure 5.3a also show daily variations for the very shallow measurements (red lines; best seen especially at times when the pond is empty, between 27/05 and 02/06), most probably induced by the daily temperature variations which also influence the electrical conductivity (e.g., Hayley et al., 2007). With increasing dipole separation, these daily variations decrease. The deeper measurements also show more pronounced erratic fluctuations in the transient response, indicating that the signal-to-noise ratio decreases with depth.

5.3.2 Conductivity Images

Figure 5.4 presents the difference inversion results from selected time steps for infiltration cycle 4 for ERT profile line A2. The inversion RMS (Equation 5.4) reached a value of one in nearly all inversion runs. The inverted images of electrical conductivity clearly show the change of electrical conductivity over time induced by the change in water content during infiltration. It can be seen that the water front starts propagating from the inlet of the pond (i.e., from the right hand side in the images)

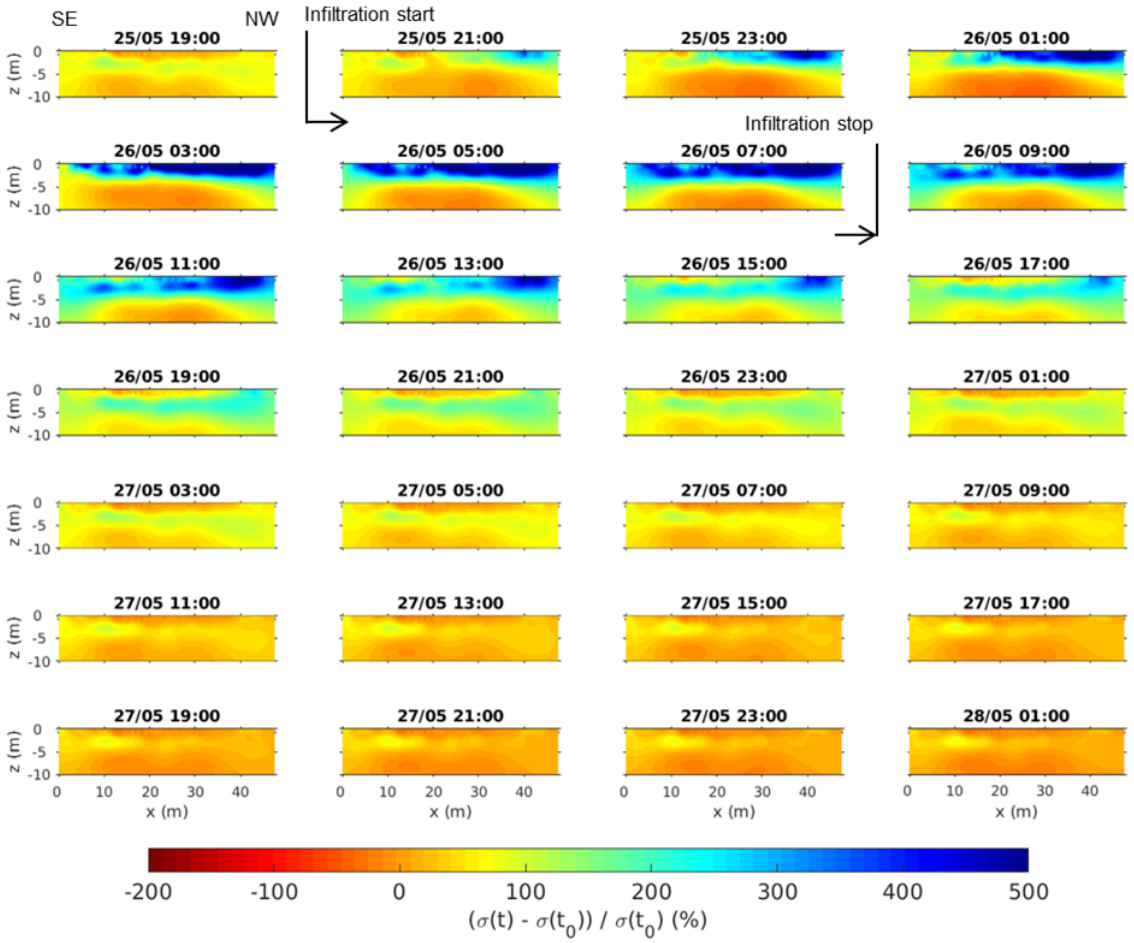

Figure 5.4: Inverted time-lapse ERT images of change in electrical conductivity for infiltration cycle 4 on profile A2, plotted here every two hours. Black diamonds denote the position of the electrodes, electrode E1 is positioned at $x = 0$ m. Pixel size is 0.25 m by 0.25 m.

until covering the entire profile length after a couple of hours. A subsurface layering is clearly visible in the dynamic behavior of the electrical conductivity. First, the conductivity increases in the very shallow part of the pond down to about 2 m depth. The layer between 2 m and 7 m depth, which is supposed to contain coarser material (compare Figure 5.9b), only shows a small increase in conductivity. The layer below these coarse sediments shows a strong increase, but at a later time (about 18 h after start of injection). The inversion results demonstrate the ability of ERT to track the vadose zone state and thus the dynamics of water infiltration even in the case of very high water fluxes.

Figure 5.5 shows the changes in electrical conductivity compared to the changes in volumetric water content from station B. The electrical conductivity values were chosen from the same depth representation as the water content sensors. The graph shows a strong correlation between electrical conductivity and volumetric water content.

Figure 5.6 shows the breakthrough curves of the inverted electrical conductivity for

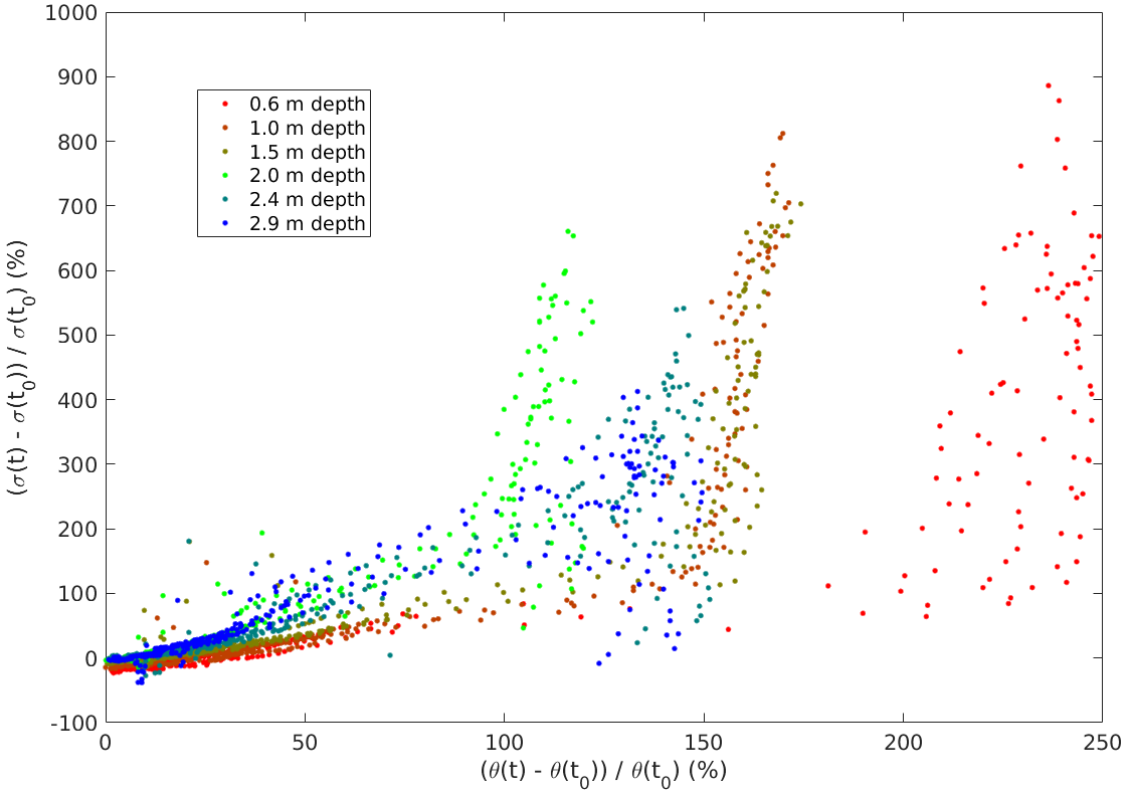

Figure 5.5: Scatter plot showing the inverted relative electrical conductivity against the relative volumetric water content. The pixels from the inverted ERT data were selected from $x = 24\,\text{m}$ (close to the position of the TDT station B) and at the same depth as the TDT sensors.

two selected pixels at different depths (1 m and 8 m depth) in the lateral center of the profile, where the best depth coverage can be found. They show the same general behavior as observed in the apparent conductivity curves (compare Figure 5.3a). Also here, the curve looks noisier at depth.

In Figure 5.7 we compare the same state of the vadose zone for the four infiltration scenarios, i.e., plotted are the images at 12 hours after start of infiltration for each of the four cycles. At this time the entire pond surface is already covered by water for about three hours in all events, which allows comparing the way the initial conditions affect the infiltration and the vadose zone state, as expressed by the electrical conductivity. Since the pond was initially dry before the experiment started and the amount of infiltrated water in the first cycle was small compared to the other cycles, the first and second images in Figure 5.7 show overall lower electrical conductivity than the other two images. This indicates that the vadose zone had contained less water before the breakthrough of the infiltrated water in the second cycle.

5.3.3 Temporal-based Zonation

The continuous measurements at high frequency open a new dimension for the understanding of the subsurface during infiltration. We discuss here a new approach

for subsurface hydraulic zonation based on the temporal behavior of the spatially distributed electrical conductivity. Herein the breakthrough curves for every single pixel of the electrical tomogram are analyzed, with the focus on the "drying" part of the curve. The local transient response upon drying can be expected to capture the local hydraulic properties. Coarse material (i.e., gravel and sand) typically shows a faster desaturation and larger water content changes between saturated and unsaturated conditions than finer material (i.e., silt and clay). Moreover, in general the electrical conductivity of finer material is higher than for coarser sediments (both due to higher water retention and to higher clay content and thus the effect of surface conductivity). However, the locally observed transient response is also a result of the infiltration through the layers above and therefore, strictly speaking, reflects the hydraulic properties down to the considered position. For instance the desaturation of a gravel layer below a fine layer is mainly influenced by the leakage of the fine layer. Nevertheless, abrupt changes of the hydraulic properties at lithological boundaries can be expected to also impact the characteristics of the drying curve. Thus, a discrimination of zones with different hydraulic properties should be possible.

In order to quantify the differences in the transient hydraulic response upon infiltration across the ERT image plane, we fitted an appropriate, simple parametric function to the temporal electrical conductivity changes over the drying period for

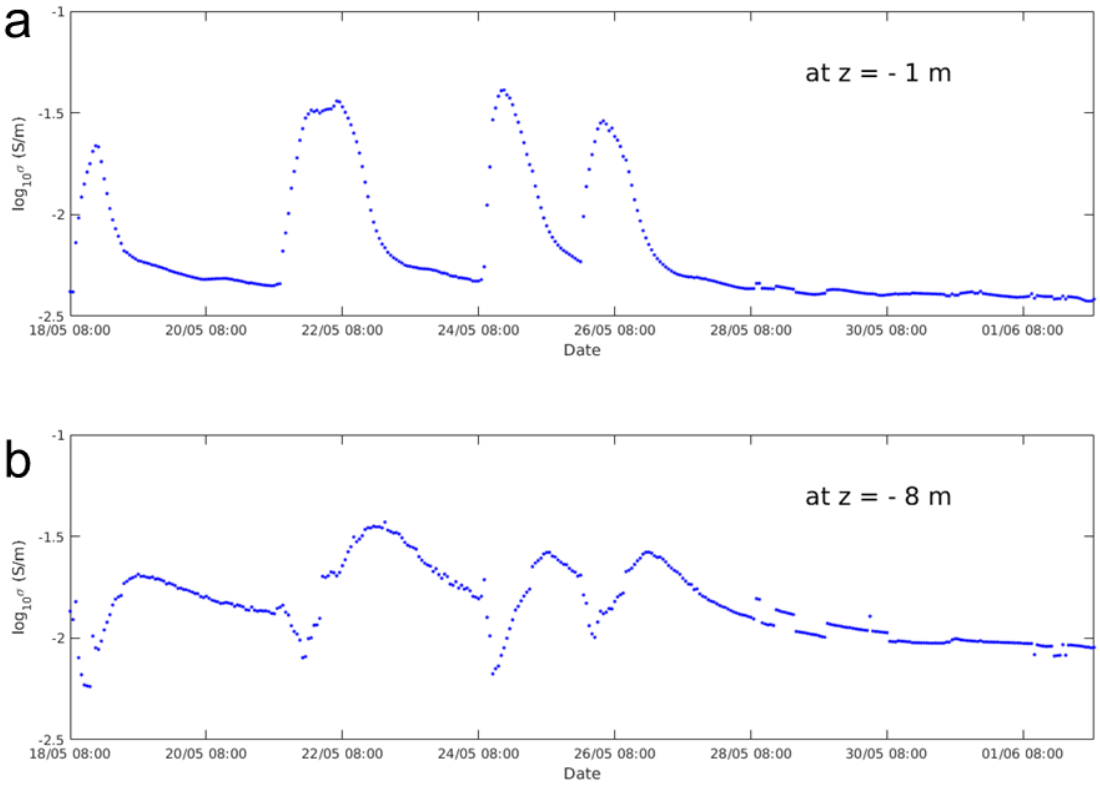

Figure 5.6: Breakthrough curves of inverted electrical conductivity for selected pixels of the ERT tomograms for profile A2 at 24 m in x-direction and at (a) 1 m depth and (b) 8 m depth.

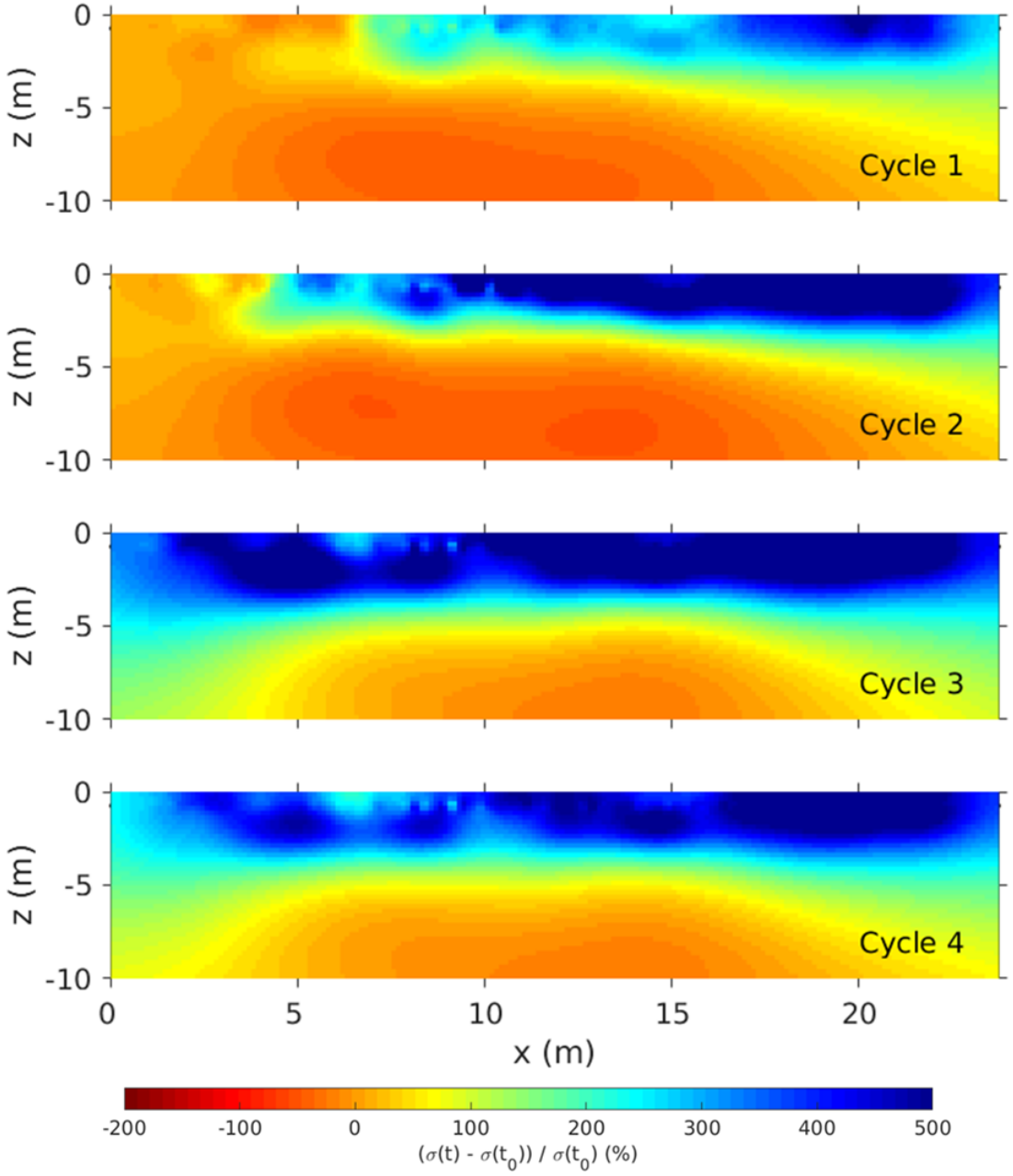

Figure 5.7: Selected images of differences in electrical conductivity of the inverted ERT data at 12 hours after start of flooding, approximately corresponding to peak breakthrough, for each of the four infiltration cycles on profile A2 (see also Table 5.1). Pixel size is 0.25 m by 0.25 m.

each pixel of the image plane. We empirically found that a satisfactory fit can be achieved with an exponential function of the form of logistic regression, adopted as

$$\sigma(t) = \frac{\sigma_{max}}{1 + e^{\frac{t-t_0}{\tau}}} + \sigma_{min}, \tag{5.5}$$

which was fitted to the curves. So, for each pixel from the ERT images, a breakthrough curve was created, from which the variables were determined. We only look

at the drying part of the curves, meaning from the peak of the curves to the minimum value. In Equation 5.5, σ_{max} represents the background electrical conductivity at the maximum of the breakthrough curve (i.e., at highest water saturation), σ_{min} represents the background electrical conductivity for the driest stage of the pond, τ describes the slope of the curve from the peak (σ_{max}) down to the minimum (σ_{min}) and represents a characteristic time of the desaturation process, and t_0 defines the time when the peak breakthrough takes place at the analyzed pixel. Although the parameters cannot be directly associated with more physical parameters, it is clear that σ_{max} and σ_{min} are primarily related to porosity and residual water content, respectively, τ is related to both the hydraulic conductivity and retention, and t_0 is related to the "hydraulic depth" of a given point. For instance, a small value of τ, meaning a steep slope, represents fast drainage and more coarse material whereas a large value of τ, a flat slope, means slow drainage and more fine material. Clearly this simplistic analysis can be better described for shallow points, while in deeper strata τ is also related to water infiltrating from shallower strata.

By fitting the function in Equation 5.5 to every pixel of the time-lapse tomograms, images of the four empirical parameters σ_{min}, σ_{max}, τ, and t_0 are obtained (Figure 5.8). These images reflect spatial variations in the infiltration response as a result of heterogeneities in the hydraulic properties and thus provide an indirect mean for a structural zonation of the subsurface that can be used for example for subsequent joint inversion of both geophysical and hydrological data. The two images of electrical conductivity, representing the upper and lower ends of the pond state with respect to water saturation are in good agreement with the corresponding snapshot images of the ERT monitoring (compare σ_{min} with step '28/05 1:00' in Figure 5.4 or profile A2 in Figure 5.10; compare σ_{max} with step '26/05 9:00' in Figure 5.4). Only for σ_{max}, the electrical conductivities mainly in the left part of the image are lower compared with the snapshot images. Additionally, the tomogram of σ_{max} shows smaller values closer to the corner of the pond which is probably related to reduced infiltration at the corners of the pond. We assume that salt accumulation is not significant in this case due to the annual load of effluent (over 100 m) and a potential evaporation of 1.5 m per year.

The parameter t_0 shows a two-layer system, which was already observed in the two peaks of the breakthrough curves of the apparent electrical conductivities (Figure 5.3a). The increased vertical gradient in t_0, i.e., in the peak breakthrough arrival time, at about 4 m depth indicates a higher hydraulic conductivity in the upper layer. Two main layers with different hydraulic properties are also suggested by the time parameter τ, with lower values in the upper layer (down to 3-4 m depth) indicating higher fluxes and with that lower retention as compared to the deeper region. The deeper region also shows lateral variation in τ, and thus the retention properties (with a decrease in retention from left to right in the image), which corresponds with the overall pattern observed in σ_{max}. We focus here mainly on the vertical heterogeneities of the parameters t_0 and τ, and do not highlight lateral heterogeneities.

Figure 5.9 shows the parameter τ as well as the electrical conductivity (at a mainly dry stage of the pond) versus depth at a lateral position of profile A2 close to the GPR boreholes B1 and B2 (at about 42 m) in comparison with the GPR results and

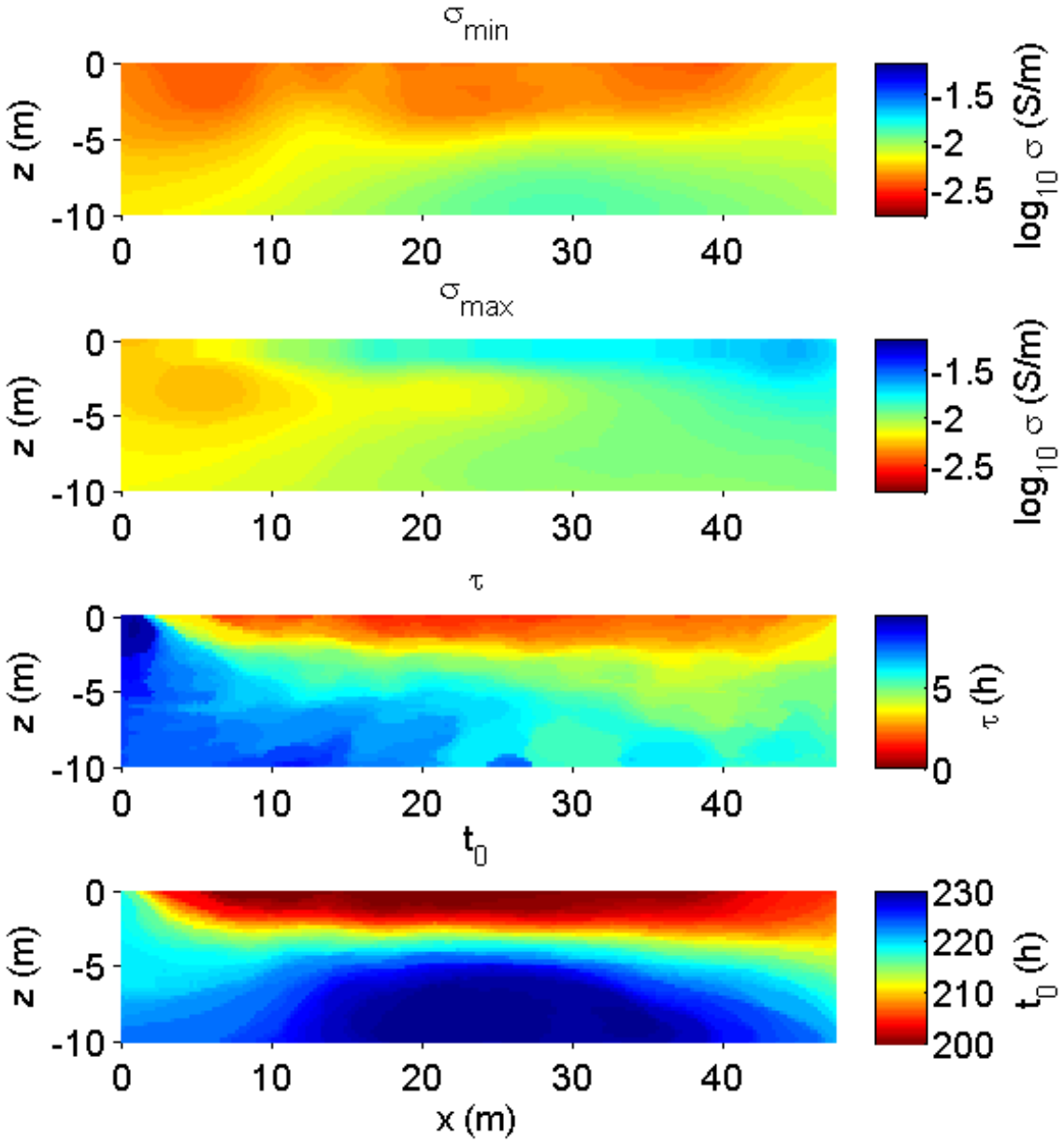

Figure 5.8: Images of the four parameters obtained from fitting Equation 5.5 to the time-lapse ERT results for each pixel for profile A2. A 2D median filter with a window size of 10 by 10 pixels was applied to the images to remove individual outliers in the fitting results. The parameter t_0 is the time (in hours) since start of the infiltration experiment (i.e., May, 18th 8:13 a.m.). Pixel size is 0.25 m by 0.25 m.

the grain size distribution from borehole B1. The layering reflected by the vertical τ variation (Figure 5.9c) agrees very well with the GPR data and the results from the grain size analyses (Figure 5.9a and b). The continuous increase in τ between 2 m and 4 m depth corresponds with a gradual change in GPR velocity. The GPR results show a stronger layering than the grain size distribution due to increasing arrival times (and stronger attenuation) of the radar waves between 3 m and 9 m depth. This is likely related to increasing water content within the uniform sand, which possibly indicates a perching layer above the layer of clayey sand below 9 m depth. This is

also very well captured by an abrupt increase just below 8 m depth in the vertical τ distribution. This layer boundary is not resolved in the vertical variation of electrical conductivity, as would be expected in a smoothness constrained inversion. Thus, the parameter τ, which captures the process dynamics, seems to be a better indicator for relevant structural changes than the distribution of electrical conductivity, which reflects both lithology and water saturation at a certain state. At least, this is due to the smoothness constraint in an Occam's type inversion and might be better resolved by a different regularization operator.

Temporal-based zonation has several inherent advantages over static-based zonation. Above all, as seen here, it is significantly more sensitive to hydraulic properties. Static measurements (see Appendix 5.A) would only discover significantly different layers, while the dynamic approach can indicate relatively milder changes. It is also more directly related to hydraulic properties, as shown above. The downside of course is the need to conduct a relatively long experiment.

Overall, the proposed zonation approach based on the observed process dynamics relies on the resolution of the ERT method, which decreases with increasing distance from the electrodes (i.e., with increasing depth in our case). This has to be taken into account in the same way as in the interpretation of the ERT images of electrical conductivity (Figures 5.4, 5.7, and 5.10) and may limit the reliability of the zonation results with increasing depth, see also e.g. Nguyen et al. (2009).

Biological and chemical processes were not addressed in this paper. We only focused on the physical process of water infiltration and the influence of heterogeneities of the subsurface material distribution on the infiltration. Yet, biological and chemical processes have to be taken into account for the optimization of such systems, since they can play a major role for the efficiency of an SAT site. On one hand surface and subsurface clogging (like algae or biofilm growth) decrease the infiltration rate, but on the other hand shorter residence times of the water percolating through the unsaturated zone decrease the time for bioremediation of organic matter. Nonetheless, the physical processes need to be investigated to build a foundation for further studies incorporating additional processes.

5.4 Summary & Conclusions

Our study helps in the understanding of water flow dynamics in the unsaturated zone and contributes in enhancing SAT sites, in particular at the Shafdan, but also in general for MAR/SAT sites. We monitored ponded water infiltration in the context of SAT at the Shafdan site using time-lapse geoelectrical imaging. The temporally dense measurements of ERT clearly show the moving water body during infiltration in the vadose zone, both using raw data and tomograms. We show that using dynamic data it is also possible to image heterogeneities in the vadose zone which were not visible from the background tomograms.

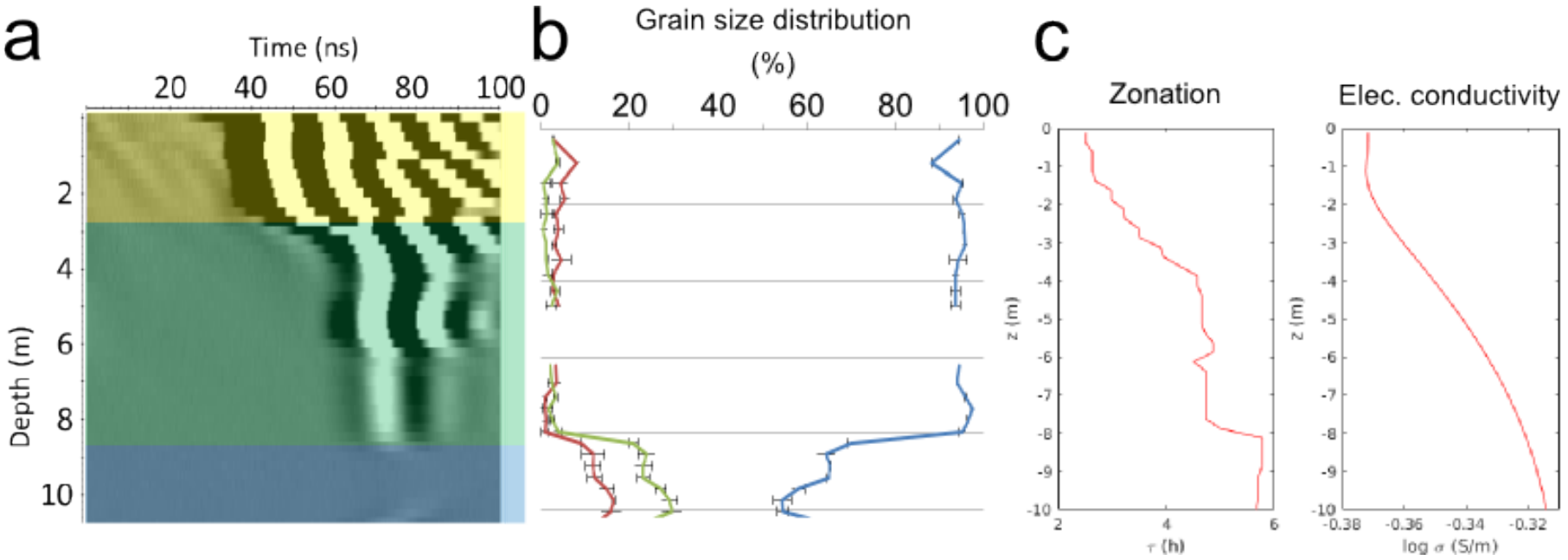

Figure 5.9: (a) Selected cross-hole GPR data from boreholes B1 and B2 and (b) selection from grain size distribution from borehole B1. (c) Vertical distribution of parameter τ (left) and electrical conductivity (right) at about $x = 42\,\text{m}$ along profile A2 (i.e., the position closest to the GPR boreholes B1 and B2; see also Figure 5.2).

We showed that ERT has the ability to monitor the vadose zone even given very high water fluxes. The ERT raw data (prior to inversion) are of value to recognize the spatial and temporal behavior of the electrical conductivity changes induced by water content changes. These raw measurements can be used as a simple and cost effective tool for SAT monitoring and control, which is highly desired for both water quantity and quality purposes. Further, we show that once a domain is mapped, an individual measurement can capture the behavior of the entire vadose zone.

Based on the temporally dense ERT images, we proposed a new approach for "temporal-based" aquifer zonation using the temporal behavior of the electrical conductivities induced by the change of water saturation during the sequences of infiltration and drying. Different behavior of the electrical conductivity breakthrough curves is indirectly related to different hydraulic properties of the subsurface material. Further investigations are needed to validate the approach, for instance via coupled numerical simulations of unsaturated flow and geoelectrical forward modeling.

The spatial information provided by the ERT images is an important advantage of the method compared to classical hydrological measurements, for instance water content measurements with TDR probes or lithological information from boreholes, which contain only point information. ERT can help to decide for the optimum infiltration cycle, i.e., to find the best timing for the next flooding related to the hydraulic state of the pond subsurface material. In combination with the synthetic hydrologic study presented in Appendix 5.B, this can be a valuable for approach for the optimization of SAT sites in particular and MAR in general.

In this study, we showed that time-lapse ERT is a powerful tool for the monitoring of SAT systems and helps to get more insights into the subsurface system and the process of water infiltration.

Acknowledgements

This work has been financed within the framework of the "German-Israeli Water Technology Cooperation Program" under the project numbers 02WA1262 / WT1203 by the German Federal Ministry of Education and Research (BMBF) and the Israeli Ministry of Science, Technology and Space (MOST). We would like to thank Mekorot Water Company LTD for the use of the infiltration pond Yavneh 2-5101 and the help regarding the operation of the pond. Further thanks go to Johannes Kenkel for the help in the field as well as to Nimrod Schwartz, Orel Kahalon, Gil Honigsman and Ziv Moreno for the work in the field and the preparation and installation of the ERT monitoring system. We would also like to thank Lev Kaufman for the help with the GPR measurements. We thank the three reviewers and the associate editor for the constructive and very helpful review of the manuscript.

Appendix 5.A

Background ERT Measurements

Various investigations were conducted to characterize the pond subsurface material before monitoring of the infiltration. Six surface ERT surveys (four lines on the surface in addition to the buried lines A2 and B1) were measured with a focus on the lower pond edge using an IRIS Instruments Syscal Pro 96 Switch resistivity meter (Figure 5.2b). The four additional ERT profiles were measured directly from the surface (no buried electrodes) with an electrode separation of 0.5 m and a total of 80 electrodes in each line. A skip-1 and skip-3 (number of skipped electrodes in a dipole) dipole-dipole acquisition with normal and reciprocal (i.e., interchanging of current and potential dipoles) measurements was applied in each of the profiles (M1-4, A2, and B1).

Figure 5.10 shows the inverted background ERT images of the subsurface to a depth of up to 10 m. They confirm the increase in water content at about 4 m depth as also seen in Figure 5.9a. Strong lateral heterogeneities are not visible here except for a change in thickness of the resistive layer associated with the dry sands.

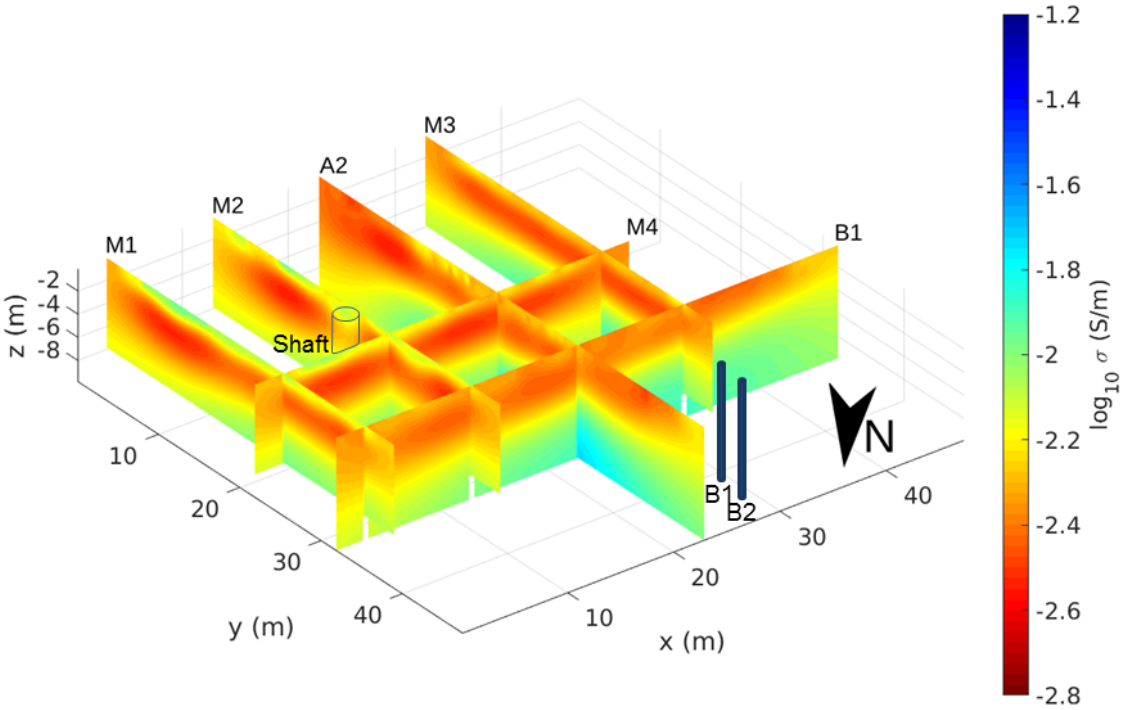

Figure 5.10: Electrical conductivity profiles for the southern end of the pond including profiles M1 to M4, A2, and B1 (compare Figure 5.2b); for orientation, the shaft and boreholes B1 and B2 are also included.

Appendix 5.B [1]

Synthetic Infiltration Experiments

Within the framework of this research project, one aim of the study, beside the time-lapse geoelectrical monitoring of water infiltration, was the optimization of ponded water infiltration in the context of SAT in terms of increasing the total volume of infiltrated water within a certain time. Therefore, a series of synthetic numerical infiltration experiments was simulated. The experiments were designed as an extension of the synthetic study in Chapter 3 (see for more details in theory of the numerical methodology). Simulations were conducted using the software iTOUGH2; however, here without geoelectrical modeling. The cyclic infiltration was investigated in order to find the highest efficiency related to infiltrated water volume.

The parameters for unsaturated water infiltration (permeability, porosity, residual water saturation, grain size distribution index) were calibrated from known parameters from the Shafdan site (for more details, see Loewy, 2010; Anger, 2014). Different cycles of infiltration were simulated by varying the period length of flooding and drying. Figure 5.11 shows exemplary the simulated water saturation at different depth for the "typical" cycle of one day flooding and two days drying. The curves show, like in the electrical data shown in the field study (see Figure 5.3), a flattening of the curves with increasing depth. The amplitudes of the breakthrough curves decrease and the slope of the curves from peak to minimum gets more flat with increasing depth.

For each of the different infiltration cycles tested, the total infiltrated water volume over a time period of 30 days was calculated and compared. Figure 5.12 shows the results of the quantification. The results reveal that different total volumes of infiltrated water are captured for different infiltration cycles. They also show that for shorter flooding and drying cycles, but the same ratio between flooding and drying (e.g., 1:1 or 1:2), the total infiltration volume increases. Since the unsaturated hydraulic conductivity is larger with higher water saturation, the subsurface contributes for higher infiltration rates within shorter drying periods. The results indicate that shorter intervals of flooding and drying may be more effective than the cycle that is used at the site. For instance, for half a day of flooding and half a day of drying, the total volume is around 250,000 m^3 whereas for three days of flooding and three days of drying it is less than 150,000 m^3. With an infiltration cycle of half a day of flooding and one day of drying (as used for the time-lapse ERT experiment), compared to the "typical" cycle (one day of flooding, two days of drying), about 30% more water can be infiltrated within the same period of time.

[1] This section is not part of the publication, but was part of the research project. The modeling and evaluation was conducted within the Bachelor Thesis by Anger (2014).

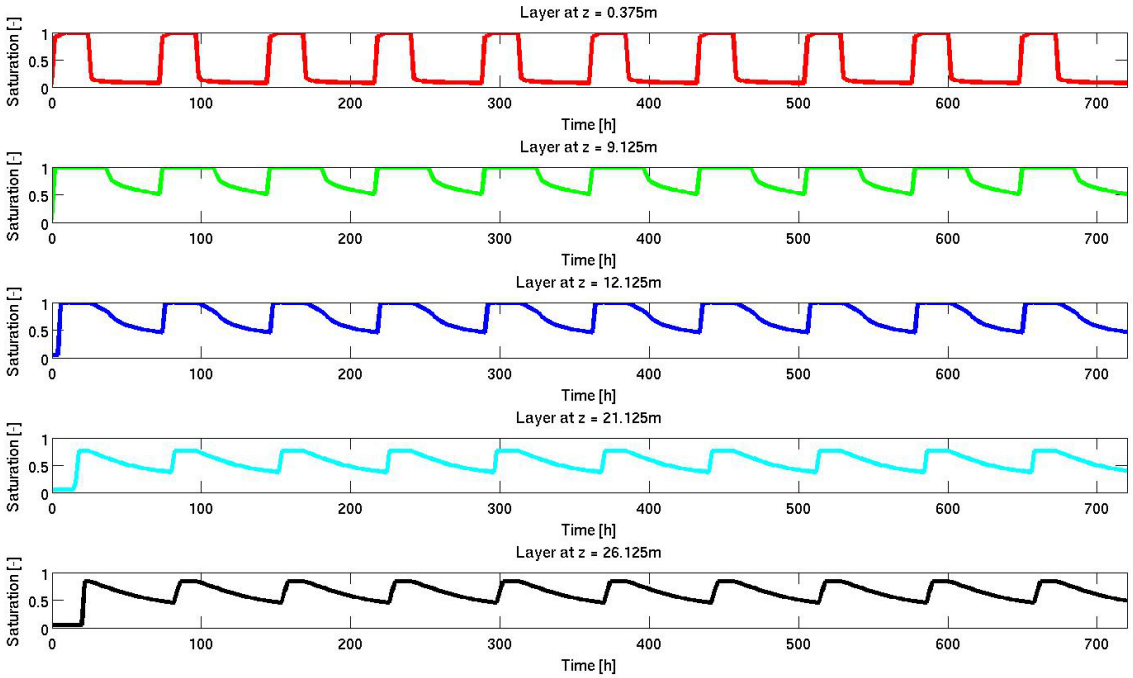

Figure 5.11: Simulation results for infiltration cycle of one day of flooding and two days of drying over a period length of 30 days. Shown is the water saturation S at different depth. Figure adopted from Anger (2014).

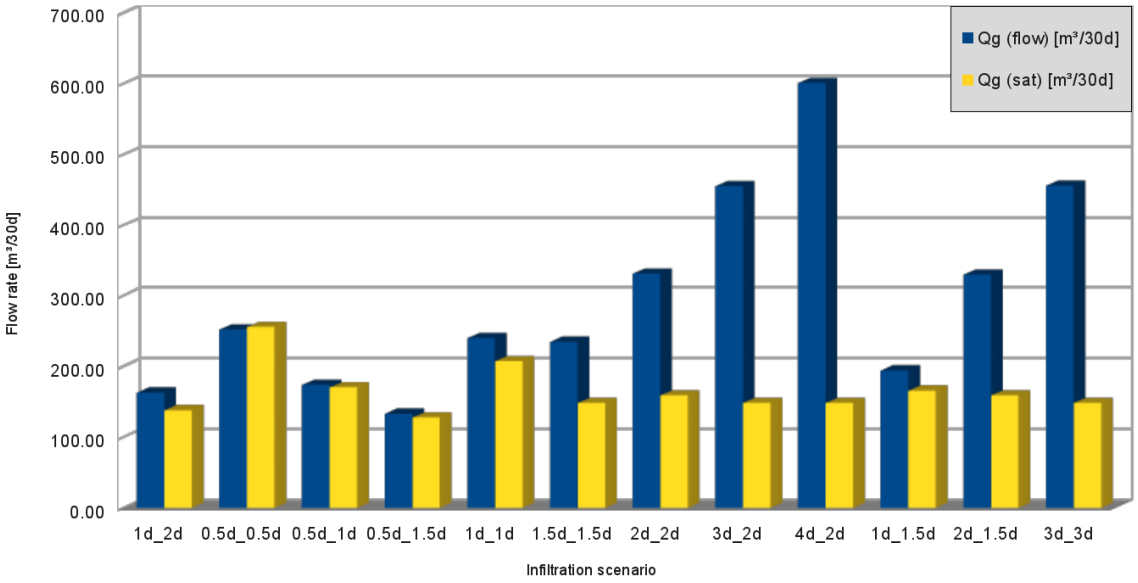

Figure 5.12: Total volume of infiltrated water over a period length of 30 days for different infiltration cycles. Specified is the duration of the flooding and of the drying period. The calculation of the total volume was conducted through the flow (blue columns) and the saturation (yellow columns) whereas the saturation is more significant here. Figure adopted from Anger (2014).

To close the link between the optimization study and the time-lapse ERT monitoring, the ERT results can be used the define the actual state of the vadose zone in terms of water saturation and therefore can be used to decide for the ideal timing of the next flooding event. For instance, this can be seen in the breakthrough curves in Figure 5.3 and in the images of the same time after start of flooding for different infiltration scenarios in Figure 5.7.

However, this synthetic study is only a very simplified quantification and only takes into account the physical process of unsaturated water infiltration. Effects like entrapped air, chemical or biological processes play a significant role on the water infiltration and thus also on the quantities of infiltrated water. A very recent study by Drumheller et al. (2017) also focuses on the optimization of MAR systems. They developed a decision making algorithm in the framework of a feasibility study with flow and transport simulations and found that the approach could improve the operation of MAR facilities.

Chapter 6

Hydrogeophysical Monitoring and Modeling of Freshwater Injection

Published in Hydrology and Earth System Sciences:

Klaus Haaken, Gian Piero Deidda, Giorgio Cassiani, Rita Deiana, Mario Putti, Claudio Paniconi, Carlotta Scudeler, and Andreas Kemna 2017. Flow dynamics in hyper-saline aquifers: hydro-geophysical monitoring and modeling. *Hydrology and Earth System Sciences* 21(3):1439-1454, doi:10.5194/hess-21-1439-2017.

Underlying data and results:

Klaus Haaken, Gian Piero Deidda, Giorgio Cassiani, Rita Deiana, Mario Putti, Claudio Paniconi, Carlotta Scudeler, and Andreas Kemna 2017. Data and results for manuscript "Flow dynamics in hyper-saline aquifers: hydro-geophysical monitoring and modeling". *Data set, Zenodo*, doi:10.5281/zenodo.322630.

6.1 Introduction

Multiphase flow in porous media has been the subject of intensive study for many decades, motivated, amongst other factors, by important economic considerations linked to the petroleum industry. Another field where interaction of pore fluids having different physical properties, which is of particular importance, is saline-freshwater systems. In this case, important density and viscosity differences between saline and fresh waters control the relative motion and mixing of the two phases. Characterizing and modeling these coupled flow and transport phenomena is a very challenging task, particularly in the presence of the hydraulic heterogeneities always present in natural porous media (e.g., Werner et al., 2013; Ketabchi et al., 2016).

The most common situation where saline-freshwater systems have practical environmental and socio-economic implications is related to seawater intrusion in coastal aquifers, often exacerbated by overexploitation of groundwater, particularly in arid and semi-arid regions such as those surrounding the Mediterranean basin (e.g., Kallioras et al., 2010; Rey et al., 2013; Dentoni et al., 2015). Another context where the study of saline-freshwater interactions is highly important is the injection and storage of freshwater in brackish or salty aquifers for later use in agriculture or for domestic purposes, also known as aquifer storage and recovery (ASR; e.g., Pyne, 1995; Dillon, 2005).

Many studies of density-dependent flow and transport phenomena in porous media have been conducted over the past decades (e.g., Gambolati et al., 1999; Simmons et al., 2001; Diersch and Kolditz, 2002). Instabilities and fingering can take place when denser water overlies lighter water (e.g., Simmons et al., 2001). Ward et al. (2007) gave an introductive literature review on density-dependent modeling, with a particular focus on ASR. The first studies on the injection of freshwater into a saline aquifer were performed by Bear and Jacobs (1965) and Esmail and Kimbler (1967). The latter investigated the tilting of the saltwater-freshwater interface, a phenomenon known as "buoyancy stratification". More recent studies have analyzed the efficiency of ASR for both field and synthetic cases (e.g., Kumar and Kimbler, 1970; Moulder, 1970; Kimbler et al., 1975; Ward et al., 2007, 2008; Lu et al., 2011; Zuurbier et al., 2014). Ward et al. (2008) conducted a numerical study to evaluate the efficiency of ASR under density-dependent conditions with anisotropy and heterogeneity of high and low permeable layers. van Ginkel et al. (2014) studied the possibility of extracting saltwater below the freshwater injection to prevent the spreading of freshwater at the top of the aquifer. Alaghmand et al. (2015) investigated fresh river water injection into a saline floodplain aquifer and developed a numerical model for the optimization of injection scenarios.

The behavior of saline-freshwater systems becomes increasingly complex with larger density and viscosity contrasts. To date, very little research has been done on the effects of freshwater injection in highly saline aquifers that can reach total dissolved solids concentrations of $100\,\mathrm{g\,l^{-1}}$. Understanding these complex systems is limited not only by the need to develop non-trivial coupled flow and transport models but also by the scarce availability of effective monitoring techniques. The latter are, under field conditions, typically limited to borehole measurements that can only provide point information in spatially heterogeneous hydraulic systems with time-

changing salt concentrations.

As in many other subsurface characterization problems, a major contribution can be made by non-invasive, spatially extensive, geophysical techniques. In particular, electrical and electromagnetic methods are very suitable in the context of saline-freshwater interactions, since electrical conductivity varies over orders of magnitude depending on solute concentrations. While the use of these methods is common in seawater intrusion studies (e.g., Goldman and Kafri, 2006; Nguyen et al., 2009), only few studies have used geophysics to monitor ASR experiments. Davis et al. (2008) used time-lapse micro-gravity surveys to monitor the utilization of an abandoned coal mine as an artificial ASR site. Maliva et al. (2009) investigated the use of geophysical borehole logging tools applied to managed aquifer recharge systems, including ASR, to improve the characterization of aquifer properties. Minsley et al. (2011) developed an integrated hydro-geophysical methodology for the siting, operation, and monitoring of ASR systems using electrical resistivity, time-domain electromagnetics, and seismic methods. Parsekian et al. (2014) applied geoelectrical imaging of the subsurface below an aquifer recharge and recovery site alongside with hydrochemical measurements to identify preferential flow paths.

A major step forward in saline-freshwater systems monitoring can be made by improving the efficiency of advanced geophysical techniques, and electrical tomographic methods in particular. Electrical resistivity tomography (ERT) is widely used today in hydrogeological and environmental investigations. Often applied in tracer studies (e.g., Kemna et al., 2002; Vanderborght et al., 2005; Cassiani et al., 2006; Doetsch et al., 2012b), ERT is a natural choice for saline-freshwater interaction monitoring, given the correlation between the salinity of a pore fluid and its electrical conductivity. Time-lapse ERT, where only the changes in electrical conductivity over time are imaged (e.g., Kemna et al., 2002; Singha and Gorelick, 2005; Perri et al., 2012), can be especially effective in tracking dynamic processes. Whereas tracer studies are typically designed with injection of a saline tracer into fresh surrounding groundwater, only very few studies have dealt with the inverse case of freshwater injection into a saline formation. For instance, Müller et al. (2010) conducted tracer tests using also a less dense tracer with lower electrical conductivity than the ambient groundwater, monitored with ERT.

The goal of this study is to present a general approach for the characterization, monitoring, and modeling of complex saline-freshwater systems, based on the combination of non-invasive techniques and accurate numerical modeling. To our knowledge, no such a comprehensive hydro-geophysical approach concerning freshwater injection in saline aquifers has been presented so far in the scientific literature; thus, we believe this case study can be very useful as a starting point for other, more comprehensive methodological testing. In this study we limit ourselves to integrating field data and modeling in a loose manner, with no aim at this stage to develop a full data assimilation framework, as implemented elsewhere for simpler systems (e.g., Manoli et al., 2015; Rossi et al., 2015). The key message that can be derived from the joint use of advanced field techniques and advanced numerical modeling is nonetheless apparent in the presented case study, and more complete assimilation approaches are possible provided that the advantages and limitations of the individual components (data and models) are fully understood as shown in the present paper.

The approach is presented in the context of a case study where we injected freshwater into a hyper-saline aquifer in the Molentargius Saline Regional Park in southern Sardinia, Italy. The experiment was monitored using cross-hole time-lapse ERT. To investigate the mixing processes, the resulting ERT images are compared with the results of a synthetic numerical study of the same experiment. We consider here both homogeneous and heterogeneous (layered) systems. For a quantitative comparison between the field and synthetic studies, spatial moments of the freshwater bulb are calculated.

6.2 Field Experiment

6.2.1 Site Description

The Molentargius Saline Regional Nature Park is located east of Cagliari in southern Sardinia, Italy (Figure 6.1). The park is a wetland situated very close to the coastline. The exceptional nature of the site is given by the presence of both freshwater and salty water basins separated by a flat area with mainly dry features (called "Is Arenas"). The freshwater areas include two ponds that originated as meteoric water retention basins. The salty water areas include the stretches of water of the former system of the Cagliari salt pans.

The park area is characterized by an oligocenic-miocenic sedimentary succession of ca. 100 m (Ulzega and Hearty, 1986) overlaid by pleistocenic deposits of marine and continental origin and by alluvial and offshore bar deposits, whose origin is still debated (Coltorti et al., 2010; Thiel et al., 2010). This ongoing scientific debate has implications for the comprehension of the phenomenon of hyper-saltiness of the park groundwater.

The specific site of investigation is located in the flat dry area within the park (Is Arenas, Figure 6.1c). The water table of the unconfined aquifer is stable at 5.2 m below ground surface (b.g.s.), and practically neither lateral groundwater flow nor tidal effects are evident. The sediments are composed mostly of sands, with thin layers of silty sand, clayey sand, and silty clay (Figure 6.2). The groundwater reaches salinity levels as high as three times the NaCl concentration of seawater. Such high salt concentration is likely the long-term legacy of infiltration of hyper-saline solutions from the salt pans dating back, in this area, to Roman times. Electrical conductivity fluid logs (see Figure 6.3) recorded in boreholes allowed two zones to be discriminated, with a transitional layer in between: (1) from the water table to a depth of 6.5 m the water electrical conductivity is about $2\,\mathrm{S\,m^{-1}}$, and (2) below 12 m depth the water electrical conductivity reaches $18.5\,\mathrm{S\,m^{-1}}$. Note that Figure 6.3 also reports the time-lapse evolution of the vertical electrical resistivity profile as a result of the freshwater injection described in the following section.

6.2.2 Freshwater Injection

Five boreholes for ERT measurements were drilled with 101 mm inner diameter to a depth of 20 m and positioned in the shape of a square with 8 m sides (four corner

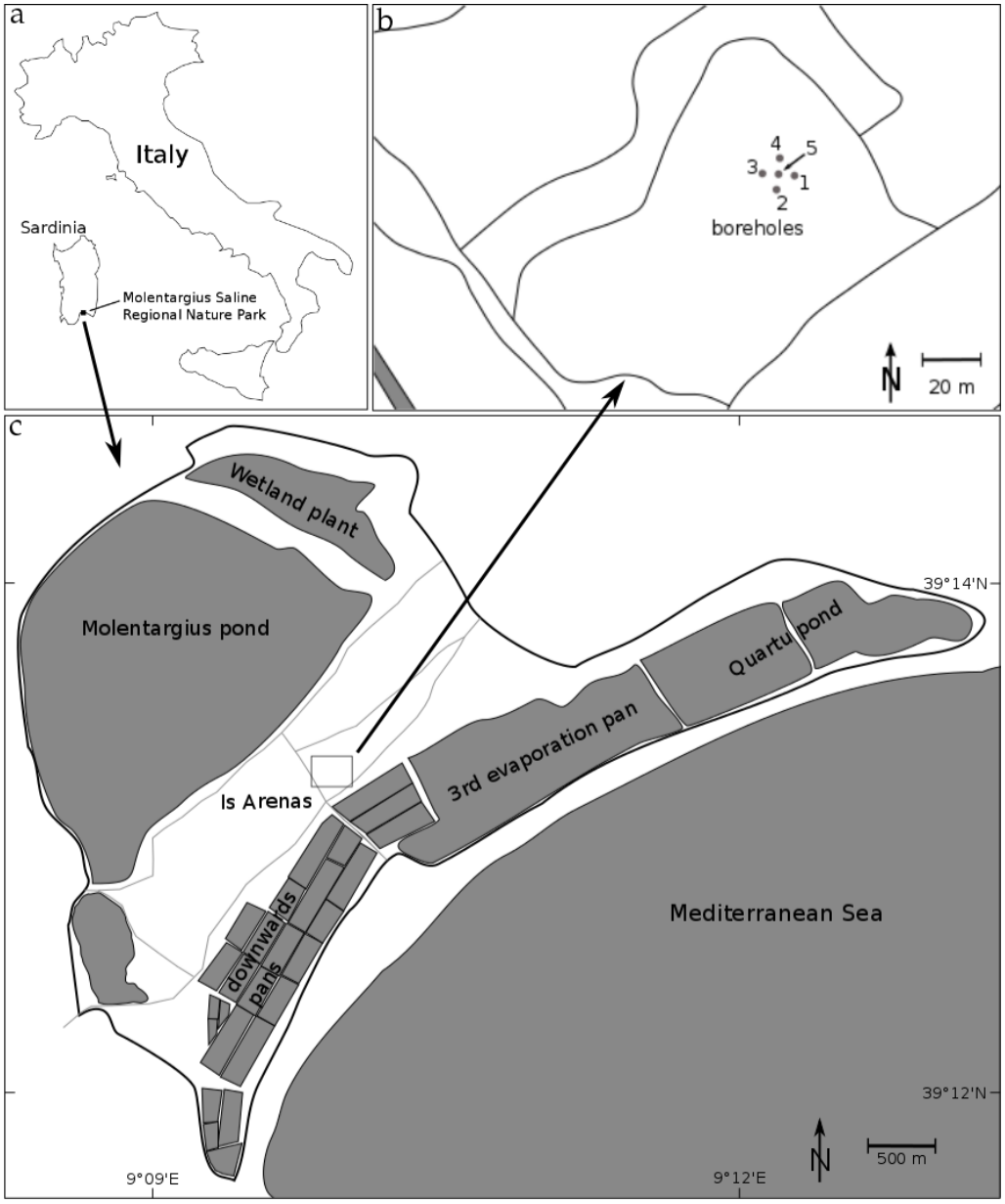

Figure 6.1: Geographical location of the test site: (a) Molentargius Saline Regional Nature Park located east of Cagliari in southern Sardinia, Italy, (b) Detailed sketch map of location and arrangement of the boreholes, (c) Sketch map of the Molentargius Park (modified according to Google Earth).

boreholes) and one borehole at the center (Figure 6.1b). All boreholes are equipped with a fully screened PVC pipe (screen with 0.8 mm size).

In November 2011, 19.4 m^3 of freshwater with an electrical conductivity of 0.03 $S\,m^{-1}$, stored in a tank, was injected into the saline aquifer. This was done through the central borehole using a double packer system with an injection segment of 1 m length. The injection chamber was set between 13 m and 14 m b.g.s. The injection rate was entirely controlled by the natural pressure gradient, given by the water head in the tank and the depth of injection (i.e., 13 m to 14 m b.g.s. plus 2 m head in the tank

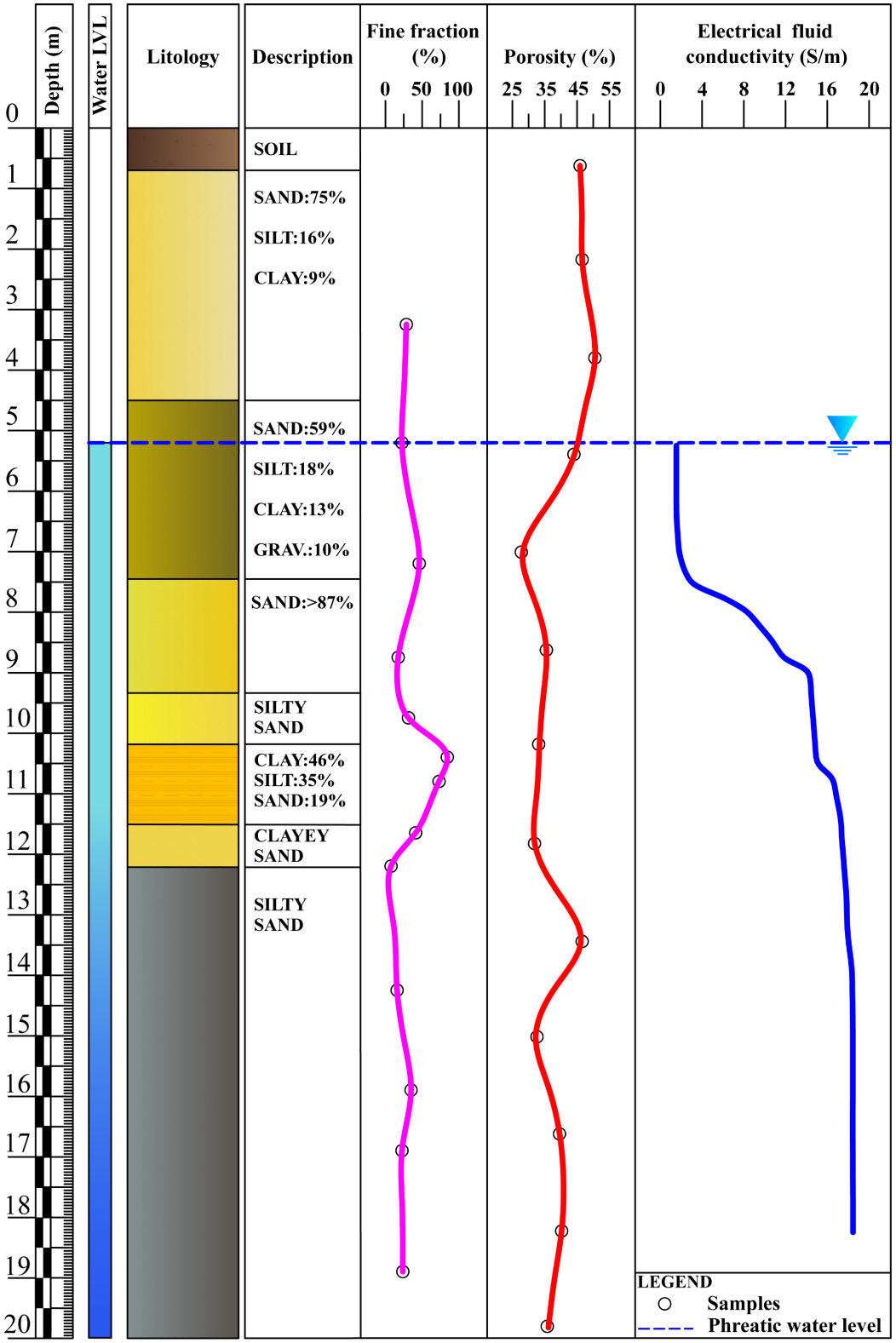

Figure 6.2: Generalized stratigraphy log from the five drilled boreholes including lithology, percentage of fine fraction, and porosity from samples as well as electrical conductivity of borehole fluid. The water table lies at 5.2 m b.g.s..

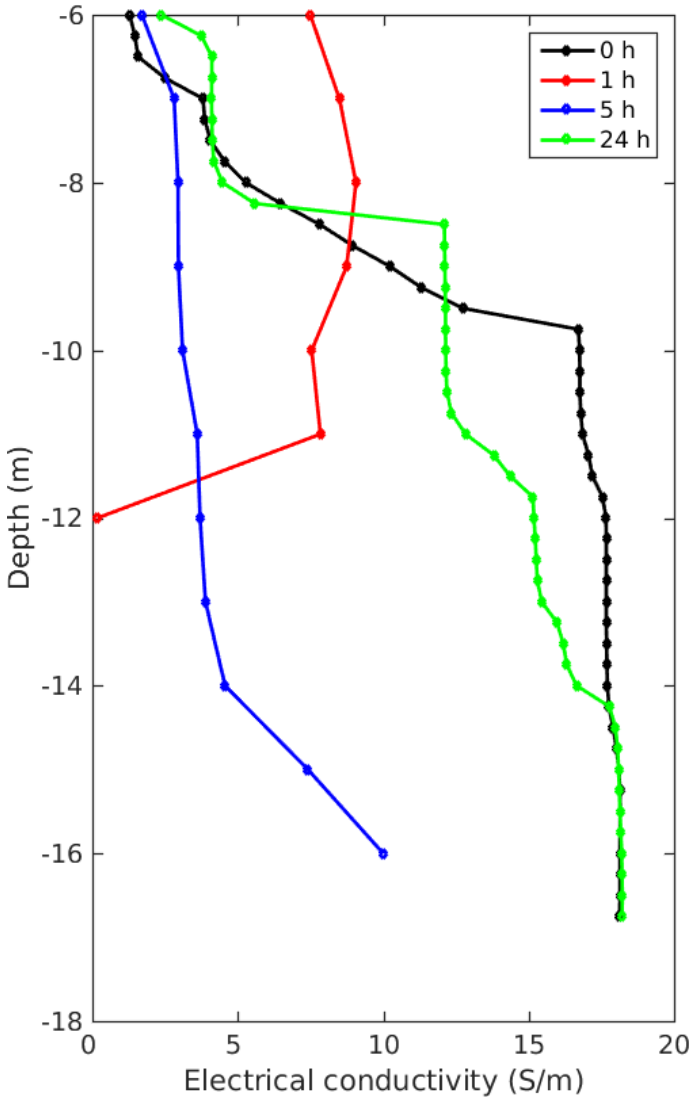

Figure 6.3: Electrical conductivity log of the fluid in borehole 5 at different times after start of freshwater injection (Section 6.2.2). 0 h denotes the background measurement before injection. At 1 h there are no measurements below 12 m b.g.s. because the packer system occupied the borehole.

above the surface). The natural pressure gradient provided for an initial injection rate of $0.5\,\mathrm{l\,s^{-1}}$. However, during injection (after about 1.5 h) this rate immediately rose to a rate of about $2.75\,\mathrm{l\,s^{-1}}$. We assume that this was due to a clogging of the backfill material, which was "de-clogged" after 1.5 h. In total, discharging the tank took about 4 h.

6.2.3 ERT Monitoring

The direct electrical conductivity measurements described in the previous subsection correspond to the data that would be available as a result of a standard monitoring plan, and is highly insufficient for drawing any conclusions concerning the processes that take place during and after freshwater injection. The available dataset was

great enriched by ERT measurements, described below.

6.2.3.1 Data Acquisition

Time-lapse ERT monitoring was applied during the injection experiment in order to image the developing freshwater bulb, "visible" thanks to its lower electrical conductivity compared to the surrounding saltwater. Each borehole bears externally to the casing 24 stainless steel cylindrical electrodes, permanently installed from 0.6 m to 19 m depth with 0.8 m separation, with the exception of the central borehole where the first electrode is placed at the surface and the last at 18.4 m depth. ERT measurements were carried out in a 2D fashion, along two vertical planes diagonal along the boreholes, i.e., one plane was using the borehole numbers 1, 5, and 3 and the second plane the borehole numbers 2, 5, and 4 (see Figure 6.1b), thus making use of 72 electrodes per plane. This choice, in contrast to a full 3D acquisition, was predicated on minimizing the acquisition time, given that the freshwater-saltwater movement was expected to be relatively rapid.

The ERT measurements were conducted using a Syscal Pro and adopting different configuration setups, consisting of in-hole dipole-dipole measurements in a skip-zero mode (i.e., adjacent electrodes form a dipole) and cross-hole dipole-dipole (hereafter referred to as bipole-bipole) measurements (Figure 6.4). Measurements were collected in normal and reciprocal configurations (i.e., exchanging the current and potential dipoles) for estimation of data errors. The acquisition for one complete measurement frame (consisting of roughly 7,300 individual readings) required about 40 minutes.

ERT data were acquired in a time-lapse manner to investigate the changes over time caused by the electrical conductivity changes of the developing freshwater bulb within the saline aquifer. The first time step, t_0, was acquired before the start of injection in order to compare the following individual time steps with the background image. These were measured on the day of injection, one day after injection, and five days after injection.

6.2.3.2 Data Processing and Time-lapse ERT Inversion

Due to technical errors (such as bad connection of electrodes, problems with power supply) and varying data quality, the ERT data were processed prior to inversion. In particular, data having a misfit larger than 5% between normal and reciprocal readings were removed.

The temperature difference between the groundwater (21 °C) and the injected freshwater (18 °C) was relatively small. Changes in electrical conductivity due to temperature effects are in this case about 5% (see, e.g., Sen and Goode, 1992). Compared to the variation in electrical conductivity between the two fluids, which is about three orders of magnitude, the temperature effect is considered negligible.

The ERT field data from the freshwater injection experiment were inverted using the smoothness-constraint inversion code CRTomo. A full description of the code is given by Kemna (2000). In the inversion, the data errors are represented according

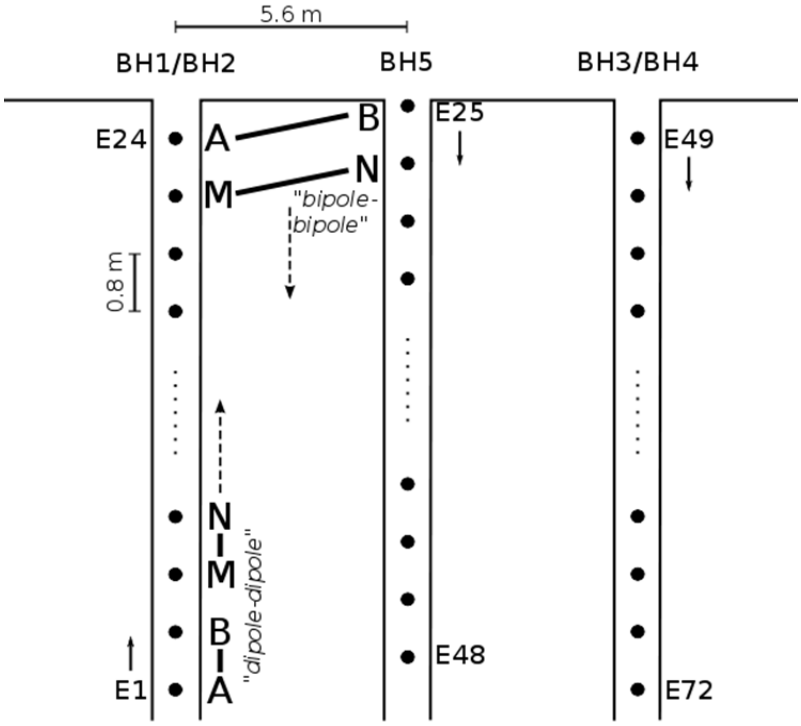

Figure 6.4: Schematic description of the ERT measurement configurations used. For dipole-dipole measurements, one dipole is always within one borehole, the other dipole also moves into the adjacent borehole. Bipole-bipole measurements are done as cross-hole measurements and are also changing as diagonals (i.e., A stays while B moves downwards for up to five electrode positions before A is also moved, similarly for M and N).

to a linear model expressed as $\varepsilon = aR + b$, where R is the measured electrical resistance. For the case at hand, the error parameters a (absolute) and b (relative) were set to $0.0001\,\Omega$m and 10%, respectively.

Resistivity images exhibit a variable spatial resolution (e.g., Ramirez et al., 1995; Alumbaugh and Newman, 2000; Nguyen et al., 2009). A useful indicator for this variation is the cumulative sensitivity $\boldsymbol{s}$ (e.g., Kemna et al., 2002; Nguyen et al., 2009). The sensitivity indicates how a change in electrical resistivity of a certain model cell affects a transfer resistance measurement. Analogously, the cumulative sensitivity quantifies the change of a complete dataset to a changing model cell, and its analysis is an important step in the inversion process. Note that an objective choice for a threshold, which identifies zones where "reliable" vs. "unreliable" ERT imaging, is not feasible. In a more qualitative manner one can assume, empirically, that a cumulated sensitivity clearly below 10^{-3} leads to weak imaging. Figure 6.5 shows exemplarily the cumulative sensitivity distribution for the inversion of one dataset (image plane boreholes 1-5-3 at time t_0, i.e., the background image). The geometry of the boreholes and the electrodes, in combination with the employed measurement configurations, yields a relatively good coverage within the area of interest (i.e., mainly the area around the central borehole).

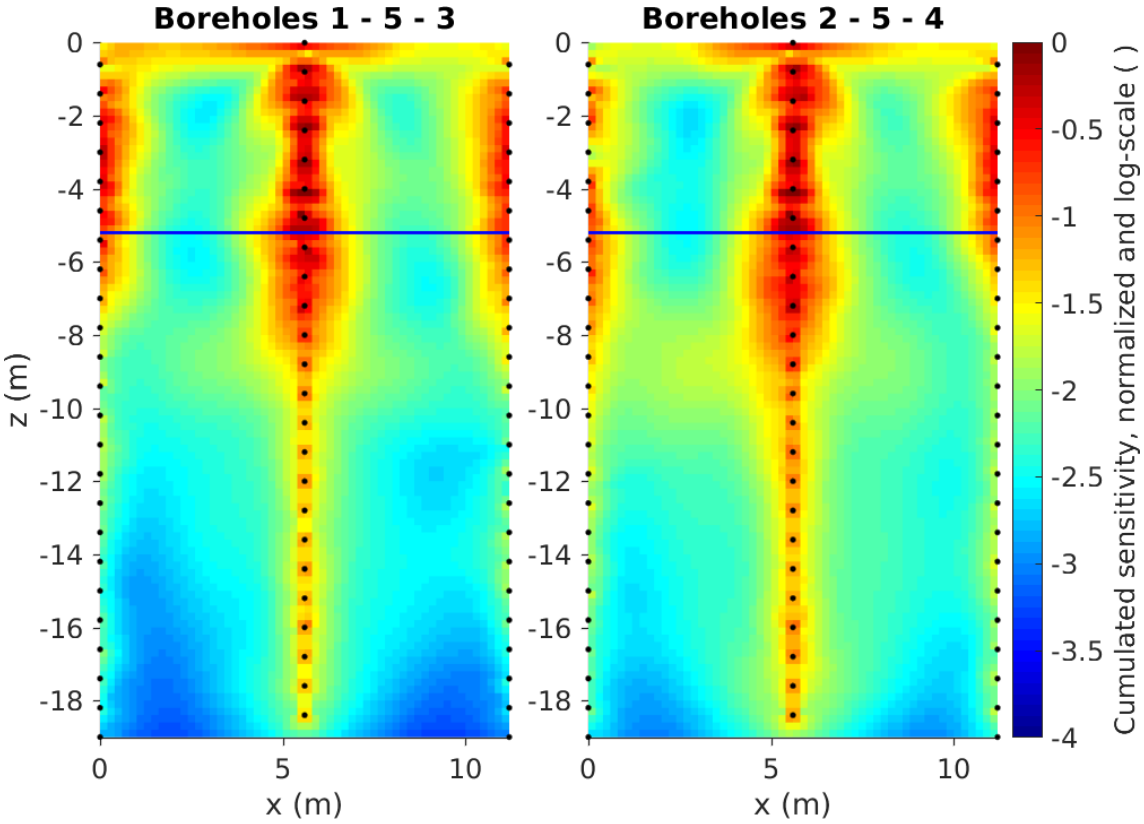

Figure 6.5: Cumulated sensitivity distribution for the inverted background (t_0) datasets for both planes.

In a time-lapse monitoring framework, one is primarily interested in the temporal changes of data and parameters. Therefore, we used the "difference inversion" approach of time-lapse ERT (e.g., LaBrecque and Yang, 2000; Kemna et al., 2002), where the inversion results are changes with respect to the background data at time t_0. The advantage of this approach is that modeling errors and data errors correlated over time are canceled out to a significant degree and associated imaging artifacts that would occur in a standard inversion are suppressed.

6.2.3.3 ERT Imaging Results

The ERT dataset was collected under challenging conditions, in particular as the very large salinity contrasts are manifested as extreme electrical conductivity differences over space and time. Large electrical conductivity can occasionally bring DC electrical currents into a nonlinear (non-Ohmic) regime, which in turn can lead to violation of the conditions for the reciprocity theorem (Binley et al., 1995; Cassiani et al., 2006). This has clear implications in terms of data processing, as in particular the error analysis based on reciprocal resistances may not guarantee that direct and reciprocal resistances are equal to each other. Filtering the data according to a reciprocity discrepancy equal to the data error level chosen for the inversion (see above) meant that a fairly large percentage of the data (about 50%) were rejected.

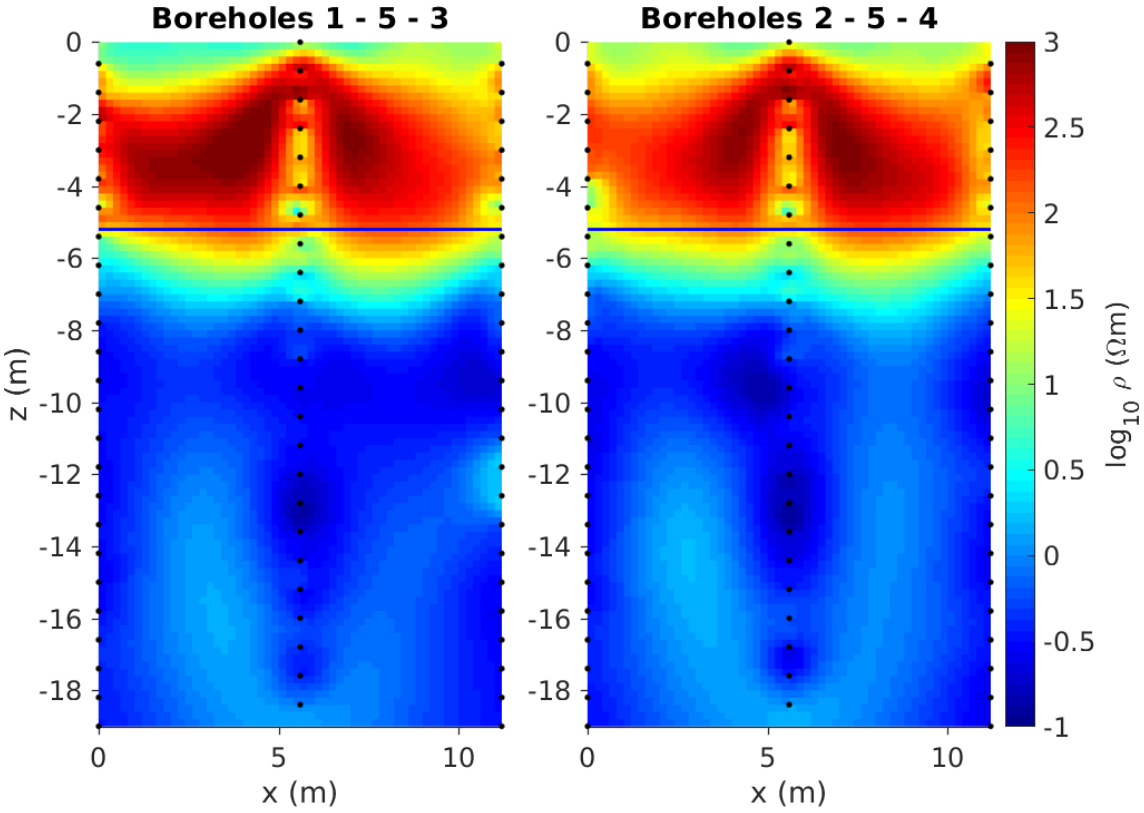

Figure 6.6: Inverted background (t_0) images for both planes, including the unsaturated zone. Black diamonds denote the position of the electrodes and the blue line shows the groundwater table at 5.2 m b.g.s.

Nonetheless, a large volume of resistance data were still retained (nearly 2,000 values per time instant).

The very high electrical conductivity of the system, which is characteristic of this experiment, has also another consequence: separated inversion of the different electrode configurations (dipole-dipole and bipole-bipole) showed that the bipole-bipole configurations provide better overall results than the dipole-dipole configuration results (not shown here). This is not a common situation, as observed elsewhere in situations of standard resistivity ranges (e.g., Deiana et al., 2007, 2008), where dipole-dipole data provide higher resolution images than bipole-bipole data that generally only give smoother images as information is averaged over large volumes. In the case shown here, for an in-hole current dipole, the current lines will not penetrate far away from the borehole as they are short-circuited by the large electrical conductivity of saline water surrounding at all times the external boreholes, whereas for the cross-hole current bipole the current lines "have to" penetrate through the volume between the boreholes. Thus, the sensitivity for the dipole-dipole configurations decreases very strongly with increasing distance from the boreholes. However, the dipole-dipole configuration still manages to provide high sensitivity in the area close to the central borehole, particularly at measurement times where the freshwater bulb surrounds this borehole. Hence, the data coming from both configurations were used for inversion.

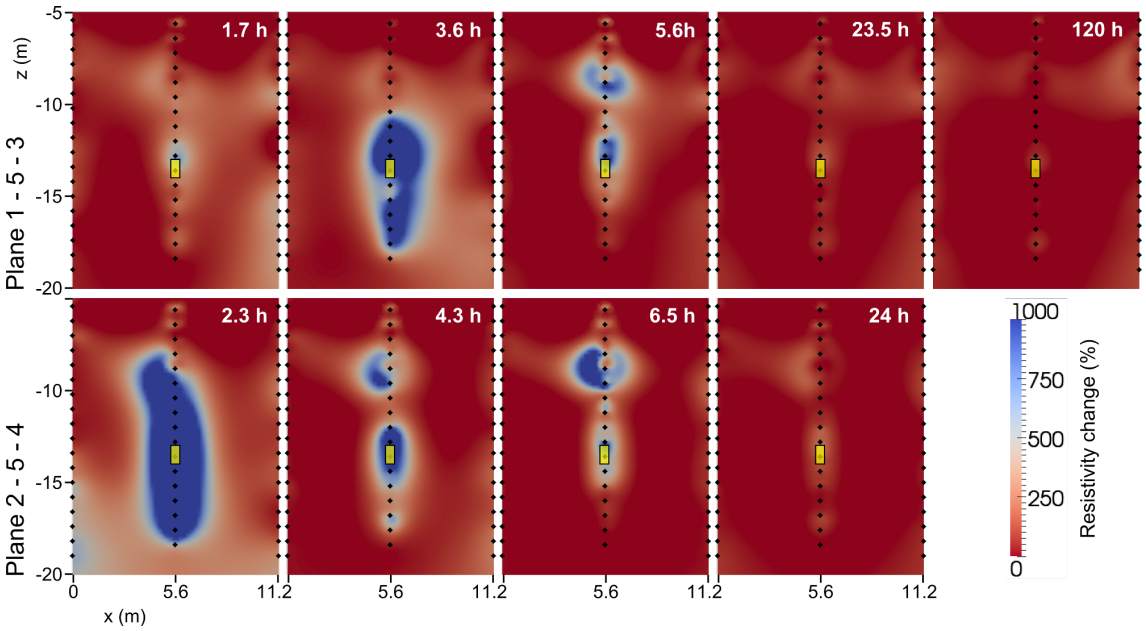

Figure 6.7: Electrical imaging (difference inversion) results for the field experiment at different times (in hours after start of injection). The top panel shows the results from borehole plane 1-5-3 and the bottom panel from plane 2-5-4. Black diamonds denote the position of electrodes.

Figure 6.6 shows the background image (time t_0) before the start of freshwater injection. The electrical resistivity of the saturated zone is very low and vertical changes due to layering of lithologies are not visible. Only a gradual change to higher resistivities in the upper part just below the water table can be seen. This can partly be attributed to the smoothness constraint applied in ERT inversion. However, this feature is also consistent with background conductivity logs (Figure 6.3).

The obtained time-lapse ERT images of the freshwater injection experiment are shown in Figure 6.7: the distribution of the injected freshwater in the aquifer surrounding the central borehole is clearly visible, in agreement with the time-lapse conductivity logs in Figure 6.3. The very fast vertical migration of the freshwater plume is also apparent. Between 2 h and 6 h after the start of injection, the injection borehole (and its surroundings) is nearly totally filled with freshwater, as confirmed by Figure 6.3 (after 5 h). However, from the ERT images the freshwater also seems to move downwards below the injection chamber. A few hours after injection, the freshwater plume nearly disappeared in the ERT images, and one day after injection the ERT image seems to have gone back to the background situation (as also confirmed by the conductivity logs in Figure 6.3).

At about 10 m to 11 m depth, the difference images show a separation of the plume into two parts. A layer of finer sediments (see Figure 6.2) is likely to cause this separation. Note that the overall high electrical conductivity masks these lithological differences in the background ERT images. This fine layer is a hydraulic barrier that forces freshwater to flow even more through the preferential flow path provided by the borehole itself and its surrounding gravel pack. Above the fine layer, the plume

expands again due to the larger hydraulic conductivity of the coarser sediments.

During the experiment, the water table as well as the electrical conductivity and the temperature of the borehole fluid were measured manually in all five boreholes. The water table rose about 1.5 m in the injection borehole and about 0.2 m in the surrounding four boreholes. The electrical conductivity log of the central borehole before, during, and after injection is shown in Figure 6.3. It can be observed that during injection (i.e., about 1 h after start of injection), the saltwater in the borehole was pushed up by freshwater. Shortly after injection stopped (5 h after start of injection) the freshwater filled the entire borehole length, whereas it is visible that the saltwater already entered the borehole in the bottom part (at about 16 m depth) and made its way upwards. Therefore, one day after the injection experiment, the fluid electrical conductivities in the central borehole were practically back to their initial values, with small differences between 8 m and 14 m depth still visible. The electrical conductivities of the fluid in the four corner boreholes showed only small changes that nonetheless indicate that part of the freshwater bulb also reached the outer boreholes.

6.3 Synthetic Experiment

In order to investigate the behavior of the injected freshwater bulb, and assess in particular the influence of the subsurface hydraulic properties on the bulb evolution, we performed a synthetic study based on the field experiment. This was undertaken using a density-dependent flow and transport simulator. Given the computational burden of the simulations and our goal of examining in detail some of the governing parameters, we did not use a data assimilation approach at this stage, opting instead for analyses of specific scenarios. We considered four scenarios of hydraulic conductivity distribution, and compared the simulated results to each other and with the field evidence in order to gain some first insights on the dynamic response of the hyper-saline-freshwater system.

6.3.1 Flow and Transport Modeling

For the coupled flow and transport modeling of the freshwater injection experiment, we used a 3D density-dependent mixed-finite element-finite volume simulator (Mazzia and Putti, 2005). This algorithm was shown to be very effective in the presence of advection-dominated processes or instabilities in the flow field induced by density variations (Mazzia and Putti, 2006). Here, groundwater flow is described by Darcy's law

$$\boldsymbol{v} = -K_s \boldsymbol{\nabla}(\psi + z), \tag{6.1}$$

where $\boldsymbol{v}$ is the Darcy flux or velocity, K_s is the saturated hydraulic conductivity tensor, ψ is the pressure head and z the elevation head. The hydraulic conductivity

is expressed in terms of the intrinsic permeability k and the properties of the fluid as

$$K_s = k\frac{\varrho_0 g}{\mu_0}, \tag{6.2}$$

where ϱ_0 is the density of freshwater, g the gravitational acceleration and μ_0 the viscosity of freshwater. For density-dependent flow, the density and viscosity of the solution are strongly dependent on the concentration of the solution:

$$\varrho = \varrho_0 e^{\epsilon c}, \tag{6.3}$$

$$\mu = \mu_0 e^{\epsilon' c}. \tag{6.4}$$

Here c is the normalized concentration (i.e., the ratio between the concentration of the solution and the maximum concentration) and ϵ and ϵ' are the density and viscosity ratios, respectively, defined as

$$\epsilon = \frac{\varrho_s - \varrho_0}{\varrho_0}, \tag{6.5}$$

$$\epsilon' = \frac{\mu_s - \mu_0}{\mu_0}, \tag{6.6}$$

where ϱ_s and μ_s are the saltwater maximum density and viscosity, respectively. In our case, the density and viscosity ratios are $\epsilon = 0.084$ and $\epsilon' = 0.28$, respectively (see also Table 6.1). For the exponential laws in Equations 6.3 and 6.4, we used a linear approximation (i.e., $\varrho = \varrho_0(1 + \epsilon c)$ and $\mu = \mu_0(1 + \epsilon' c)$) to reduce the computational cost while introducing only a negligible inaccuracy.

The mass conservation equations for the coupled flow and transport model can be written as (Gambolati et al., 1999):

$$S_s(1 + \epsilon c)\frac{\partial \psi}{\partial t} = \boldsymbol{\nabla} \cdot [K_s \frac{1 + \epsilon c}{1 + \epsilon' c}(\boldsymbol{\nabla}\psi + (1 + \epsilon c)\boldsymbol{\eta_z})] - \phi\epsilon\frac{\partial c}{\partial t} + \frac{\varrho}{\varrho_0}q^*, \tag{6.7}$$

$$\boldsymbol{v} = -K_s \frac{1 + \epsilon c}{1 + \epsilon' c}(\boldsymbol{\nabla}\psi + (1 + \epsilon c)\boldsymbol{\eta_z}), \tag{6.8}$$

$$\phi\frac{\partial c}{\partial t} = \boldsymbol{\nabla} \cdot (D\boldsymbol{\nabla} c) - \boldsymbol{\nabla} \cdot (c\boldsymbol{v}) + qc^* + f, \tag{6.9}$$

where S_s is the specific storage, t is time, $\boldsymbol{\eta_z}$ is the unit vector in z direction, ϕ the porosity, q^* is a source (positive)/sink (negative) term, $\boldsymbol{v}$ is the Darcy velocity, D is hydrodynamic dispersion, c^* is the normalized concentration of salt in the injected/extracted fluid, and f is the volumetric rate of injected (positive)/extracted (negative) solute that does not affect the velocity field (Mazzia and Putti, 2006).

For the flow and transport model we used a 3D mesh (Figure 6.8) with about 57,000 tetrahedral elements and 10,000 nodes. The size of the mesh was a good compromise between mesh resolution and computational effort. The computational domain

extends for 20 m in the x and y directions and 15 m in z direction, starting at 5 m b.g.s., thus representing only the saturated zone. This choice focuses our attention on the processes of interest and reduces dramatically the numerical complexity of modeling coupled flow and transport processes in variably saturated porous media. However, because a water table rise was observed in the boreholes during the injection experiment, we needed to account for this pressure transient in the flow and transport model. Thus, we simulated a comparable injection experiment using a 3D variably saturated flow simulator (Paniconi and Wood, 1993). The changing pressure values due to the water table rise at 5 m depth were then taken as top boundary conditions for the fully saturated flow and transport model.

Table 6.1: Flow and transport input parameters for the different zones in the model.

Parameter	Symbol	Value	Unit
Model			
Aquifer thickness (z direction)	H	15	m
Horizontal extent (x and y directions)	L	20	m
Thicknesses of aquifer layers			
Upper layer		5.4	m
Middle layer		1.2	m
Bottom layer		8.4	m
Hydraulic conductivities			
Aquifer			
Upper layer		10^{-5}-10^{-3}	m s^{-1}
Middle layer		10^{-6}-10^{-5}	m s^{-1}
Bottom layer		10^{-5}	m s^{-1}
Well			
Injection chamber		10^{-3}	m s^{-1}
Packer system		10^{-12}	m s^{-1}
Remaining well		1	m s^{-1}
Gravel pack			
Clogging effect		10^{-4}-10^{-3}	m s^{-1}
Remaining gravel		10^{-2}	m s^{-1}
Solid and fluid properties			
Porosity	ϕ	0.35	-
Longitudinal dispersivity	α_L	10^{-5}	m
Transverse dispersivity	α_T	10^{-5}	m
Diffusion coefficient	D^*	0	
Density difference ratio	ϵ	0.084	-
Viscosity difference ratio	ϵ'	0.28	-
Injection parameters			
Injected volume	V_{mod}	20	m^3
Injection duration		3.5	h

In addition to the boundary condition described above for pressure and with $c = 0$, we set Dirichlet conditions also on the lateral boundaries with a hydrostatic pressure, according to the concentration dependency $\psi = -(1 + \epsilon c)z$ and Neumann no-flow conditions at the bottom of the mesh. The flow and transport parameter values are given in Table 6.1. The injection borehole was modeled as a preferential flow path by giving the corresponding cells a large value of hydraulic conductivity. Also the borehole backfill material was included in the simulation by giving it a slightly higher

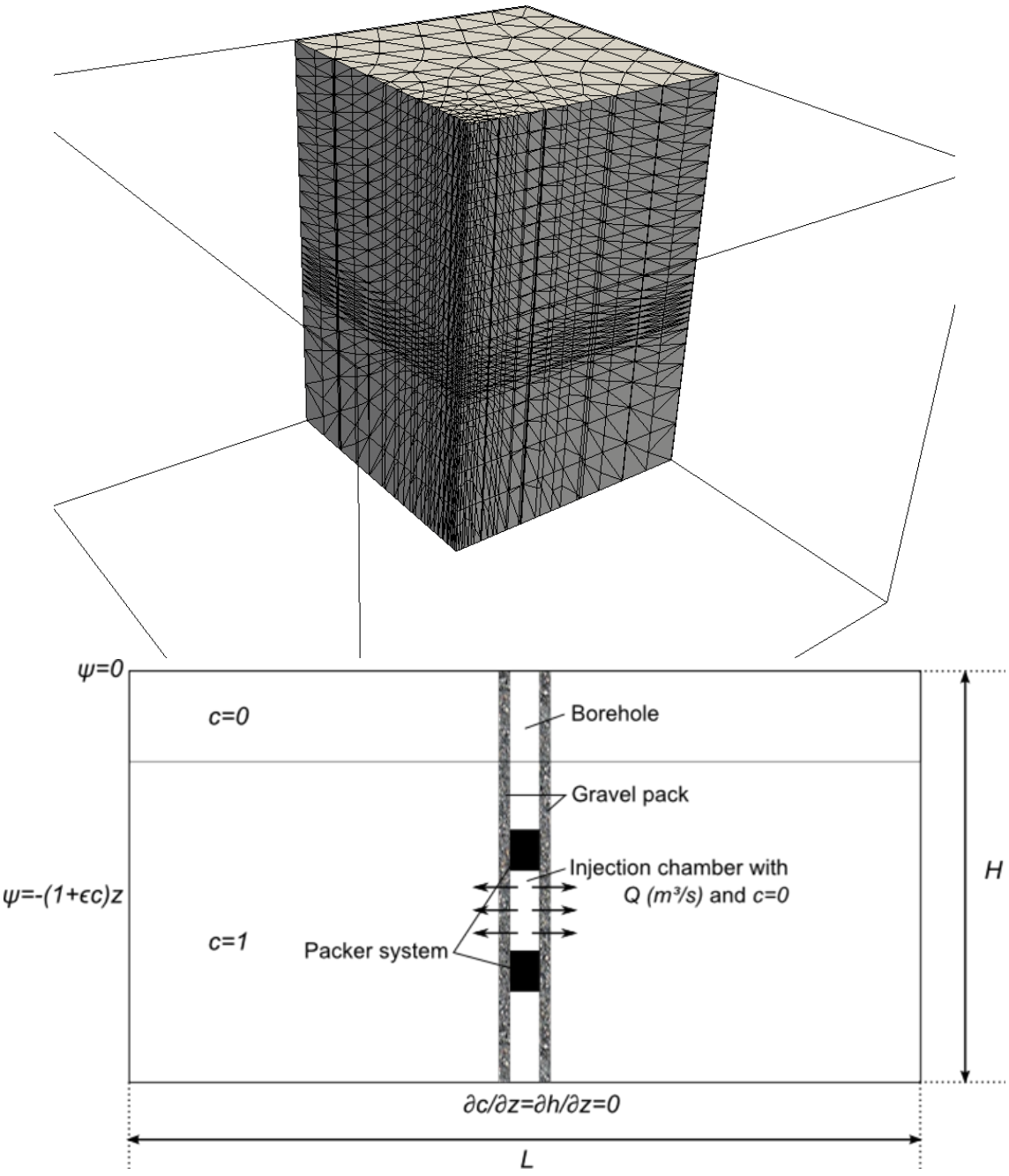

Figure 6.8: (a) 3D mesh with refinement in the central part and around injection layers and (b) conceptual model for the synthetic injection experiment.

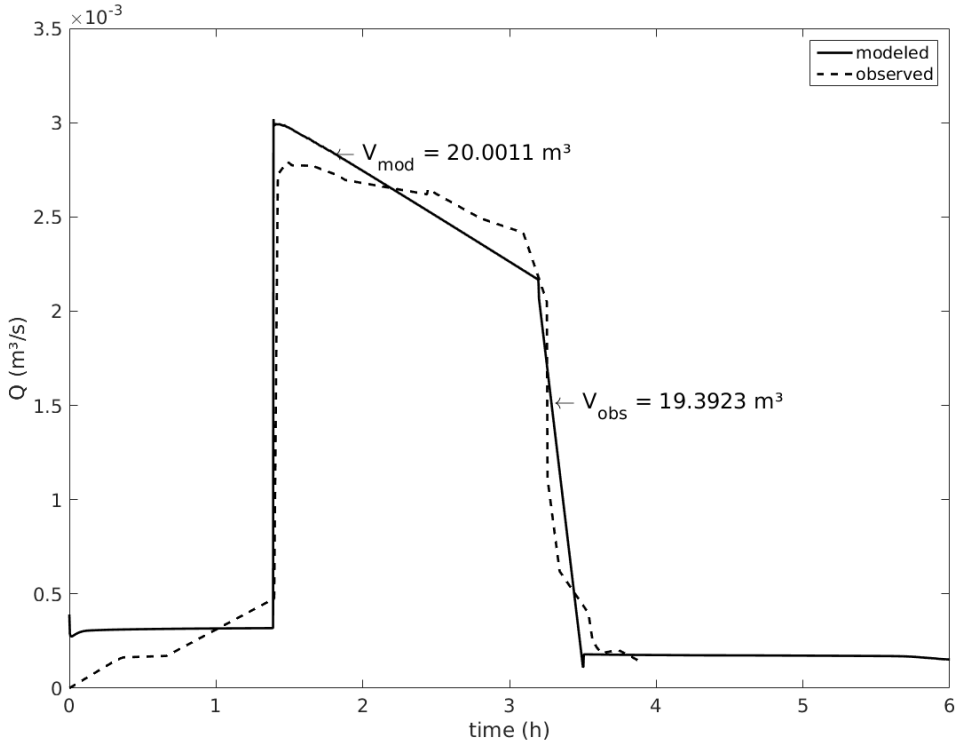

Figure 6.9: Injection rate of the experiment. The dashed line shows the observed injection in the field experiment (total volume of injected water 19.4 m^3) and the solid line shows the calibrated injection rate of the flow and transport model.

hydraulic conductivity than the surrounding aquifer material. The salt concentration was given as normalized concentration with a value of 1.0 for the saltwater and 0.0 for the injected freshwater. The initial conditions for the concentration in the aquifer were set to honor the transition zone observed in the borehole fluid conductivity log (Figure 6.2).

The conditions for the injection were set by giving the cells that represent the injection chamber (between 13 m and 14 m b.g.s.) a pressure head ψ 2 m higher (from 15 m to 16 m). To simulate the emptying of the tank, the pressure head decreases over time, calibrated after the measured injection rate in the field.

The immediate increase of the injection rate, observed in the field experiment, was modeled by a "de-clogging" effect of the material closely surrounding the injection chamber (i.e., representing the backfill material). This was done by increasing the hydraulic conductivity of the corresponding cells by about one order of magnitude after a corresponding time (i.e., about 5,000 s). The simulated and true injection rates are compared in Figure 6.9.

Dispersive processes play a minor role for the relatively short timescale of the experiment. In fact, several dispersivity values were tested and compared (modeling results not shown here); their influence is not significant over the short timescale considered here. Thus, only advective transport is studied.

To investigate the influence of heterogeneous hydraulic conductivity distributions in the aquifer, four different scenarios were simulated, including one homogeneous model and three different layered models, with a fine (clay-silt) layer between 10.5 m and 11.5 m depth (Table 6.2). The hydraulic conductivity values for the different scenarios were calibrated manually.

Table 6.2: Hydraulic conductivities of each layer for the four different scenarios.

	Scenario 1	Scenario 2	Scenario 3	Scenario 4
Upper layer	$5{\cdot}10^{-5}$ m s^{-1}	$5{\cdot}10^{-5}$ m s^{-1}	$1{\cdot}10^{-3}$ m s^{-1}	$1{\cdot}10^{-3}$ m s^{-1}
Middle layer	$5{\cdot}10^{-5}$ m s^{-1}	$1{\cdot}10^{-6}$ m s^{-1}		$1{\cdot}10^{-6}$ m s^{-1}
Bottom layer	$5{\cdot}10^{-5}$ m s^{-1}	$5{\cdot}10^{-5}$ m s^{-1}	$1{\cdot}10^{-5}$ m s^{-1}	$1{\cdot}10^{-5}$ m s^{-1}

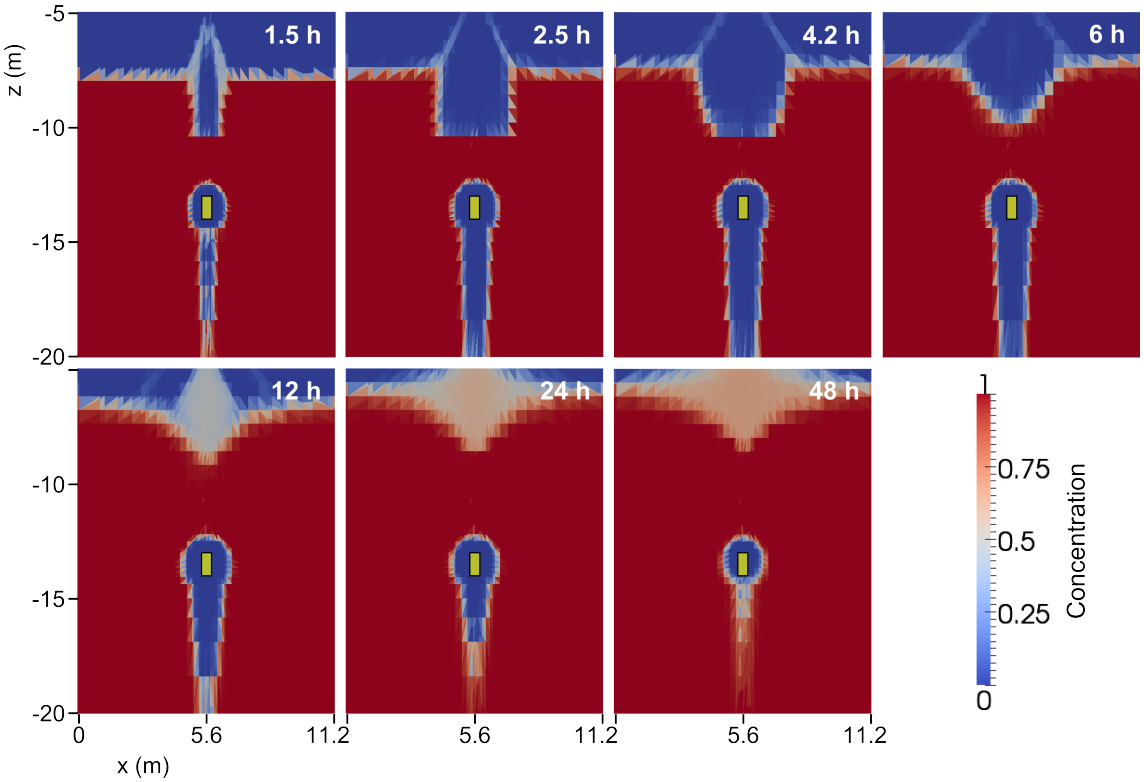

Figure 6.10: Flow and transport modeling results at different time steps (in hours after start of injection) for scenario 4 (see Table 6.2).

6.3.2 Simulation of ERT Monitoring

In order to compare, at least in a semi-quantitative manner, the observed ERT inversions with the results of the synthetic study, it is necessary to convert first the simulated normalized salt concentration from the flow-transport model into bulk electrical conductivity, for example through Archie's law relationship (Archie, 1942), here expressed for saturated sediments:

$$\sigma_b = \frac{\phi^m}{\mathrm{a}}\sigma_w, \tag{6.10}$$

where σ_b is the bulk electrical conductivity, a is a tortuosity factor, σ_w is the electrical conductivity of the fluid, and m is the cementation exponent. The formation factor $F = \mathrm{a}/\phi^m$ accounts for the pore space geometry. Due to the high salinity of the groundwater in the present case, surface conductivity is assumed to be negligible, and thus Archie's law is safely applicable. Since core data were available from one of the boreholes, it was possible to calibrate Archie's law in the laboratory with $F = 4.6$.

The next step is to simulate the field data that would be acquired given the simulated bulk electrical conductivity. For the 3D electrical forward modeling, we used the same approach as Manoli et al. (2015) and Rossi et al. (2015). The electric potential field, Φ, for a current injection between electrodes at $\boldsymbol{r}_{S+}$ (current source) and $\boldsymbol{r}_{S-}$ (current sink) is calculated by solving the Poisson equation

$$-\boldsymbol{\nabla} \cdot [\sigma_b \boldsymbol{\nabla} \Phi] = I[\delta(\boldsymbol{r} - \boldsymbol{r}_{S+}) - \delta(\boldsymbol{r} - \boldsymbol{r}_{S-})], \tag{6.11}$$

together with appropriate boundary conditions, where σ_b is the given electrical conductivity distribution, I is the injected current strength, and δ is the Dirac delta function. The mesh for the geoelectrical modeling includes the unsaturated zone, and the top boundary of the mesh (at $z = 0\,\mathrm{m}$) was set as a Neumann no-current boundary condition. For the lateral and bottom boundaries we used Dirichlet boundary conditions. Therefore, the mesh size was expanded in all directions with respect to the hydraulic mesh, so that the influence of the fixed voltage boundary conditions on the current lines was negligible.

The final step was to process and invert the synthetic ERT data in the same way as the field data.

6.3.3 Moment Analysis

In order to provide a more quantitative comparison between the field and synthetic experiments, we analyzed 2D moments as defined for example by Singha and Gorelick (2005):

$$M_{ij}(t) = \iint_{\Gamma} C(x, z, t) x^i z^j dx dz, \tag{6.12}$$

where M_{ij} is the spatial moment of order i, j between 0 and 2, x and z are the Cartesian coordinates, and dx and dz the pixel sizes. Γ is the integration domain of interest. The zeroth moment represents the total mass in the system while the vertical first moment, normalized with respect to mass, defines the center of mass in the z-direction. The second moments relate to the spread around the center of mass.

6.4 Results & Discussion

As a first step, let us consider the results of the synthetic study. Figure 6.10 shows the salt concentration of the flow and transport simulations for scenario 4, which

represents the most complex parameterization of the aquifer and is assumed to be most realistic for the test site (see the site stratigraphy reported in Figure 6.2). A general upward motion of the injected bulb is visible, with the highest velocities occurring within the injection hole. After some time, the freshwater starts to enter the aquifer along the entire borehole length. Although its density is much less than the density of the surrounding saltwater, the freshwater also moves downwards within the borehole, pushed by the pressure gradients. The 1.2 m thick fine material layer also plays a clear role in the bulb dynamics. This is expected. In correspondence to this layer, the flow only takes place along the borehole and the backfill material. Above the fine layer the plume expands laterally into the aquifer. Also the transition between the saltwater and the upper freshwater layer above 7.4 m depth moves entirely upwards since the overall movement in the model domain is upwards. One can also observe in the simulation results the tilting of the freshwater-saltwater interface in the lower part of the borehole as well as below the groundwater level, as described by Ward et al. (2007, 2008). The higher the ratio of hydraulic conductivity between the two layers, the stronger is the tilting, as predicted by Ward et al. (2008) (results not shown here).

Figure 6.11 shows the inverted images for four different subsurface scenarios at time 4.2 h after start of injection for the flow and transport simulations and the synthetic ERT monitoring (see Table 6.2 for definition of the scenarios). The figure clearly shows the dramatic influence of the hydraulic conductivity distribution on the shape of the freshwater bulb, both in the "real" images and in the corresponding inverted ERT images. Scenario 4, which includes the fine layer, is closest to the field results as already discussed above. However, scenario 3, with just two layers, shows a similar behavior in terms of plume development. In general, given the strong influence that hydraulic conductivity has on the results, it is conceptually possible to try and infer the site's hydraulic properties on the basis of the freshwater injection experiment. However, it is also apparent that calibrating *in detail* the true hydraulic conductivity distribution in the field experiment starting from the ERT images alone may be a very challenging task. In fact, while some main features are clearly identifiable, other smaller details may prove difficult to capture.

Indeed, the governing hydraulic effect comes from the different conductivities of the upper and lower parts of the aquifer (scenarios 1 + 2 vs. 3 + 4), and the fine layer does not play such an important role as expected a priori. From the simulation results it is difficult to say whether scenario 3 or scenario 4 is closest to reality. However, for scenarios 1 and 2 ERT clearly overestimates the extent of the freshwater plume, whereas for scenarios 3 and 4 the plume extension is reconstructed quite well, in particular in the deeper region (Figure 6.10).

It is instructive to examine in detail (Figure 6.12) the similarities and differences between the ERT field data and the reconstructed ERT images from the simulation scenario that visually appears better than the others (scenario 4). The simulated ERT images show the same general behavior in response to the injection process and associated plume development as the ERT field results. In the field ERT images the freshwater body disappears much faster. After 24 h, although in the field ERT images the freshwater bulb is hardly visible, the simulation still shows its presence. It should be noted that in the simulations the boundary condition at the well is

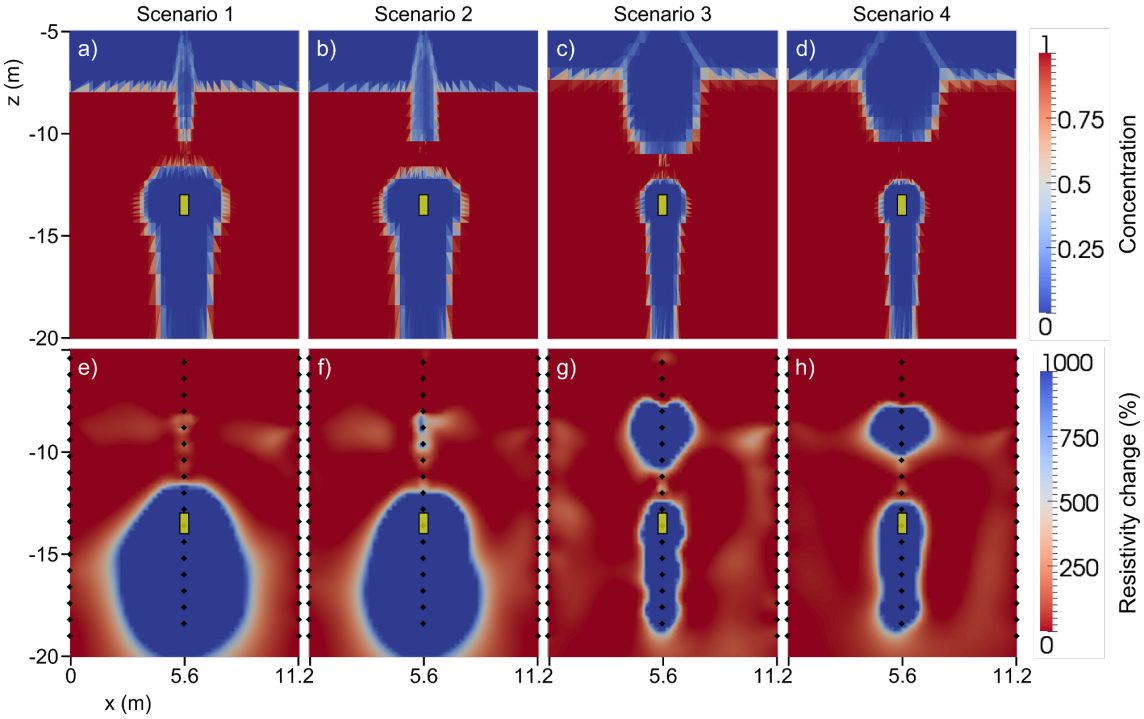

Figure 6.11: Comparison of simulation results for different hydraulic conductivity parameterizations at time 4.2 h after start of injection. The top panel shows the flow and transport modeling results, the bottom panel the corresponding simulated ERT results; (a) and (e) homogeneous model, (b) and (f) fine layer within homogeneous model, (c) and (g) two-layered system, and (d) and (h) two-layered system including fine layer at interface.

imposed as Dirichlet (head) condition, so flux is computed depending on the applied head. We applied the head as actually measured in the injection tank. Consequently, the flow is never zero, not even at the end of the experiment. On the other hand, the tilting of the freshwater-saltwater interface as seen in the flow and transport model results is much less visible in the ERT images.

The imaged resistivity changes in the field experiment show less contrast than in the synthetic study. The salinity difference between the freshwater and the saltwater is very large and thus so is the NaCl concentration. Within this range, the electrical conductivity of the water might no longer follow a linear relation with concentration (e.g., Wagner et al., 2013), while here it is assumed to be linear. This can lead to a shifting in the contrast when the concentration is converted into electrical conductivity.

Note also that the gradual change of electrical conductivity in the transition zone (i.e., between 5 m and 7.4 m depth) is not visible in the ERT images (Figure 6.11). In the transport simulations it can be seen that this zone also moves upwards in the aquifer and becomes thinner (Figure 6.10).

Another difference between the field and the synthetic ERT results is the sharpness of the freshwater body: the boundaries appear smoother in the field study. Although dispersion effects were not further investigated in this study, a higher value of α_L

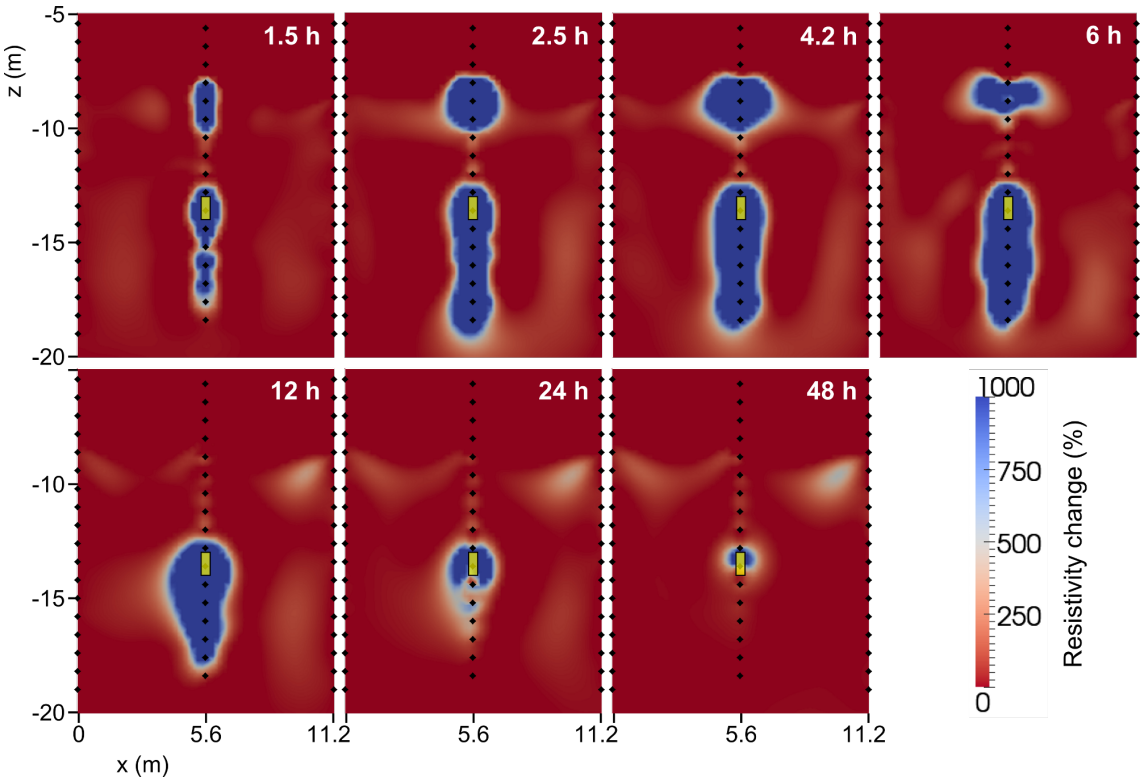

Figure 6.12: Results of synthetic ERT experiment for selected time steps (in hours after start of injection) for scenario 4 (see Table 6.2). Black diamonds denote the position of electrodes.

and α_T in the simulations would obviously lead to a smoother gradient across the plume boundaries. On the other hand, in the field results this may also be partly explained by the fact that one ERT measurement frame took about 40 minutes, and since the overall plume migration was relatively fast, the process is to some degree smeared in the inverted images.

Figure 6.13 shows the spatial moments (0^{th} moment: total mass; 1^{st} moment: center of mass) of the freshwater bulb for the field and synthetic ERT inversion results, as well as the "true" moments from the flow and transport model (see Section 6.3.3). The total mass is well recovered by the synthetic ERT results (using backwards the same Archie's law parameterization used in the forward modeling). However, the field ERT underestimates the total mass. While this is a known characteristic of moment analysis applied to ERT data for tracer tests (e.g., Singha and Gorelick, 2005), in this specific case it looks likely that the chosen Archie's law parameters are not fully adequate to represent the electrical conductivity-salinity relationship. Considering that even linearity of Ohm's law is questionable at the high salt concentrations observed at the site, one could also question the overall validity of Archie's law. Note that all other factors normally contributing to bad ERT mass recovery under field conditions are the same in the synthetic and the true case, and thus cannot be called into play.

In contrast to the total mass, the vertical center of mass is, despite some early oscillations, well recovered also for the field data. This, however, is known to be a

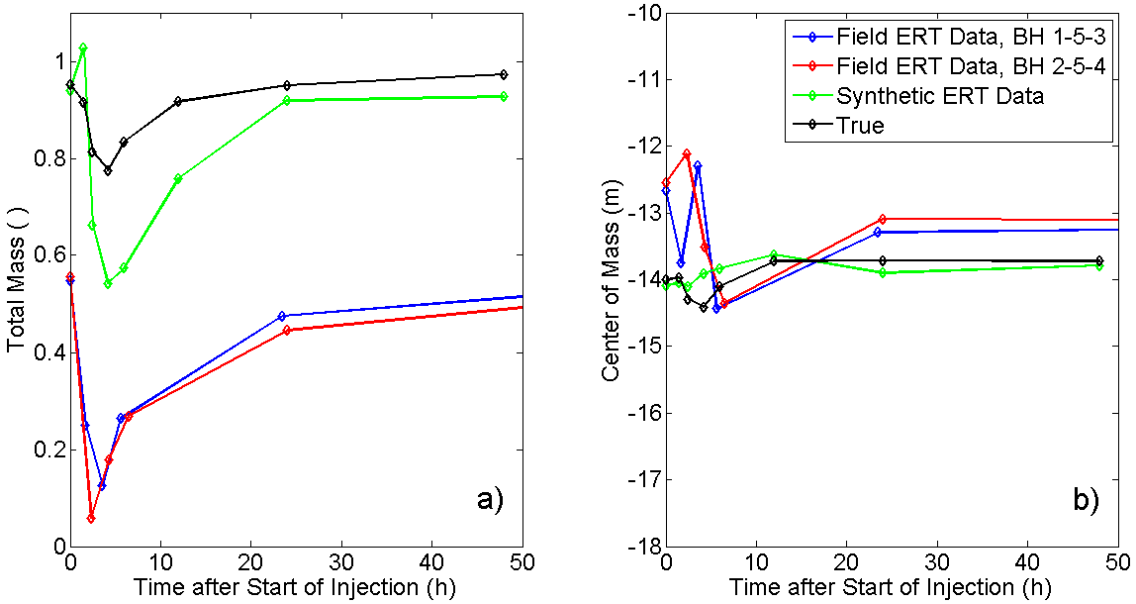

Figure 6.13: Spatial moments for the field ERT data, synthetic ERT data, and the true data from the flow and transport model. The moments for the true field were calculated in 3D while those for the ERT tomograms were calculated in 2D. The field ERT data are separated into the two borehole planes. (a) shows the total mass in the system, normalized, and (b) is the center of mass in the vertical direction.

very robust indicator (e.g., Binley et al., 2002a; Deiana et al., 2007, 2008).

Overall, and in spite of the differences described above, the comparison between observed and modeled ERT images is satisfactory, particularly in the face of uncertainties concerning the heterogeneities of the real system that could not be investigated in extreme detail. In addition, we cannot exclude the possibility that the linearity of the current flow equation may be violated in such a highly conductive environment, thus leading to inconsistencies between field reality and theoretical assumptions.

Despite the above limitations, the comparison shows that ERT imaging is a viable tool for monitoring freshwater injection in a hyper-saline aquifer. This, by itself, was not an obvious result. The ERT dataset was collected under extreme, challenging conditions. Even so, the ERT data are of fairly good quality considering that we retained only data that passed a fairly strict reciprocity check, knowing that larger reciprocity errors are likely to be related to nonlinear current effects occurring in such high electrical conductivity environments. The study also indicates how an accurate coupled model can mimic in an effective manner the behavior of the observed freshwater bulb that was injected into the domain, and this too was not self-evident.

6.5 Conclusions

In this paper we present a hydro-geophysical approach that can be used to study freshwater injections in saline aquifers. In particular the approach is used to monitor and describe a freshwater injection experiment conducted in a hyper-saline aquifer in

the Molentargius Saline Regional Park in the south of Sardinia (Italy). The experiment was monitored using time-lapse ERT in five boreholes. A numerical study of the experiment (density-dependent flow and transport modeling in conjunction with ERT simulations) was carried out to investigate the plume migration dynamics and the influence of different hydraulic conductivity parameterizations. The numerical algorithm of the coupled flow and transport model proved to be stable and accurate despite the challenging conditions.

The results demonstrate the feasibility and benefit of using a combination of (a) time-lapse cross-borehole ERT and (b) numerical modeling of coupled flow and transport to predict the same ERT results. The comparison between measured and simulated ERT images was used as the key diagnostics aimed at estimating the system's governing parameters and consequently describing the saltwater-freshwater dynamics. More sophisticated data assimilation techniques can be used to further refine the presented approach in future work. We can conclude from the present study the following:

a) The complex dynamics of hyper-saline-freshwater systems can be tracked using high-resolution spatially extensive time-lapse non-invasive monitoring. On the contrary, traditional monitoring techniques alone (e.g., conductivity logs, as in Figure 6.3) give only a very partial image, largely inconclusive to understand the system dynamics.

b) Numerical modeling of these coupled systems is very challenging due to the presence of strong density/viscosity contrasts and large hydraulic conductivity heterogeneities. The latter, in particular, largely control the dynamics of the saltwater-freshwater interaction. In absence of a robust numerical model, it is impossible to estimate the impact of hydraulic heterogeneity on this dynamics.

c) A detailed comparison between field data (here, ERT time-lapse images) and modeled data of the same type enables a better understanding of the behavior of a freshwater bulb injected into a hyper-saline environment.

Our study also serves to highlight some of the weaknesses that should be addressed in future work:

- Fine-tuning of geophysical constitutive relationships, hydraulic and transport parameters, and system heterogeneities needs to be improved. We managed to bring the match between field and synthetic data to an acceptable level with relatively small effort, but it is very difficult to improve the match further. For instance, in the case presented here the injected freshwater bulb "disappears" from the real ERT images faster than in the simulation results. Also, the mass balance is honored easily in the simulations, whereas in the real data lack of mass is apparent. All of this points towards a number of aspects that could be improved in the data matching. However, the target parameters to be modified for this improvement are not easy to identify, given their very high number and complex nature. Among these, there are hydraulic parameters and dispersivities, and their spatial heterogeneities, as well as also Archie's

law parameters. This task is likely to be challenging even in a rigorous data assimilation framework, and equifinality of model parameterizations is likely.

- The extreme hyper-saline system considered here is likely to exceed the limits of linear relationships between current and voltage (Ohm's law) as well as between electrical conductivity and salinity. Therefore, a full nonlinear analysis should be conducted, particularly concerning the electrical behavior of the system. In absence of this, we have to limit ourselves to a semi-quantitative interpretation, as shown here.

Finally, with regards to practical aspects of freshwater injection and monitoring in saline aquifers, we can draw the following conclusions:

- Although in typical ASR applications the contrasts of density and salinity are usually smaller, this study shows that time-lapse ERT is a powerful monitoring tool for this (and also other) types of hyper-saline applications. ERT can provide spatial information that is unattainable using traditional monitoring techniques (e.g., in boreholes).
- The movement and mixing of the freshwater plume can be very fast; thus, any ERT monitoring must adopt configurations for quick measurements (e.g., in the conditions represented in this study an acquisition time of less than 30 minutes is recommended).
- In hyper-saline systems, measuring reciprocity may not be the ideal error indicator since nonlinear phenomena may be triggered, or during the time between the normal and reciprocal measurement the system may have already changed, thus invalidating the reciprocity check.

The example shown in this paper shows how the joint use of ERT imaging and gravity-dependent flow and transport modeling give fundamental information for this type of study.

Acknowledgements

This research was supported by the Basic Research Project L.R. 7/2007 (CRP2_686, Gian Piero Deidda) funded by the Regione Autonoma della Sardegna (Italy) and the EU FP7 project GLOBAQUA ("Managing the effects of multiple stressors on aquatic ecosystems under water scarcity"). We thank the Parco Naturale Molentargius-Saline for allowing us to set up a test site in the park. We also thank the field crew from the University of Cagliari (namely Luigi Noli and Mario Sitzia) as well as Marco Mura, Enzo Battaglia and Francesco Schirru for their work in the field. Special thanks go to Damiano Pasetto and Gabriele Manoli for their support regarding the 3D ERT forward modeling code and Annamaria Mazzia for assistance concerning the numerical experiments. The data can be obtained from the authors upon request.

Chapter 7

Conclusions & Perspectives

7.1 Conclusions

This thesis deals with the application of geophysical investigation techniques for the characterization and monitoring of different types of managed aquifer recharge. A focus lies on (time-lapse) electrical resistivity tomography. MAR, where water resources are stored under controlled conditions in aquifers for storage, purification and reclamation, is a sustainable technology in modern water resources management and receives increasing attention, especially in regions with water scarcity.

A major advantage of the geophysical methods is their tomographic character without invasive disturbances of the subsurface. Furthermore, they are mostly easy to use, fast and cheap in application. However, since the geophysical methods often do not deliver distinct data, the interpretation of results can sometimes be misleading and the raw measurement data need further and intense treatment. The combination of different geophysical methods together with selected "classical" hydro-geological measurements can be a promising and powerful approach for hydrogeological investigations, like for MAR. This was shown in the present thesis.

Four case studies (synthetic and field studies) of different MAR types in different regions of the world were presented throughout this thesis. The first study (Chapter 3) was a short numerical feasibility study showing the potential of time-lapse ERT to monitor controlled water infiltration experiments and to quantify the infiltrated water volume. The comparison between the true (modeled) data and the time-lapse ERT derived data by setting the results in relation and calculate a recovery rate shows that ERT is able to quantify the water volumes with little underestimation. The study also shows that different designs of electrode distribution (on the surface and in boreholes with different distances between boreholes) have, of course, large impact on the recovery rate.

The second study (Chapter 4) dealt with the ability of geoelectrical and seismic methods to characterize the geology and hydrogeology of an alluvial basin in the arid region of the Lower Jordan River Valley (West Bank) to be suitable for subsurface water storage. The geophysical methods were used to delineate the basin geometry, the border of the alluvial sediments to the underlying chalk aquiclude and, in combination with hydrogeological approaches, characterize hydraulic parameters

of the alluvial sediments. Recommendations for the subsurface storage of runoff water within the concept of MAR were given.

The third study (Chapter 5) investigated the dynamic process of water infiltration using on-line geoelectrical monitoring at an SAT site in the coastal area south of Tel Aviv (Israel). It shows that ERT is able to detect the moving water body even under very high fluxes. To date, there is probably no published study that applied time-lapse ERT with such a temporal density for a couple of weeks (hourly measurements) at this scale of water infiltration. New is also the presented approach of aquifer zonation based on the temporal and spatial variability of the electrical conductivity, induced by the variations of water content. The study also showed that already the apparent electrical conductivity data contained valuable information on the vadose zone state during infiltration.

For the fourth study (Chapter 6), an experiment of freshwater injection into a hypersaline aquifer was monitored with geoelectrics via boreholes at a site near Cagliari (Sardinia, Italy). The experiment happened very quick, the freshwater body completely disappeared already one day after start of injection. Nevertheless, time-lapse ERT was also here able to detect the moving freshwater body within the very saline groundwater since the electrical conductivity is dependent on the salinity of the fluid. An extensive numerical study of the injection experiment was conducted, including density-dependent flow and transport simulations within a fine defined model domain containing the injection borehole as a preferential flow path. Forward simulations of geoelectrical measurements were conducted, after the salinity concentrations were converted into electrical properties using a petrophysical model after Archie. The experiment demonstrates that the evolution of the freshwater bulb is not only influenced by the density-contrast but also by the system's (even mild) hydraulic heterogeneities. By the way, the results show that such an extreme environment would fail for aquifer storage and recovery. However, this result was kind of obvious.

All four studies show that time-lapse ERT is able to track infiltrated or injected water under very different conditions and even under very high fluxes. It is able to detect water bodies with different salt concentrations. Furthermore, the spatial distribution of the dynamic behavior of the electrical conductivity, caused by changes in water saturation, can be used to define and even quantify hydraulic parameters which then can be used for instance for flow models. A main concern in MAR investigations is that the subsurface hydraulic characteristics are often very heterogeneous. This is challenging to be measured by conventional hydro-geological approaches. The thesis shows that time-lapse ERT is able to overcome the problem of delineating the heterogeneous subsurface.

Some of this is not completely "new" in the hydrogeophysics community. However, in the context of MAR the here presented approaches have not or only barely been applied yet (see Chapter 1) and they may help in the design and application of new as well as existing sites for MAR. And as MAR is a promising technique in sustainable and innovative water resources management for the future, especially in arid and semi-arid regions, the geophysical investigation techniques may play an important role for the pre-investigations, planning, implementation, and operation of MAR systems since they are cheap, easy to apply and non- to minimally-invasive.

7.2 Perspectives

The here presented thesis contains four different case studies on the use of geophysics for MAR. Since beside this study only a few other studies on this subject exist (Chapter 1), further work is still required. Especially on the real use, the application side, which is the most interesting part for the stakeholders (like companies and authorities), the geophysics has to make its way to get more popular. For sure, an ERT monitoring system that was installed at the Shafdan site in Israel (Chapter 5) would not be applicable for the local water company to be installed in every pond. However, a four-point electrode array would be a cheap and easy installation and can still give an insight into the vadose zone state, even at depths where for instance TDT sensors would be very difficult to be installed.

Geophysical field campaigns conducted prior to the implementation of MAR systems can, depending on the situation at hand, give fast and cheap insight into the subsurface. This makes the geophysics a promising alternative with the implication to reduce the number of required exploration boreholes as was shown with the seismic and geoelectrical surveys in the study in Chapter 4.

As already mentioned in Chapter 2, a major concern of MAR systems, especially occurring for spreading basins, is clogging. Fine material, suspended in the flowing fluid, can rapidly clog the basin surface and shallow layers of the subsurface material which strongly decreases the infiltration rate and thus, the efficiency of the pond. This aspect was not addressed in this thesis. As an outlook regarding geophysical monitoring techniques, the method of (spectral) induced polarization ((S)IP) could be a useful tool to be applied for monitoring of the accumulation of fine material. This is due to the fact that the grains in porous media cause a polarization effect at the grain-fluid-interface which can be measured via geoelectrical methods in the time- or frequency-domain. And clay minerals cause an even higher polarization effect. For example, for a new developed infiltration basin, the monitoring of the accumulation of fine material via SIP could provide an early warning system, even spatially, before the infiltration rate decreases below a certain degree.

The new developed approach for subsurface zonation (see Chapter 5) is very promising for the hydraulic characterization of the heterogeneous subsurface and may therefore also have an impact in other fields of hydrology. However, it still needs more investigation, for instance via numerical studies (as discussed in Section 5.3.3). A numerical modeling study as it was undertaken in the synthetic study in Chapter 3, could be conducted to analyze this phenomenon and to get a better understanding of the parameters of the fitting function (Equation 5.5). To start with a homogeneous aquifer and increase the complexity to, e.g., a two-layered system, a homogeneous system with a thin, fine layer and a heterogeneous system (as in Figure 3.1) could be a procedure to understand the cumulative behavior and thus, the role of τ in Equation 5.5.

Further development takes place in the area of coupled inversion, i.e., to invert the measured geophysical data directly for hydrologic parameters. Here, MAR applications will definitely benefit from new approaches and coupled inversion procedures. And additionally, a combination with optimization approaches, as presented in the study of Drumheller et al. (2017) (see Appendix 5.B in Chapter 5), are thinkable.

Bibliography

Alaghmand, S., Beecham, S., Woods, J. A., Holland, K. L., Jolly, I. D., Hassanli, A., and Nouri, H. 2015. Injection of fresh river water into a saline floodplain aquifer as a salt interception measure in a semi-arid environment. *Ecological Engineering* 75:308–322, doi:10.1016/j.ecoleng.2014.11.014.

Alumbaugh, D. L. and Newman, G. A. 2000. Image appraisal for 2-D and 3-D electromagnetic inversion. *Geophysics* 65:1455–1467.

Anger, S. 2014. Synthetic study of infiltration processes relating to managed aquifer recharge. BSc Thesis, Rheinische Friedrich-Wilhelms-Universität Bonn, Germany.

Annan, A. P. 2005. GPR methods for hydrogeological studies, pp. 185–213. *In* Y. Rubin and S. S. Hubbard (eds.), Hydrogeophysics, volume 50 of *Water Science and Technology Library*, chapter 7. Springer.

Archie, G. E. 1942. The electrical resistivity log as an aid in determining some reservoir characteristics. *Transactions of the American Institute of Mining, Metallurgical and Petroleum Engineers* 146:54–62, doi:10.2118/942054–G.

Asano, T. 1985. Artificial recharge to groundwater. Butterworth, Boston.

Bear, J. and Jacobs, M. 1965. On the movement of water bodies injected into aquifers. *Journal of Hydrology* 3:37–57.

Begin, Z. 1974. The geological map of Israel - 1:50.000 - Sheet 9-III: Jericho, explanatory notes. Geological Survey of Israel, Jerusalem.

Begin, Z., Ehrlich, A., and Nathan, Y. 1974. Lake Lisan, the Pleistocene precursor of the Dead Sea. Geological Survey of Israel Bulletin, 63, 30 pp.

Binley, A., Cassiani, G., Middleton, R., and Winship, P. 2002a. Vadose zone flow model parameterisation using cross-borehole radar and resistivity imaging. *Journal of Hydrology* 267:147–159.

Binley, A., Hubbard, S. S., Huismann, J. A., Revil, A., Robinson, A., Singha, K., and Slater, L. 2015. The emergence of hydrogeophysics for improved understanding of subsurface processes over multiple scales. *Water Resources Research* 51:3837–3866, doi:10.1002/2015WR017016.

Binley, A. and Kemna, A. 2005. DC resistivity and induced polarization methods, pp. 129–156. *In* Y. Rubin and S. S. Hubbard (eds.), Hydrogeophysics, volume 50 of *Water Science and Technology Library*, chapter 5. Springer.

Binley, A., Ramirez, A., and Daily, W. 1995. Regularised image reconstruction of noisy electrical resistance tomography data, pp. 401–410. *In* M. Beck, B. Hoyle, M. Morris, R. Waterfall, and R. Williams (eds.), Process Tomography - 1995, volume 6-8 April 1995 of *Bergen*. Proceedings of the 4th Workshop of the European Concerted Action on Process Tomography.

Binley, A., Winship, P., West, L. J., Pokar, M., and Middleton, R. 2002b. Seasonal variation of moisture content in unsaturated sandstone inferred from borehole radar and resistivity profiles. *Journal of Hydrology* 267:160–172.

Bouwer, H. 2002. Artificial recharge of groundwater: hydrogeology and engineering. *Hydrogeology Journal* 10:121–142, doi:10.1007/s10040–001–0182–4.

Browne, D., Deletic, A., Mudd, G. M., and Flechter, T. D. 2008. A new saturated/unsaturated model for stormwater infiltration systems. *Hydrological Processes* 22:4838–4849, doi:10.1002/hyp.7100.

Cassiani, G., Bruno, V., Villa, A., Fusi, N., and Binley, A. 2006. A saline tracer test monitored via time-lapse surface electrical resistivity tomography. *Journal of Applied Geophysics* 59:244–259, doi:10.1016/j.jappgeo.2005.10.007.

Coltorti, M., Melis, E., and Patta, D. 2010. Geomorphology, stratigraphy and facies analysis of some Late Pleistocene and Holocene key deposits along the coast of Sardinia (Italy). *Quaternary International* 222:19–35, doi:10.1016/j.quaint.2009.10.006.

Daily, W., Ramirez, A. L., Binley, A., and LaBrecque, D. J. 2004. Electrical resistance tomography. *The Leading Edge* 23:438–442, doi:10.1190/1.1729225.

Daily, W., Ramirez, A. L., LaBrecque, D. J., and Nitao, J. 1992. Electrical resistivity tomography of vadose zone water movement. *Water Resources Research* 28:1429–1442, doi:10.1029/91WR03087.

Davis, J. L. and Annan, A. P. 1989. Ground penetrating radar for high-resolution mapping of soil and rock stratigraphy. *Geophysical Prospecting* 37:531–551.

Davis, K., Li, Y., and Batzle, M. 2008. Time-lapse gravity monitoring: A systematic 4D approach with application to aquifer storage and recovery. *Geophysics* 73:WA61–WA69, doi:10.1190/1.2987376.

Deiana, R., Cassiani, G., Kemna, A., Villa, A., Bruno, V., and Bagliani, A. 2007. An experiment of non-invasive characterization of the vadose zone via water injection and cross-hole time-lapse geophysical monitoring. *Near Surface Geophysics* 5:183–194, doi:10.3997/1873–0604.2006030.

Deiana, R., Cassiani, G., Villa, A., Bagliani, A., and Bruno, V. 2008. Calibration of a vadose zone model using water injection monitored by GPR and Electrical Resistance Tomography. *Vadose Zone Journal* 7:215–226, doi:10.2136/vzj2006.0137.

Dentoni, M., Deidda, R., Paniconi, C., Qahman, K., and Lecca, G. 2015. A simulation/optimization study to assess seawater intrusion management strategies for the Gaza Strip coastal aquifer (Palestine). *Hydrogeology Journal* 23:249–264, doi:10.1007/s10040–014–1214–1.

Diersch, H.-J. G. and Kolditz, O. 2002. Variable-density flow and transport in porous media: approaches and challanges. *Advances in Water Resources* 25:899–944.

Dillon, P. J. 2005. Future management of aquifer recharge. *Hydrogeology Journal* 13:313–316, doi:10.1007/s10040–004–0413–6.

Dillon, P. J., Pavelic, P., Page, D., Beringen, H., and Ward, J. D. 2009. Managed aquifer recharge: An introduction. Technical report, Waterlines Report Series No. 13, National Water Commission, Canberra, Australia.

Dillon, P. J., Pavelic, P., Toze, S., Rinck-Pfeiffer, S., Martin, R., Knapton, A., and Pidsley, D. 2006. Role of aquifer storage in water reuse. *Desalination* 188:123–134, doi:10.1016/j.desal.2005.04.109.

Doetsch, J., Linde, N., and Binley, A. 2010a. Structural joint inversion of time-lapse crosshole ERT and GPR traveltime data. *Geophysical Research Letters* 37:L24404, doi:10.1029/2010gl045482.

Doetsch, J., Linde, N., Coscia, I., Greenhalgh, S., and Green, A. G. 2010b. Zonation for 3D aquifer characterization based on joint inverions of multimethod crosshole geophysical data. *Geophysics* 75:G53–G64, doi:10.1190/1.3496476.

Doetsch, J., Linde, N., Pessognelli, M., Green, A. G., and Günther, T. 2012a. Constraining 3-D electrical resistance tomography with GPR reflection data for improved aquifer characterization. *Journal of Applied Geophysics* 78:68–76, doi:10.1016/j.jappgeo.2011.04.008.

Doetsch, J., Linde, N., Vogt, T., Binley, A., and Green, A. G. 2012b. Imaging and quantifying salt-tracer transport in a riparian groundwater system by means of 3D ERT monitoring. *Geophysics* 77:207–218, doi:10.1190/GEO2012–0046.1.

Drumheller, Z., Smits, K. M., Illangasekare, T. H., Regnery, J., Lee, J., and Kitanidis, P. K. 2017. Optimal decision making algorithm for managed aquifer recharge and recovery operation using near real-time data: Benchtop scale laboratory demonstration. *Groundwater Monitoring & Remediation,* doi:10.1111/gwmr.12198.

Esmail, O. J. and Kimbler, O. K. 1967. Investigation of the technical feasibility of storing fresh water in saline aquifers. *Water Resources Research* 3:683–695.

EWRI/ASCE 2001. Standard guidelines for artificial recharge of ground water. Environmental and Water Resources Institute, American Society of Civil Engineers, Reston, Virginia, 34-01.

Farber, E., Vengosh, A., Gavrieli, I., Marie, A., Bullen, T. D., Mayer, B., Holtzman, R., Segal, M., and Shavit, U. 2004. The origin and mechanisms of salinization of the Lower Jordan River. *Geochimica et Cosmochimica Acta* 68:1989–2006, doi:10.1016/j.gca.2003.09.021.

Faust, L. Y. 1953. A velocity function including lithologic variation. *Geophysics* 18:271–288.

Finsterle, S. 2007. iTOUGH2 user's guide. LBNL-40040, Lawrence Berkeley National Laboratory, Berkeley, CA.

Finsterle, S., Doughty, C., Kowalsky, M. B., Moridis, G. J., Pan, L., Xu, T., Zhang, Y., and Pruess, K. 2008. Advanced vadose zone simulations using TOUGH. *Vadose Zone Journal* 7:601–609, doi:10.2136/vzj2007.0059.

Finsterle, S. and Kowalsky, M. B. 2008. Joint hydrological-geophysical inversion for soil structure identification. *Vadose Zone Journal* 7:287–293, doi:10.2136/vzj2006.0078.

Flint, A. L. and Ellet, K. M. 2004. The role of unsaturated zone in artificial recharge at San Gorgonio Pass, California. *Vadose Zone Journal* 3:763–774.

Gale, I. 2005. Strategies for managed aquifer recharge (MAR) in semi-arid areas. UNESCO-IHP, Paris.

Gambolati, G., Putti, M., and Paniconi, C. 1999. Three-dimensional model of coupled density dependent flow and miscible salt transport, pp. 315–362. *In* J. Bear, A. H.-D. Cheng, S. Sorek, D. Ouazar, and I. Herrera (eds.), Seawater Intrusion in Coastal Aquifers - Concepts, Methods and Practices. Kluwer Academic Publishers, Dordrecht, The Netherlands.

Goldman, M. and Kafri, U. 2006. Hydrogeophysical applications in coastal aquifers, pp. 233–254. *In* H. Vereecken, A. Binley, G. Cassiani, A. Revil, and K. Titov (eds.), Applied Hydrogeophysics. Springer.

Hayley, K., Bentley, L. R., and Gharibi, M. 2009. Time-lapse electrical resistivity monitoring of salt-affected soil and groundwater. *Water Resources Research* 45:W07425, doi:10.1029/2008WR007616.

Hayley, K., Bentley, L. R., Gharibi, M., and Nightingale, M. 2007. Low temperature dependence of electrical resistivity: Implications for near surface geophysical monitoring. *Geophysical Research Letters* 34:L18402.

Hermans, T., Nguyen, F., and Caers, J. 2015. Uncertainty in training image-based inversion of hydraulic head data constrained to ERT data: workflow and case study. *Water Resources Research* 51:5332–5352, doi:10.1002/2014WR016460.

Hötzl, H., Möller, P., and Rosenthal, E. 2009. The Water of the Jordan Valley - Scarcity and deterioration of groundwater and its impact on the regional development. Spinger-Verlag, Berlin Heidelberg.

Icekson-Tal, N., Michail, M., Kraitzer, R., Elkayam, R., Sherer, D., and Shoham, G. 2012. Groundwater recharge with municipal effluent. Technical report, Mekorot Report, Dan Region Reclamation Project, Mekorot Water Company LTD.

Idelovitch, E., Icekson-Tal, N., Avraham, O., and Michail, M. 2003. The long-term performance of soil aquifer treatment (SAT) for effluent reuse. *Water Science and Technology: Water Supply* 3:239–246.

Kallioras, A., Pliakas, F., and Diamantis, I. 2010. Simulation of groundwater flow in a sedimentary aquifer system subjected to overexploitation. *Water Air Soil Pollution* 211:177–201, doi:10.1007/s11270–009–0291–6.

Kemna, A. 2000. Tomographic inversion of complex resistivity - Theory and application. PhD Thesis, Bochum Ruhr-University, Bochum, Germany.

Kemna, A., Binley, A., Day-Lewis, F., Englert, A., Tezkan, B., Vanderborght, J., Vereecken, H., and Winship, P. 2006. Solute transport processes, pp. 117–160. *In* H. Vereecken, A. Binley, G. Cassiani, A. Revil, and K. Titov (eds.), Applied Hydrogeophysics, volume 71 of *IV: Earth and Environmental Sciences*. Springer, Dordrecht.

Kemna, A., Binley, A., and Slater, L. 2004. Crosshole IP imaging for engineering and environmental applications. *Geophysics* 69:97–107.

Kemna, A., Vanderborght, J., Kulessa, B., and Vereecken, H. 2002. Imaging and characterisation of subsurface solute transport using electrical resistivity tomography (ERT) and equivalent transport models. *Journal of Hydrology* 267:125–146.

Ketabchi, H., Mahmoodzadeh, D., Ataie-Ashtiani, B., and Simmons, C. T. 2016. Sea-level rise impacts on seawater intrusion in coastal aquifers: review and integration. *Journal of Hydrology* 535:235–255, doi:10.1016/j.jhydrol.2016.01.083.

Kimbler, O. K., Kazmann, R. G., and Whitehead, W. R. 1975. Cyclic storage of fresh water in saline aquifers. Louisiana Water Resour. Res. Inst. Bulletin 10, Baton Rouge, L.A.

Klinger, J., Goldscheider, N., and Hötzl, H. 2015. SMART - IWRM - Sustainable Management of Available Water Resources with Innovative Technologies - Integrated Water Resources Management in the Lower Jordan Rift Valley: Final Report Phase II. Report, KIT Scientific Reports 7698, doi:10.5445/KSP/1000047307, Karlsruhe.

Knödel, K., Lange, G., and Voigt, H.-J. 2007. Environmental Geology - Handbook of Field Methods and Case Studies. Federal Institute for Geosciences and Natural Resources, Springer Berlin Heidelberg.

Koestel, J., Kemna, A., Javaux, M., Binley, A., and Vereecken, H. 2008. Quantitative imaging of solute transport in an unsaturated and undisturbed soil monolith with 3-D ERT and TDR. *Water Resources Research* 44:W12411, doi:10.1029/2007WR006755.

Koestel, J., Vanderborght, J., Javaux, M., Kemna, A., Binley, A., and Vereecken, H. 2009a. Noninvasive 3-D transport characterization in a sandy soil using ERT: 1. Investigating tha validity of ERT-derived transport parameters. *Vadose Zone Journal* 8:711–722, doi:10.2136/vzj2008.0027.

Koestel, J., Vanderborght, J., Javaux, M., Kemna, A., Binley, A., and Vereecken, H. 2009b. Noninvasive 3-D transport characterization in a sandy soil using ERT: 2. transport process inference. *Vadose Zone Journal* 8:723–734, doi:10.2136/vzj2008.0154.

Kumar, B. and Kimbler, O. K. 1970. Effect of dispersion, gravitational segregation, and formation stratification on the recovery of freshwater stored in saline aquifer. *Water Resources Research* 6:1689–1700, doi:10.1029/WR006i006p01689.

LaBrecque, D. J. and Yang, X. 2000. Difference inversion of ERT data: a fast inversion method for 3-D in-situ monitoring. *Proc. Symp. Appl. Geophys. Eng. Environ. Probl., Environ. Eng. Geophys. Soc.* pp. 723–732.

Lesmes, D. and Friedman, S. P. 2005. Relationships between the electrical and hydrogeological properties of rocks and soils, pp. 87–128. *In* Y. Rubin and S. S. Hubbard (eds.), Hydrogeophysics, volume 50 of *Water Science and Technology Library*, chapter 4. Springer.

Linde, N., Binley, A., Tryggvason, A., Pederson, L., and Revil, A. 2006. Improved hydrogeophysical characterization using joint inversion of cross-hole electrical resistance and ground-penetrating radar traveltime data. *Water Resources Research* 42:W12404, doi:10.1029/WR005131.

Loewy, A. 2010. Flow and transport processes below the Shafdan spreading basins. MSc Thesis, University of the Negev, Sde Boker, Israel.

Loke, M. H. and Barker, R. D. 1996. Practical techniques for 3D resistivity surveys and data inversion. *Geophysical Prospecting* 44:499–523.

Looms, M. C., Binley, A., Jensen, K. H., Nielsen, L., and Hansen, T. M. 2008a. Identifying unsaturated hydraulic parameters using an integrated data fusion approach on cross-borehole geophysical data. *Vadose Zone Journal* 7:238–248, doi:10.2136/vzj2007.0087.

Looms, M. C., Jensen, K. H., Binley, A., and Nielsen, L. 2008b. Monitoring unsaturated flow and transport using cross-borehole geophysical methods. *Vadose Zone Journal* 7:227–237, doi:10.2136/vzj2006.0129.

Lu, C., Du, P., Chen, Y., and Luo, J. 2011. Recovery efficiency of aquifer storage and recovery (ASR) with mass transfer limitation. *Water Resources Research* 47:W08529, doi:10.1029/2011WR010605.

Maliva, R. and Missimer, T. 2012. Managed aquifer recharge, pp. 559–630, doi:10.1007/978–3–642–29104–3_23. *In* Arid Lands Water Evaluation and Management, Environmental Science and Engineering. Springer-Verlag, Heidelberg.

Maliva, R. G., Clayton, E. A., and Missimer, T. M. 2009. Application of advanced borehole geophysical logging to managed aquifer recharge investigations. *Hydrogeology Journal* 17:1547–1556, doi:10.1007/s10040–009–0437–z.

Maliva, R. G. and Missimer, T. M. 2010. Hydrogeology of ASR - lessons from over 60 years of global practice. *ISMAR7 Proceedings* pp. 9–13 Oct 2010, Abu Dhabi.

Manoli, G., Rossi, M., Pasetto, D., Deiana, R., Ferraris, S., Cassiani, G., and Putti, M. 2015. An iterative particle filter approach for coupled hydro-geophysical inversion of a controlled infiltration experiment. *Journal of Computational Physics* 283:37–51, doi:10.1016/j.jcp.2014.11.035.

Mawer, C., Kitanidis, P., Pidlisecky, A., and Knight, R. 2013. Electrical resistivity for characterization and infiltration monitoring beneath a managed aquifer recharge pond. *Vadose Zone Journal* 12, doi:10.2136/vzj2011.0203.

Mawer, C., Parsekian, A., Pidlisecky, A., and Knight, R. 2016. Characterizing heterogeneity in infiltration rates during managed aquifer recharge. *Groundwater, doi:10.1111/gwat.12423* .

Mazác, O., Císlerová, M., and Vogel, T. 1988. Application of geophysical methods in describing spatial variability of saturated hydraulic conductivity in the zone of aeration. *Journal of Hydrology* 103:117–126, doi:10.1016/0022–1694(88)90009–1.

Mazzia, A. and Putti, M. 2005. High order Godunov mixed methods on tetrahedral meshes for density driven flow simulations in porous media. *Journal of Computational Physics* 208:154–174, doi:10.1016/j.jcp.2005.01.029.

Mazzia, A. and Putti, M. 2006. Three-dimensional mixed finite element-finite volume approach for the solution of density-dependent flow in porous media. *Journal of Computational and Applied Mathematics* 185:347–359, doi:10.1016/j.cam.2005.03.015.

Meju, M. A., Gallardo, L. A., and Mohamed, A. K. 2003. Evidence for correlation of electrical resistivity and seismic velocity in heterogeneous near-surface materials. *Geophysical Research Letters* 30:1373, doi:10.1029/2002GL016048.

Minsley, B. J., Ajo-Franklin, J., Mukhopadhyay, A., and Dale Morgan, F. 2011. Hydrogeophysical methods for analyzing aquifer storage and recovery systems. *Ground Water,* doi:10.1111/j.1745-6584.2010.00676.x.

Mizrahi, G., Furman, A., and Weisbrod, N. 2016. Infiltration under confined air conditions: Impact of inclined soil surface. *Vadose Zone Journal* 15, doi:10.2136/vzj2016.04.0034.

Müller, K., Vanderborght, J., Englert, A., Kemna, A., Huismann, J. A., Rings, J., and Vereecken, H. 2010. Imaging and characterisation of solute transport during two tracer tests in a shallow aquifer using electrical resistivity tomography and multilevel groundwater samplers. *Water Resources Research* 46:W03502, doi:10.1029/2008WR007595.

Moreno, Z., Arnon-Zur, A., and Furman, A. 2015. Hydro-geophysical monitoring of orchard root zone dynamics in semi-arid regions. *Irrigation Science* 33:303–318, doi:10.1007/s00271–015–0467–3.

Moulder, E. A. 1970. Freshwater bubbles: A possibility for using saline aquifers to store water. *Water Resources Research* 6:1528–1531, doi:10.1029/WR006i005p01528.

Nadav, I., Arye, G., Tarchitzky, J., and Chen, Y. 2012. Enhanced infiltration regime for treated-wastewater purification in soil aquifer treatment (SAT). *Journal of Hydrology* 420-421:275–283, doi:10.1016/j.jhydrol.2011.12.013.

Nenna, V., Pidlisecky, A., and Knight, R. 2014. Monitoring managed aquifer recharge with electrical resistivity probes. *Interpretation* 2:T155–T166, doi:10.1190/INT–2013–0192.1.

Nguyen, F., Kemna, A., Antonsson, A., Engesgaard, P., Kuras, O., Ogilvy, R., Gisbert, J., Jorreto, S., and Pulido-Bosch, A. 2009. Characterization of seawater intrusion using 2D electrical imaging. *Near Surface Geophysics* 7:377–390, doi:10.3997/1873–0604.2009025.

Oberdörster, C., Vanderborght, J., Kemna, A., and Vereecken, H. 2010. Investigating preferential flow processes in a forest soil using time domain reflectometry and electrical resistivity tomography. *Vadose Zone Journal* 9:350–361, doi:10.2136/vzj2009.0073.

Palestinian Water Authority, a. 2012. National water strategy for Palestine - Toward building a Palestinian state from water perspective. Technical report, National Water Policy and Strategy, Full Report, Vol. 2, 114 pp.

Paniconi, C. and Wood, E. F. 1993. A detailed model for simulation of catchment scale subsurface hydrologic processes. *Water Resources Research* 29:1601–1620.

Parsekian, A. D., Regnery, J., Wing, A. D., Knight, R., and Drewes, J. E. 2014. Geophysical and hydrochemical identification of flow paths with implications for water quality at an ARR site. *Groundwater Monitoring and Remediation* 34:105–116, doi:10.1111/gwmr.12071.

Perri, M. T., Cassiani, G., Gervasio, I., Deiana, R., and Binley, A. 2012. A saline tracer test monitored via both surface and cross-borehole electrical

resistivity tomography: Comparison of time-lapse results. *Journal of Applied Geophysics* 79:6–16, doi:10.1016/j.jappgeo.2011.12.011.

Piel, R. 2011. Geophysikalische Charakterisierung eines alluvialen Beckens zur Grundwasser-Anreicherung - Eine Fallstudie im Jordantal, Auja, West Bank. BSc Thesis, Rheinische Friedrich-Wilhelms-Universität Bonn, Germany.

Pruess, K. 2004. The TOUGH codes - a family of simulation tools for multiphase flow and transport processes in permeable media. *Vadose Zone Journal* 3:738–746.

Pruess, K., Oldenburg, C., and Moridis, G. 1999. TOUGH2 User's Guide, Version 2.0. Earth Sciences Division, Lawrence Berkeley National Laboratory.

Pyne, R. D. G. 1995. Groundwater recharge and wells: A guide to aquifer storage and recovery. CRC Press LLC, Boca Raton, Florida.

Rahman, M. A., Rusteberg, B., Gogu, R. C., Lobo Ferreira, J. P., and Sauter, M. 2012. A new spatial multi-criteria decision support tool for site selection for implementation of managed aquifer recharge. *Journal of Environmental Management* 99:61–75.

Ramirez, A. L., Daily, W., and Newmark, R. L. 1995. Electrical resistance tomography for steam injection monitoring and process control. *Journal of Environmental & Engineering Geophysics* 1:39–51.

Reitemeyer, L. 2015. Geoelektrische Messungen an Sanden zur Bestimmung petrophysikalischer Parameter. BSc Thesis, Rheinische Friedrich-Wilhelms-Universität Bonn, Germany.

Revil, A. 2013. Effect conductivity and permittivity of unsaturated porous materials in the frequency range 1 mHz - 1 GHz. *Water Resources Research* 49:306–327, doi:10.1029/2012WR012700.

Revil, A., Karaoulis, M., Johnson, T., and Kemna, A. 2012. Review: Some low-frequency electrical methods for subsurface characterization and monitoring in hydrogeology. *Hydrogeology Journal* 20:617–658, doi:10.1007/s10040–011–0819–x.

Rey, J., Martínez, J., Barberá, G. G., García-Aróstegui, J. L., G.-P. J., and Martínez-Vicente, D. 2013. Geophysical characterization of the complex dynamics of groundwater and seawater exchange in a highly stressed aquifer system linked to a coastal lagoon (SE Spain). *Environmental Earth Sciences* 70:2271–2282, doi:10.1007/s12665–013–2472–2.

Richards, L. H. 1931. Capillary conduction of liquids through porous mediums. *Physics* 1:318–333.

Rossi, M., Manoli, G., Pasetto, D., Deiana, R., Ferraris, S., Strobbia, C., Putti, M., and Cassiani, G. 2015. Coupled inverse modeling of a controlled irrigation experiment using multiple hydro-geophysical data. *Advances in Water Resources,* doi:10.1016/j.advwatres.2015.03.008.

Rubin, Y. and Hubbard, S. S. 2005. Hydrogeophysics, volume 50. Springer, Dorddrecht, The Netherlands.

Schmidt, S., Geyer, T., Guttman, J., Marei, A., Ries, F., and Sauter, M. 2014. Characterisation of conduit restricted karst aquifers - example of the Auja spring, Jordan Valley. *Journal of Hydrology* 511:750–763, doi:10.1016/j.jhydrol.2014.02.019.

Schwartz, B. F. and Schreiber, M. E. 2009. Quantifying potential recharge in mantled sinkholes using ERT. *Ground Water* 47:370–381, doi:10.1111/j.1745–6584.2008.00505.x.

Sen, P. N. and Goode, P. A. 1992. Influence of temperature on electrical conductivity on shaly sands. *Geophysics* 57:89–96.

Simmons, C. T., Fenstemaker, T. R., and Sharp Jr., J. M. 2001. Variable-density groundwater flow and solute transport in heterogeneous porous media: approaches, resolutions and future challanges. *Journal of Contaminant Hydrology* 52:245–275.

Singha, K. and Gorelick, S. M. 2005. Saline tracer visualized with three-dimensional electrical resistivity tomography: Field-scale spatial moment analysis. *Water Resources Research* 41:W05023, doi:10.1029/2004WR003460.

Slater, L. 2007. Near surface electrical characterization of hydraulic conductivity: From petrophysical properties to aquifer geometries - a review. *Survey Geophysics* 28:169–197, doi:10.1007/s10712–007–9022–y.

Slater, L., Binley, A., Daily, W., and Johnson, R. 2000. Cross-hole electrical imaging of a controlled saline tracer injection. *Journal of Applied Geophysics* 44:85–102.

Slater, L. and Lesmes, D. 2002. IP interpretation in environmental investigations. *Geophysics* 67:77–88.

Slater, L. and Reeve, A. 2002. Investigating peatland stratigraphy and hydrogeology using integrated electrical geophysics. *Geophysics* 67:365–378.

Sneh, A. and Rosensaft, M. 2004. Geological map of Israel 1:50,000 - Sheet 7-IV: Rishon Lezion. Technical report, Geological Survey Israel, Jerusalem.

Spitzer, K. 1998. The three-dimensional DC sensitivity for surface and subsurface sources. *Geophysical Journal International* 134:736–746.

Steinel, A. 2012. Guidline for assessment and implementation of managed aquifer recharge (MAR) in (semi-)arid regions - Pre-feasibility study for infiltration of floodwater in the Amman-Zarqa and Azraq basins, Jordan. Report, Bundesanstalt für Geowissenschaften und Rohstoffe (BGR), Federal Ministry for Economic Cooperation and Development, Germany.

Sumner, J. S. 1976. Principles of induced polarization for geophysical exploration, volume 5 of *Developments in Economic Geology*. Elsevier Scientific Publishing Company, Amsterdam, The Netherlands.

Telford, W. M., Geldart, L. P., and Sheriff, R. E. 1990. Applied Geophysics. Cambridge University Press, 2. edition.

Thiel, C., Coltorti, M., Tsukamoto, S., and Frechen, M. 2010. Geochronology for some key sites along the coast of Sardinia (Italy). *Quaternary International* 222:36–47, doi:10.1016/j.quaint.2009.12.020.

Topp, G. C., Davis, J. L., and Annan, A. P. 1980. Electromagentic determination of soil water content: Measurements in coaxial transmission lines. *Water Resources Research* 16:574–582.

Tuinhof, A. and Heederik, J. P. 2003. Management of aquifer recharge and subsurface storage - Making better use of our largest reservoir. NNC-IAH Publication No. 4. Netherlands National Committee for the IAH, Utrecht.

Ulzega, A. and Hearty, P. J. 1986. Geomorphology, stratigraphy and geochronology of Late Quaternary marine deposits in Sardinia. *Zeitschrift für Geomorphologie N. F.* 62:119–129.

UN 2010. The human right to water and sanitation. Technical report, Resolution A/RES/64/292, United Nations General Assembly.

van Genuchten, M. T. 1980. A closed-form equation for predicting the hydraulic conductivity of unsaturated soils. *Soil Science Society of America Journal* 44:892–898.

van Ginkel, M., Olsthoorn, T. N., and Bakker, M. 2014. A new operational paradigm for small-scale ASR in saline aquifers. *Ground Water* 52:685–693, doi:10.1111/gwat.12113.

Vanderborght, J., Kemna, A., Hardelauf, H., and Vereecken, H. 2005. Potential of electrical resistivity tomography to infer aquifer characteristics from tracer studies: A synthetic case study. *Water Resources Research* pp. W06013, doi:10.1029/2004WR003774.

Vereecken, H., Binley, A., Cassiani, G., Revil, A., and Titov, K. 2006. Applied Hydrogeophysics, volume 71 of *IV. Earth and Environmental Sciences*. Springer, Dordrecht, The Netherlands.

Vereecken, H., Kemna, A., Münch, H.-M., Tillmann, A., and Verweerd, A. 2005. Aquifer characterization by geophysical methods, pp. 2265–2283. *In* M. G. Anderson (ed.), Encyclopedia of Hydrological Sciences. John Wiley & Sons Ltd, England.

Wagner, F. M., Möller, M., Schmidt-Hattenberger, C., Kempka, T., and Maurer, H. 2013. Monitoring freshwater salinization in analog transport models by time-lapse electrical resistivity tomography. *Journal of Applied Geophysics* 89:84–95, doi:10.1016/j.jappgeo.2012.11.013.

Ward, J. D., Simmons, C. T., and Dillon, P. J. 2007. A theoretical analysis of mixed convection in aquifer storage and recovery: How important are density effects? *Journal of Hydrology* 343:169–186.

Ward, J. D., Simmons, C. T., and Dillon, P. J. 2008. Variable-density modelling of multiple-cycle aquifer storage and recovery (ASR): Importance of anisotropy and layered heterogeneity in brackish aquifers. *Journal of Hydrology* 356:93–105, doi:10.1016/j.jhydrol.2008.04.012.

Waxman, M. H. and Smits, L. J. M. 1968. Electrical conductivities in oil-bearing shaly sands. *Society of Petroleum Engineers Journal* 8:107–122, doi:10.2118/1863–PA.

Werner, A. D., Bakker, M., Post, V. E. A., Vandenbohede, A., Lu, C., Ataie-Ashtiani, B., Simmons, C. T., and Barry, D. A. 2013. Seawater intrusion processes, investigation and management: recent advances and future challanges. *Advances in Water Resources* 51:3–26, doi:10.1016/j.advwatrres.2012.03.004.

Wolf, L., Werz, H., Hötzl, H., and Ghanem, M. 2007. Exploring the potential of managed aquifer recharge to mitigate water scarcity in the Lower Jordan River Basin within an IWRM approach. *ISMAR6 Proceedings* pp. 30–46.

Xanke, J., Goeppert, N., Sawarieh, A., Liesch, T., Klinger, J., Ali, W., Hötzl, H., Hadidi, K., and Goldscheider, N. 2015. Impact of managed aquifer reacharge on the chemical and isotopic composition of a karst aquifer, Wala reservoir, Jordan. *Hydrogeology Journal* 23:1027–1040, doi:10.1007/s10040–015–1233–6.

Zhou, Q., Shimada, J., and Sato, A. 2001. Three-dimensional spatial and temporal resistivity monitoring of soil water content using electrical resistivity tomography. *Water Resources Research* 37:273–285, doi:10.1029/2000WR900284.

Zuurbier, K. G., Zaadnoordijk, W. J., and Stuyfzand, P. J. 2014. How multiple partially penetrating wells improve the freshwater recovery of coastal aquifer storage and recovery (ASR) systems: A field and modeling study. *Journal of Hydrology* 509:430–441, doi:10.1016/j.jhydrol.2013.11.057.

List of Figures

List of Tables

Symbols & Abbreviations

Symbols

a	absolute error parameter
a	tortuosity factor
$a_{i,j}$	sensitivity of i-th datum with respect to j-th parameter
α	air entry pressure
α_L	longitudinal dispersivity
α_T	transverse dispersivity
b	relative error parameter
c	normalized concentration
c_0	vacuum propagation velocity
Γ	domain within area of interest
$\boldsymbol{d}$	data vector
$\boldsymbol{d}_0$	background data vector
D	hydrodynamic dispersion tensor
$D*$	molecular diffusion coefficient
∂	partial differential
δ	Dirac delta function
$\boldsymbol{\nabla}$	vector Nabla operator - gradient
$\boldsymbol{\nabla\cdot}$	vector Nabla operator - divergence
ϵ	data error
ϵ_i	error estimate of the i-th datum
ε	dielectric permittivity
ε_0	dielectric permittivity in free space
ε_r	relative dielectric permittivity
ϵ	density ratio

ϵ'	viscosity ratio
$\boldsymbol{\eta_z}$	unit vector in z direction
θ	volumetric water content
f	volumetric rate of injected/extracted solute
$\boldsymbol{f(m)}$	forward model operator
F	formation factor
g	gravitational acceleration
h	hydraulic head
H	aquifer thickness
I	electric current strength
k	intrinsic permeability
k_{rel}	relative permeability
K	hydraulic conductivity
K_s	saturated hydraulic conductivity
L	horizontal extent / length
λ	regularization parameter
m	grain size distribution index
m	cementation index
$\boldsymbol{m}$	model vector
$\boldsymbol{m}_0$	background model vector
M_{ij}	spatial moment
μ	fluid viscosity
μ_0	viscosity of freshwater
μ_s	viscosity of saltwater
n	saturation index
N	total number of measurements
$\boldsymbol{\nu}$	Darcy flux or velocity
P	liquid-phase pressure
P_{ref}	reference gas pressure
P_c	capillary pressure
ϕ	porosity
Φ	electric potential field

ψ	pressure head
$\psi(\boldsymbol{m})$	objective function
$q*$	source/sink term
$\boldsymbol{r}_{S+}, \boldsymbol{r}_{S-}$	electrode position vector (current source, sink)
R	electrical resistance
ΔR	electrical resistance error
RR	recovery rate
RMS	root mean square error
ρ	electrical resistivity
ϱ	fluid density
ϱ_0	density of freshwater
ϱ_s	density of saltwater
$\boldsymbol{s}$	cumulative sensitivity
S	water saturation
S_e	effective water saturation
S_r	residual water saturation
S_s	specific storage
σ	electrical conductivity
σ_a	apparent electrical conductivity
σ_b	bulk electrical conductivity of the soil
σ_{max}	maximum electrical conductivity
σ_{min}	minimum electrical conductivity
σ_s	surface electrical conductivity
σ_w	electrical conductivity of pore fluid
$\sum$	sum
t	time
t_0	background time step
t_x	time step
τ	time exponent describing the slope of the curve
Υ	integral of water saturation changes
v	velocity
v_p	seismic p-wave velocity

V_{med}	injection volume (modeled)
V_{obs}	injection volume (observed)
$\boldsymbol{W}_d$	data weighting matrix
$\boldsymbol{W}_m$	first-oder roughness of $\boldsymbol{m}$ matrix
x, y, z	Cartesian coordinates
$\|\cdot\|$	norm

Abbreviations

1D, 2D, 3D	one-dimensional, two-dimensional, three-dimensional
ASR	Aquifer Storage and Recovery
ASTR	Aquifer Storage Transfer and Recovery
b.g.s.	below ground surface
CRMod	Complex Resistivity Modeling
CRTomo	Complex Resistivity Tomography
DC	direct current
ERT	Electrical Resistivity Tomography
GPR	Ground-Penetrating Radar
LJRV	Lower Jordan River Valley
MAR	Managed Aquifer Recharge
MCM	million cubic meters
RS	Refraction Seismics
SAT	Soil Aquifer Treatment
SIP	Spectral Induced Polarization
TDR	time domain reflectometry
TDT	time domain transmittance
UN	United Nations
VWC	volumetric water content
WWTP	wastewater treatment plant

Publikationen Klaus Haaken

Haaken, K., Deidda, G. P., Cassiani, G., Deiana, R., Putti, M., Paniconi, C., Scudeler, C., and Kemna, A. 2017. Flow dynamics in hyper-saline aquifers: hydro-geophysical monitoring and modeling. *Hydrology and Earth System Sciences* 21(3):1439-1454, doi:10.5194/hess-21-1439-2017.

Haaken, K., Furman, A., Weisbrod, N., and Kemna, A. 2016. Time-lapse electrical imaging of water infiltration in the context of soil aquifer treatment. *Vadose Zone Journal* 15(11), doi:10.2136/vzj2016.04.0028.

Haaken, K., Kemna, A., Furman, A., Mizrahi, G., and Weisbrod, N. 2015. Integrated hydrogeophysical monitoring and modelling of soil aquifer treatment for improved recharge management. *Proceedings of German-Israeli Cooperation in Water Technology Research, Status Conference 2015*, Berlin, Germany, March 22-24.

Haaken, K., Oberdörster, C., Sauter, M., and Kemna, A. 2011. Time-lapse electrical imaging as a tool for monitoring and quantification in managed aquifer recharge applications: a numerical feasibility study. *Proceedings of the International Conference on Integrated Water Resources Management (IWRM)*, Dresden, Germany, October 12-13.

Larocque, M., Cook, P. G., Haaken, K., and Simmons, C. T. 2009. Estimating flow using tracers and hydraulics in synthetic heterogeneous aquifers. *Ground Water* 47(6):786-796, doi:10.1111/j.1745-6584.2009.00595.x.

Klose, S. and Haaken, K. 2008. Groundwater quality in Ouled Yaoub. *In* O. Schulz and M. Judex (eds.), IMPETUS Atlas Morocco. Research Results 2000-2007, 3rd edition, *Department of Geography*, University of Bonn, Germany.

Konferenzbeiträge (Vorträge / Poster)

Haaken, K., Furman, A., Weisbrod, N. and Kemna, A. 2015. Time-lapse ERT of water infiltration in the context of soil aquifer treatment. *GELMON 3rd International Workshop on Geoelectrical Monitoring*, Vienna, Austria, November 24-26. *(Vortrag)*

Haaken, K., Furman, A., Weisbrod, N. und Kemna, A. 2015. Dynamische elektrische Widerstandstomographie von Wasserinfiltration im Bereich des Soil Aquifer Treatment in Israel. *75. Jahrestagung der Deutschen Geophysikalischen Gesellschaft (DGG)*, Hannover, 23.-26. März. *(Vortrag)*

Haaken, K., Furman, A., Weisbrod, N. and Kemna, A. 2014. Hydrogeophysical monitoring of water infiltration in the context of soil aquifer treatment at the Shafdan site (Israel). *AGU Fall Meeting*, San Francisco, USA, December 15-19. *(Vortrag)*

Haaken, K., Furman, A., Weisbrod, N. und Kemna, A. 2014. Dynamische Widerstandstomographie von Soil Aquifer Treatment für verbessertes Management der künstlichen Grundwwasseranreicherung in Israel. *74. Jahrestagung der Deutschen Geophysikalischen Gesellschaft (DGG)*, Karlsruhe, 10.-13. März. *(Poster)*

Haaken, K., Deidda, G. P., Cassiani, G., Kemna, A., Deiana, R., Putti, M., Scudeler, C., and Paniconi, C. 2013. Cross-hole ERT monitoring to investigate mixing processes of freshwater injection in a hyper-saline aquifer. *GELMON 2nd International Workshop on Geoelectrical Monitoring*, Vienna, Austria, December 4-6. *(Vortrag)*

Haaken, K., Deidda, G. P., Cassiani, G., Kemna, A., Deiana, R., Putti, M., and Paniconi, C. 2013. Hydrogeophysical monitoring and modeling of freshwater injection in a hyper-saline aquifer. *International Conference NovCare (Novel Methods for Subsurface Characterization and Monitoring: From Theory to Practice)*, Leipzig, Germany, May 13-16. *(Poster)*

Haaken, K., Deidda, G. P., Cassiani, G., Kemna, A., Deiana, R., Putti, M., Paniconi, C., Schirru, F., and Mura, M. 2013. Cross-hole ERT monitoring of freshwater injection in a hyper-saline aquifer. *Advancing Hydrogeophysics - A Young Scientists Workshop on Combining Hydrologists Needs and Geophysical Input*, Hornberg, Germany, February 22-24. *(Poster)*

Haaken, K., Deidda, G. P., Cassiani, G., Kemna, A., Deiana, R., Putti, M., Paniconi, C., Schirru, F., and Mura, M. 2012. Cross-hole ERT monitoring of freshwater injection in a hyper-saline aquifer. *Geophysical Research Abstracts, EGU General Assembly* Vienna, Austria, Vol. 14, EGU2012-11789. *(Poster)*

Haaken, K., Oberdörster, C., and Kemna, A. 2011. Monitoring water infiltration for managed aquifer recharge using time-lapse electrical imaging: a numerical feasibility study. *71. Jahrestagung der Deutschen Geophysikalischen Gesellschaft (DGG)*, Köln, Germany, February 21-24. *(Poster)*

Flores-Orozco, A., Kemna, A., Haaken, K., Cassiani, G., and Binley, A. 2011. Improved site characterisation through time-lapse complex resistivity imaging. *71. Jahrestagung der Deutschen Geophysikalischen Gesellschaft (DGG)*, Köln, Germany, February 21-24. *(Poster)*

Haaken, K., Kemna, A., and Sauter, M. 2010. Monitoring water infiltration for managed aquifer recharge using time-lapse electrical imaging: a numerical feasibility study. *Geophysical Research Abstracts, EGU General Assembly* Vienna, Austria, Vol. 12, EGU2010-8657. *(Poster)*